Countrywide and Transboundary Spatial Reconstruction of Rainfall Using Commercial Microwave Links

Dissertation
zur Erlangung des Doktorgrades
an der Fakultät für Angewandte Informatik
der Universität Augsburg

vorgelegt von

Nico Blettner

Oktober 2023

Erstes Gutachten:	Prof. Dr. Harald Kunstmann
Zweites Gutachten:	Prof. Dr. Elke Hertig
Tag der mündlichen Prüfung:	05.07.2024

Abstract

Rainfall strongly influences the availability of water on the land surface, and hence, its quantification is utterly relevant for addressing a variety of social, economic, and environmental matters. Quantification via traditional rainfall measuring devices has its limitations and can be supported by opportunistic sensors like commercial microwave links (CMLs), which theoretically enable rainfall estimation on large spatial scales due to their vast global abundance. However, estimation across organizational (e.g., national) boundaries is challenging due to heterogeneous CML data sets with customized rainfall retrieval methods. Moreover, common interpolation techniques have shortcomings in using path-averaged CML observations for spatial rainfall reconstruction. These challenges of CML-based transboundary rainfall estimation have been addressed in this thesis by generating rainfall maps of hourly temporal resolution, which were evaluated using a weather radar reference. Two large CML data sets from Germany and the Czech Republic with distinctly different network characteristics were combined and processed jointly via established and extended algorithms to generate transboundary rainfall maps. Beyond that, the German CML data set was combined with a countrywide network of rain gauges to generate rainfall maps via a stochastic reconstruction approach called Random Mixing (RM). The quality of these maps was analyzed considering an alternative standard Kriging approach and an object-based validation scheme named eSAL, which quantifies errors in structure, amplitude, and location. The computational complexity of RM was examined and reduced. It was found that the German and Czech CML data sets could be processed jointly to generate consistent transboundary rainfall maps once issues of limited data quality were identified and addressed by appropriate universal algorithms. The strong influence of partly hardware-dependent data quality issues could be demonstrated. Furthermore, stochastic reconstruction via RM proved to enable the generation of rainfall maps with accurate pattern representation. Despite a general underestimation and relatively high computational complexity, the method had clear advantages over the Kriging approach as indicated in particular by significantly lower structure errors and by providing probabilistic ensemble solutions. The results yield evidence for the capabilities of generating high-quality CML-based rainfall maps on large spatial scales, even across political borders, and hence, they contribute to better utilize the potential of CMLs as widespread rainfall sensors worldwide.

Kurzfassung

Niederschlagsmengen haben einen großen Einfluss auf die Verfügbarkeit von Wasser auf der Landoberfläche, weshalb ihre Quantifizierung für eine Vielzahl von sozialen, ökonomischen und ökologischen Fragen äußerst wichtig ist. Die Quantifizierung mittels herkömmlicher Niederschlagsmessgeräte hat ihre Grenzen und kann durch opportunistische Sensoren wie kommerzielle Richtfunkverbindungen (CMLs) unterstützt werden, die aufgrund ihrer enormen globalen Verbreitung theoretisch eine Niederschlagsschätzung auf großen räumlichen Skalen ermöglichen. Die Schätzung über organisatorische (z. B. nationale) Grenzen hinweg ist jedoch aufgrund heterogener CML-Datensätze mit individuell angepassten Methoden zur Ableitung der Regenmengen eine Herausforderung. Außerdem haben gängige Interpolationsmethoden Defizite bei der Verwendung pfadgemittelter CML-Beobachtungen für die räumliche Niederschlagsrekonstruktion. Diese Herausforderungen der CML-basierten grenzüberschreitenden Niederschlagsschätzung wurden in dieser Arbeit thematisiert, indem Niederschlagskarten mit stündlicher Auflösung erstellt und anhand einer Wetterradar-Referenz evaluiert wurden. Zwei große CML-Datensätze aus Deutschland und der Tschechischen Republik mit deutlich unterschiedlichen Netzwerkeigenschaften wurden kombiniert und gemeinsam mittels bewährter sowie erweiterter Methoden verarbeitet, sodass grenzüberschreitende Niederschlagskarten erstellt werden konnten. Der deutsche CML-Datensatz wurde zudem mit einem landesweiten Netz von Regenmessern kombiniert, um Niederschlagskarten mittels eines stochastischen Rekonstruktionsansatzes namens *Random Mixing* (RM) zu erstellen. Die Qualität dieser Karten wurde unter Berücksichtigung eines alternativen Standard-Kriging-Ansatzes und einer objektbasierten Validierung namens eSAL analysiert, die Fehler in Struktur, Amplitude und Lage quantifiziert. Der Rechenaufwand von RM wurde untersucht und reduziert. Es wurde festgestellt, dass die deutschen und tschechischen CML-Datensätze gemeinsam verarbeitet werden können, um konsistente grenzüberschreitende Niederschlagskarten zu erstellen, sobald Probleme begrenzter Datenqualität erkannt und durch geeignete universelle Algorithmen behoben wurden. Der starke Einfluss von teilweise hardwareabhängigen Datenqualitätsproblemen konnte nachgewiesen werden. Darüber hinaus hat sich gezeigt, dass die stochastische Rekonstruktion mittels RM die Erstellung von Niederschlagskarten mit genauer räumlicher Verteilung ermöglicht. Trotz einer generellen Unterschätzung und eines relativ hohen Rechenaufwands hatte die Methode deutliche Vorteile gegenüber dem Kriging-Ansatz,

die sich insbesondere in wesentlich geringeren Strukturfehlern und in der Bereitstellung probabilistischer Ensemble-Lösungen zeigten. Die Ergebnisse belegen, dass es möglich ist, qualitativ hochwertige CML-basierte Niederschlagskarten auf großen räumlichen Skalen, auch über politische Grenzen hinweg, zu erstellen und tragen somit dazu bei, das Potenzial von CMLs als weit verbreitete Niederschlagssensoren weltweit besser nutzbar zu machen.

Acknowledgments

I would like to express my gratitude to

- Prof. Dr. Harald Kunstmann for providing me the opportunity to conduct research in the exciting field of hydrometeorology, for many important guiding ideas, and the respectful and encouraging way of interaction;
- Prof. Dr. Elke Hertig for agreeing on examining this thesis;
- Dr. Christian Chwala for constant willingness for detailed discussions, for teaching me many aspects of rainfall monitoring and code development, and for his trust in my work;
- Dr. Sebastian Hörning and Dr. Barbara Haese for many productive discussions and for sharing their knowledge of Random Mixing;
- my fellow group members, friends, and colleagues working on similar topics for the helpful exchange and general mutual support in all matters;
- the project partners from the Czech Technical University for the pleasant collaboration and for hosting my research stay in Prague;
- numerous colleagues at KIT/IMK-IFU for creating a great scientific and social environment;
- many people I met during conferences and workshops for scientific and cultural exchange and joint projects;
- KIT/IMK-IFU for providing work facilities and access to high-performance computers
- the IFU Graduate Program for offering many interesting workshops and coaching opportunities; and finally,
- my family and my partner for always being there for me.

Contents

List of Figures

List of Tables

List of Abbreviations and Symbols

A_q	Signal quantization [dB]
A_R	Rainfall-induced attenuation [dB]
ATPC	Automatic transmit power control
BL	Baseline attenuation [dB]
CML	Commercial microwave link
CZ	Czech Republic
DE	Germany
DL	Detection limit [mm/h]
DSD	Drop size distribution
DWD	German Weather Service (ger.: Deutscher Wetterdienst)
$(e)A$	Amplitude component of (e)SAL metrics [-]
$(e)L$	Location component of (e)SAL metrics [-]
$(e)L_1$	Domain-wide aspect of location component of (e)SAL metrics [-]
$(e)L_2$	Object-related aspect of location component of (e)SAL metrics [-]
$(e)S$	Structure component of (e)SAL metrics [-]
(e)SAL	(Ensemble) structure, amplitude, location error
eRM	The full ensemble reconstructed by Random Mixing
est	Suffix for variables describing the estimate
FF	Final field (in Random Mixing algorithm)
$freq$	Frequency [GHz]
G	CML length (distance between antennas) [km]
HF	Homogeneous field (in Random Mixing algorithm)
IF	Inner field (in Random Mixing algorithm)
ITU	International Telecommunication Union
k	Specific attenuation [dB/km]
KRI	The reconstruction by Ordinary Kriging

M	Number of ensemble members
MAE	Mean absolute error [mm]
MHRW	Metropolis-Hastings random walk
mRM(M)	Ensemble mean over M members of the Random Mixing reconstruction
NF	Normal field (in Random Mixing algorithm)
nug	Nugget effect (semivariogram)
OK	Ordinary Kriging
PCC	Pearson correlation coefficient [-]
pol	Polarization
QC	Quality control
QPE	Quantitative precipitation estimation
R	Rainfall rate [mm/h]
R_H	Hourly rainfall sum [mm]
rec	Suffix for variables describing the reconstruction
ref	Suffix for variables describing the reference
RG	Rain gauge
RM	Random Mixing
$RMSE$	Root-mean-square error [mm]
rng	Range (semivariogram)
RSL	Received signal level [dB]
SF	Solution field (in Random Mixing algorithm)
sRM	A single ensemble member of the Random Mixing reconstruction
TL	Total loss (of signal intensity) [dB]
TSL	Transmitted signal level [dB]
UF	Unconditional field (in Random Mixing algorithm)
WAA	Wet antenna attenuation [dB]
Z	Radar reflectivity [mm^6/m^3]
$\gamma()$	Semivariogram function
Γ	Covariance matrix
$\vartheta()$	Transformation function (in Random Mixing algorithm)
$\Phi()$	Standard normal cumulative distribution function
$\chi()$	Marginal distribution function

Chapter 1

Introduction

1.1 Significance, Aim, and Challenge of Rainfall Estimation

The amount and distribution of water is essential to all forms of life. All species on the land surface directly depend on water. Humans, moreover, not only require drinking water but also need it for indirect purposes such as establishing and maintaining agriculture, hydraulic energy supply, transportation, industrial cooling, etc. Throughout history, human cultures have been tightly interconnected with the presence of water and its significance is indisputable.

The amount of water on land is on the one hand limited and on the other hand unequally distributed. Consequently, water shortage is a serious widespread threat (Vörösmarty et al., 2010; Mekonnen and Hoekstra, 2016; Liu et al., 2017)). Water scarcity can be expected to become more severe due to population increase but also due to changing availability related to climate change (IPCC, 2022). Severe droughts such as the one in the Horn of Africa (UNHCR, 2023) that lasts for several years by now, or the ones in large parts of Europe in recent summers (Rousi et al., 2023) are occurring with increasing frequency and intensity. Conversely, *too much* water can be a threat, too. Cases of floods, landslides or soil erosion show the harmful potential of a surplus of water. The flooding in Belgium, France, Luxembourg, and western Germany in July 2021 (Tradowsky et al., 2023), in Iran and Pakistan in summer 2022 (World Economic Forum, 2023), or in Greece and Libya in September 2023 are recent examples of the catastrophic consequences of enormous river discharges.

Precipitation is the prime direct source for water on land. Hence, the amount and distribution of precipitation directly causes both extreme shortcomings and surpluses of water. *Too little* water is usually associated with a shortage of rainfall over several days, months, or even years (Mishra and Singh, 2010). For extreme precipitation, on the other hand, the crucial time spans can be distinctly different. While flooding can be related to longer periods of strong precipitation in a region, they can in many cases be linked to relatively short events of extreme precipitation. Flash floods, in particular, are often the direct result of such exceptional events that may last not more than a few hours (Hapuarachchi et al., 2011).

In order to learn about water availability, quantitative precipitation estimation (QPE) is of greatest relevance. QPE is required to answer crucial questions like: how much did it rain over a particular river catchment? What was the peak rain rate of a given event? Where and when exactly did it occur? The basis for answering these and similar questions, is to quantify precipitation accurately in space and time. The better the knowledge about precipitation the better the forecast of river discharges and water availability on the land surface. Such forecasts enable more suitable response measures – whether, for example, in mitigating the damage induced by floods or optimizing the irrigation arrangements on a crop field. While QPE considers both solid and liquid precipitation, focus can be given to rainfall as its predominant type.

Whereas accurate rainfall estimation is highly valuable, it is also very challenging. Regarding flash floods, for example, forecasting errors in the rainfall field are considered the largest source of uncertainty (Hapuarachchi et al., 2011). The difficulties in quantifying rainfall can be explained to a large extent by its specific and fairly unique properties. For example, rainfall is very different from other meteorological parameters such as temperature or pressure in that it displays intermittency. That is, there is a binary element to rainfall as it can be zero or nonzero and therefore, it cannot be modeled as a continuous function in space or time. And noteworthy, zero rainfall is much more common than nonzero rainfall, particularly when considering rather short time spans (Schleiss et al., 2011). Moreover, rainfall can be highly variable: At a given point in time, for instance, there might be extreme rainfall at one location, whereas it remains dry relatively close by. Similarly, it may be dry only a few minutes after extreme rainfall at a given location. Furthermore, aggregating over time influences the spatial variability, and vice versa: In a given region, for example, the spatial variability may be moderate when considering rainfall amounts over long periods (such as years or months) but increases when considering amounts over short periods (such as hours or minutes) (Krajewski et al., 2003).

In spite of these challenges, rainfall quantification should ideally be accurate and cover large spatial and temporal extents consistently with a high resolution. Neither the instantaneous rainfall amount of one isolated minute, nor the temporal continuous information for only a tiny subset of a river catchment is of much help to forecast river discharges, or any other hydrologically relevant information. As will become clear in the following, especially the wide and dense spatial coverage of rainfall information is a major challenge involving political and scientific obstacles.

1.2 State of the Art

1.2.1 Rainfall Observations

In order to gain knowledge of rainfall, the fundamental approach is to measure it. Notably, also (numerical) weather models can provide information on rainfall and these have improved significantly with respect to quality and resolution in recent decades Bauer et al. (2015). However, even the development and the validation of such models depends on actual observations as the primary source of information.

Several diverse types of measurement instruments exist to observe rainfall amounts: rain gauges, weather radar and satellites provide information on rainfall in quite different ways and each of those has its specific advantages and shortcomings. Next to such dedicated instruments, also information from other sources are used opportunistically.

Rain gauges have been used since ancient times (Strangeways, 2010) and still play an important role in modern rainfall observation. A rain gauge directly measures the amount of rainfall in time at a specific location. While their observations can be considered accurate (Lanza and Vuerich, 2009), rain gauge measurements are restricted to the tiny local area in the order of 0.02 m^2 per sensor. For the spatially highly variable rainfall, this lack of spatial representativeness is a limiting factor (Ciach and Krajewski, 2006).

Newer, but well-established rainfall observations come from weather radars. They provide area-wide information via remote sensing and, hence, overcome the rain gauges' lack of spatial coverage. However, weather radars also have shortcomings stemming from the indirect measurement, beam blockage, ground clutter and the fact that rainfall is observed at significant height above ground (Hazenberg et al., 2011; Berne and Krajewski, 2013). Moreover, weather radars are simply not available in many regions as their installation and maintenance involve high costs.

Additionally, remote sensing of rainfall can be achieved by satellites of various types. Accurate and spatially high-resolved information, e.g., is provided by the Global Precipitation Measurement Mission (Hou et al., 2014; Skofronick-Jackson et al., 2017), which involves a core satellite with two radar sensors. However, being a non-stationary low Earth orbit satellite, it provides only snapshots in time. These can be combined with radiometer measurements of other satellites to provide continuous coverage (e.g., via the Integrated Multi-satellite Retrievals for GPM (IMERG) product (Huffman et al., 2020)), for which, however, the accuracy and quality of the temporal continuity is not comparable to a pure radar observation. Geostationary satellites (e.g., MSG SEVIRI (Aminou, 2002)) can also be used for rainfall estimation via visible or infrared channels. Their major disadvantage is considerable uncertainty stemming from the indirect measurement of clouds' top.

Since the aforementioned dedicated sensors are not free of limitations, opportunistic sensing devices have been considered as an additional source of information. These are devices which are not primarily installed to measure rainfall, at least not on a professional level, but which produce data that allows a rainfall estimation nonetheless. As they are installed and primarily used for other purposes, they usually require no additional installation or maintenance costs. Opportunistic sensing can be used as a support for dedicated sensors, but more importantly, it may be the only source of information in regions where no dedicated sensors exist.

Commercial microwave links (CMLs) are arguably the best studied and most widely used opportunistic sensing devices for rainfall monitoring. They have been used for almost two decades. A CML constitutes a line of sight connection between two sites established by the transmission of microwave radiation between directional antennas. CMLs have the primary purpose of facilitating cell phone communication or other types of communication infrastructure via the exchange of microwave radiation. The radiation is attenuated by rain which allows an estimation of path-averaged rain rates based on observed signal intensities (Messer, 2006; Leijnse et al., 2007). CMLs are very abundant, notably also in regions where dedicated sensors are not (Overeem et al., 2016b). Moreover, they measure close to the ground and can be used even in mountainous terrain which is problematic for weather radars (Smiatek et al., 2017; Nebuloni et al., 2022). Unfortunately, being opportunistic sensors, CMLs lack strict conventions and require elaborate processing routines, which are not unified but usually adapted to individual data sets. Moreover, they provide only average rainfall information along their paths, and they are limited with respect to estimating solid precipitation (Overeem et al., 2016b; Graf et al., 2020).

In summary, no type of observation alone provides the desired quality of rainfall information. Often, a combination of data sources increases the quality (McKee and Binns, 2016; Ochoa-Rodriguez et al., 2019) and such combined products are used on an operational basis, e.g., by meteorological services. Typically, rain gauges are used to adjust spatial satellite or radar products. However, dedicated sensors are still limited and most importantly not available everywhere. Hence, rainfall estimation can benefit from the consideration of opportunistic CML data. For this purpose and despite the progress in recent decades, further research is required to address the specific challenges involved in their usage. Most prominently addressed in this thesis, is the question: how to best derive spatial rainfall estimates over large extents from CML observations.

1.2.2 Spatial Rainfall Estimates

Whenever CMLs or rain gauges should be considered independently and not only to support spatial (radar- or satellite-based) products, a crucial question needs to be addressed: how to derive spatial estimates from scattered local observations? While the observations may provide extensive and highly-resolved information with respect to time, the spatial coverage is naturally always limited as the rainfall sensors cannot be located everywhere.

Consequently, using CML or rain gauge data requires some way of spatial interpolation to estimate rainfall in space, that is, to estimate rainfall maps. This is particularly challenging due to the high spatial variability of rainfall in combination with the relatively low sensor density. For CMLs, moreover, it is not obvious how to account for their path-averaged nature: Their measurement involves uncertainty of the exact location of rainfall along the CML paths. Furthermore, the path-averaged information cannot fully represent extreme values as they are naturally smoothed by the process of averaging. Spatial estimation techniques should ideally be able to account for these effects.

CML-based rainfall maps have been estimated in a variety of studies (e.g., Zinevich et al. (2008); Goldshtein et al. (2009); Overeem et al. (2013, 2016b); D'Amico et al. (2016); Graf et al. (2020); Roversi et al. (2020)). Partly, these maps have been generated by standard ways of spatial interpolation like Inverse Distance Weighting (Graf et al., 2020) or Ordinary Kriging (Overeem et al., 2013, 2016b; Roversi et al., 2020). In these attempts the path-based nature of the observation is disregarded and the CML is considered a virtual gauge at the center of the path. While these attempts provide meaningful results, they are certainly not optimal as information is lost. There have also been studies focusing on the interpolation part and on how to best use the path-averaged CML information. Goldshtein et al. (2009) considered not only the midpoint but several points along the CML paths. However, still not the full integral character is represented by this method, and its calculation is sensitive to rain cell characteristics. Zinevich et al. (2008) and D'Amico et al. (2016) applied different approaches of tomographic models to estimate spatial rainfall. While the latter study considered only an area of a few hundreds of square kilometers and three CMLs, the former considered a relatively large area of 3200 m^2 but obtained accurate high spatial resolution rainfall fields only for an urban subregion where the CML density was particularly high. A different approach of Bayesian assimilation (Scheidegger and Rieckermann, 2014) showed potential in a small setting but with the shortcoming that a Gaussian distribution is required, which does not apply for a typical rainfall distribution. Another method was applied by Haese et al. (2017): They showed the potential of stochastic reconstruction via the so-called Random Mixing (RM) method (Bárdossy and Hörning, 2016b) for the usage in rainfall estimation. The method enables the generation of rainfall fields that can represent rainfall statistics and account for the effect of path-averaging of CMLs. These promising results, however, have so far only been obtained on the scale of rather small river catchments with a limited amount of data. So far, no study has focused on the aspect of interpolation and at the same time considered particularly large spatial extents and amounts of data.

1.2.3 Spatial Extension of Rainfall Estimates

When considering large spatial extents a crucial barrier is imposed by political and organizational boundaries. Both the networks of dedicated sensors and those of CMLs are commonly organized on regional or national levels. Generating consistent rainfall estimates across boundaries is not straightforward as data acquisition, data quality control, and processing routines can vary significantly between independent networks. Nevertheless, the generation of transnational rainfall estimates has been addressed: for example, European composites are generated via merging of individual radar data sets by the European Meteorological Network (EUMETNET) in the OPERA program. Despite major advancements, there remain various challenges involved in the process of merging and substantial limitations in the quality of the composites (Huuskonen et al., 2014; Haase and Johnson, 2018).

While it is difficult even for dedicated sensors to generate transboundary rainfall products, it is arguably even more challenging for CMLs. Firstly, data access and hence data exchange across borders is generally very limited as individual agreements with network providers need to be established (Chwala and Kunstmann, 2019). Moreover, CML networks are not designed to measure rainfall and hence no conventions and homogeneity of data quality exist as, for example, for rain gauge or radar networks. Independent CML data sets have their specific hardware characteristics, e.g., different distributions of antenna distances, different radiation frequencies, and different types and rates of recording. That is, for several historical reasons there exists a significant heterogeneity among independent national CML networks. The differences affect the usability of data as well as rainfall retrieval and mapping processes. Hence also the complex processing routines that are necessary to derive rainfall from raw observable data, are closely adapted and specific to individual data sets.

Actually, these challenges have so far prevented transboundary CML-based rainfall estimation altogether. While many studies have generated rainfall maps on different scales, the countrywide scale, e.g., of the Netherlands (Overeem et al., 2016b) or Germany (Graf et al., 2020), could not yet be transgressed. All examples of CML-based rainfall estimation are based on individual regional or at most national data sets obtained from single network providers. Therefore, it is utterly unclear whether two independent CML data sets from different countries and different network providers can be combined and processed jointly to estimate rainfall across national borders. This research gap disguises whether the enormous potential given by the global availability of CMLs could actually be utilized.

1.2.4 Spatial Validation

After generating rainfall maps, a common step is their validation via performance metrics considering a reference. Many of the above mentioned studies that focus on CML-based rainfall maps have based their conclusions of the quality of reconstructions on specific performance metrics. The usual metrics comprise bias, correlation coefficient, coefficient of variation, etc. which are central, e.g., in Zinevich et al. (2008); Overeem et al. (2013); Graf et al. (2020). However, it is also known that these metrics have shortcomings and often cannot give a final answer to the question whether a reconstruction is actually a good representation of the reference that is regarded as the truth (Ebert, 2008; Gilleland et al., 2009). Some crucial aspects of the reconstruction such as a representation of reasonable rainfall patterns can hardly be assessed by such metrics.

Several other classes of performance metrics exist which enable a broader quality evaluation (Gilleland et al., 2009), however, few of these have been consulted in CML-based rainfall maps in earlier studies. For example, the so-called SAL metrics (Wernli et al., 2008) provide a useful way of validating rainfall patterns by focusing on the correct representation of rainfall objects within the maps. The extension (e)SAL (Radanovics et al., 2018) is even suitable to validate stochastic ensemble-based rainfall maps. These metrics have so far been considered mainly for the validation of model-derived rainfall fields (Portele et al., 2021; Laux et al., 2021), but not for CML-derived maps.

1.3 Research Questions and Objectives

Based on the state of the art and the research gaps presented in the previous chapter, the overarching research questions of this thesis are formulated as follows:

- Can two large independent CML data sets be combined and processed jointly to generate consistent transboundary rainfall maps?
- What are the benefits of rainfall maps generated by stochastic reconstruction via Random Mixing (RM) using large CML and rain gauge data sets?

These questions are addressed in this thesis via two main case studies. The first objective is to combine two independent and heterogeneous CML data sets from Germany and the Czech Republic and to produce transboundary rainfall maps. In this case study a central aspect considered is the processing of CML raw data: The aim is to homogenize the individual CML data sets to allow for joint and consistent rain rate retrieval and mapping procedures. This involves a detailed investigation of aspects of data quality. Adapted and new algorithms are tested in a range of combinations, and their effect is analyzed via an evaluation of the estimated path-averaged rainfall per CML and the rainfall maps.

The second main objective of this thesis is the generation of rainfall maps using a combination of CMLs and rain gauges in Germany in a stochastic reconstruction approach. The method RM is used for the first time with a combination of large (countrywide) rain gauge and CML data sets. These maps are thoroughly evaluated by different sets of performance indices with the particular aim of quantifying the quality of the representation of rainfall patterns via the so-called eSAL performance metrics. Moreover, the advantage of the stochastic approach and its ability for ensemble calculation are evaluated. The evaluation includes a direct comparison of RM with a deterministic reconstruction via Ordinary Kriging (OK).

Additionally, this thesis addresses technical aspects of the applied methods as these are inseparably connected to answering the scientific questions: first, the reconstruction method RM had to be adjusted to enable its usage with the large data sets considered in this thesis. In this context, the method and its subroutines were analyzed with respect to their computational cost and runtime requirements. Moreover, the calculation of the eSAL performance metrics that were applied to quantify aspects of rainfall patterns was implemented in the Python programming language.

1.4 Innovation

This thesis provides several insights in CML-based rainfall estimation and addresses various aspects of processing raw data, spatial reconstruction and validation. It combines data and methods for reconstruction and validation in several new ways. Moreover, it presents solutions to technical obstacles in the methods of rainfall quantification. The main innovations are:

- the generation of the first transboundary CML-based rainfall maps;
- the development of the methodology to allow for combining independent data sets of CMLs;
- the generation of the first countrywide CML-based rainfall reconstruction via RM;
- the contribution to overcome obstacles for the application of RM with large CML and rain gauge data sets; and
- the implementation of the calculation of the (e)SAL performance metrics in Python.

1.5 Structure of this Thesis

The remainder of this thesis is broadly structured into three parts: Chapters 2–5 describe theory, data, and methods, Chapters 6 and 7 present the results, and Chapter 8 provides final conclusions. An overview of the main aspects of CML-based QPE, its validation, and how the chapters of this thesis relate to those aspects is presented in Figure 1.1.

In **Chapter 2** essential theory of the considered sensor types, as well as the actually used data sets are described. Subsequently, **Chapter 3** presents general challenges and the applied algorithms of CML data processing for rainfall estimation. **Chapter 4** introduces aims and concepts of spatial reconstruction methods and describes the stochastic reconstruction

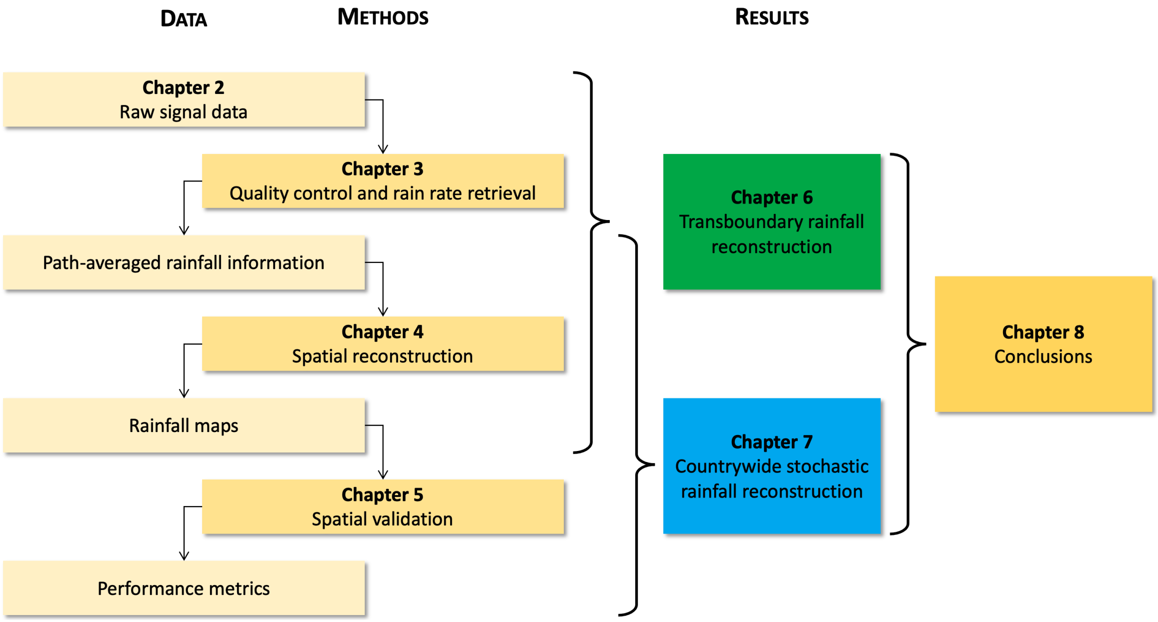

Figure 1.1: Thesis structure by reference to a typical CML-based QPE procedure (left). The procedure starts when rainfall affects the raw signal data of CMLs, which is processed via quality control and rain rate retrieval algorithms to obtain path-averaged rainfall information; based on this scattered information, a rainfall map is generated via a reconstruction method and the validation of the map provides performance metrics. The results are presented in two case studies each addressing one of the posed research questions and each focusing on different parts of the QPE procedure.

method RM. **Chapter 5** is about the validation of rainfall estimates and describes several performance metrics with the focus on the (e)SAL metrics. **Chapter 6** is about results of the case study on the combination of independent CML data sets that are used to generate transboundary rainfall maps. **Chapter 7** presents the results of the case study on countrywide rainfall maps using CML and rain gauge data, the RM reconstruction method, and the eSAL validation approach. Finally, **Chapter 8** provides answers to the research questions, a discussion of the results, and an outlook on potential future research in this field.

1.6 Publications

Note that the results presented in Chapter 6 and Chapter 7 are based on the two publications

- Blettner, N., Fencl, M., Bareš, V, Kunstmann, H., and Chwala, C. Transboundary rainfall estimation using commercial microwave links. *Earth and Space Science*, 10(8), 2023. doi: 10.1029/2023EA002869

  Abstract: Unlike actual rainfall, the spatial extent of rainfall maps is often determined by administrative and political boundaries. Similarly, data from commercial microwave links (CMLs) is usually acquired on a national basis and exchange among countries is limited. Up to now, this has prohibited the generation of transboundary CML-based rainfall maps despite the great extension of networks across the world. We present CML based transboundary rainfall maps for the first time, using independent CML data sets from Germany and the Czech Republic. We show that straightforward algorithms used for quality control strongly reduce anomalies in the results. We find that, after quality control, CML-based rainfall maps can be generated via joint and consistent processing, and that these maps allow to seamlessly visualize rainfall events traversing the German-Czech border. This demonstrates that quality control represents a crucial step for large-scale (e.g., continental) CML-based rainfall estimation.

- Blettner, N., Chwala, C., Haese, B., Hörning, S., and Kunstmann, H. (2022). Combining commercial microwave link and rain gauge observations to estimate countrywide precipitation: A stochastic reconstruction and pattern analysis approach. *Water Resources Research*, 58(10), 2022. doi: 10.1029/2022WR032563

  Abstract: Accurate spatiotemporal precipitation quantification is a crucial prerequisite for hydrological analyses. The optimal reconstruction of the spatial distribution, that is, the rainfall patterns, is particularly challenging. In this study, we reconstructed spatial rainfall on a countrywide scale for Germany by combining commercial microwave link and rain gauge observations for a better representation of the variability and spatial structure of rainfall. We further developed and applied the Random-Mixing-Whittaker-Shannon method, enabling the stochastic reconstruction of ensembles of spatial fields via linear combinations of unconditional random fields. The pattern of rainfall objects is evaluated by three performance characteristics, that is, ensemble Structure-, Amplitude-, and Location-error. Precipitation estimates obtained are in good agreement with the gauge-adjusted weather radar product RADOLAN-RW of the German Weather Service (DWD) which was used as a reference. Compared to reconstructions by Ordinary Kriging, Random Mixing showed clear advantages in the pattern representation via a five times smaller median structure error.

Chapter 2

Data: Rainfall Observations

This chapter gives an overview of observational data that is used in this thesis. It includes theoretical background as well as an introduction to the specific used data sets. Dedicated devices, that is, rain gauges and weather radar are covered in Section 2.1. The opportunistic sensing via commercial microwave links (CMLs) is the topic of Section 2.2.

2.1 Dedicated Rainfall Sensors: Rain Gauges and Weather Radar

2.1.1 Sensing Principle

As mentioned above, rain gauges have a long history and provide accurate but very local observations. They constitute the standard ground-based rainfall information and are installed and maintained by many meteorological services and other institutions on various scales. Rain gauges directly measure the amount of precipitation in a usually cylindrical container (see Figure 2.1). The exact way of measuring can vary and has evolved over time. In the simpler and earlier versions, rainfall amount was read from a scale at the side of the device. Modern gauges usually measure by the number of tilts of a scale (*tipping-bucket*) or by weighing the amount of water that entered the container. The devices are often heated to allow for measuring even solid precipitation. Contemporary instruments provide accurate measurements even though wind induced bias has a considerable effect (Pollock et al., 2018; Por and Sevruk, 1999). Depending on the network size and density, only moderate costs for installation and maintenance are required. Nonetheless, on a global scale, the number of rain gauges and particularly the orifice area is very limited (Lorenz and Kunstmann, 2012; Kidd et al., 2017).

Weather radars enable rainfall measurement via remote sensing and thereby provide area-wide information quite in contrast to rain gauges (see Figure 2.1). A base station sends out radio waves which are reflected by snow, hail, or rain droplets. From the reflected signal

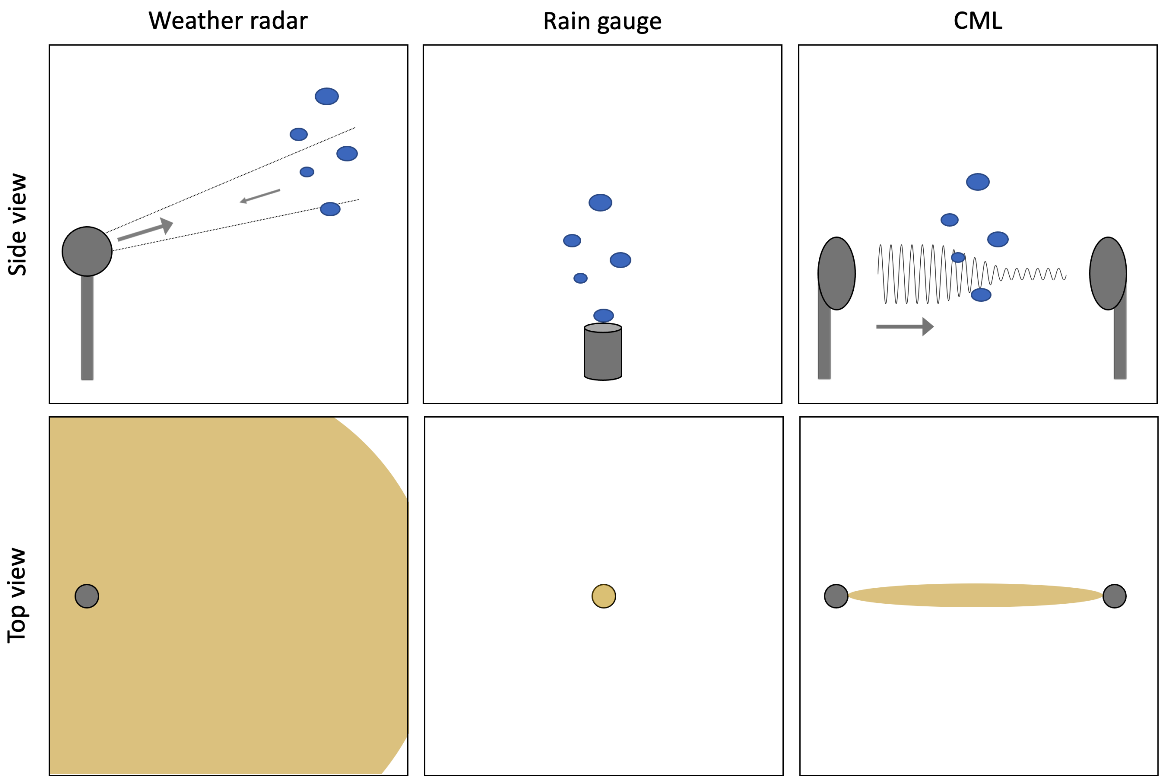

Figure 2.1: Schematic simplified illustration of the operating principles of the three sensor types used in this thesis: weather radar, rain gauge, and CML. The top row shows how rainfall is sensed in side view, and the bottom row shows the area (in dark yellow) that can be observed this way, in top view. The width of the CML observation orthogonal to the path direction is defined by the so-called Fresnel zones and very short compared to the distance between the antennas. The observation is therefore generally considered to represent a simple line. Note that the drawings are not true to scale.

intensity the amount of rainfall can be deduced using the power law relation

$$Z = \alpha R^{\beta} \tag{2.1}$$

where Z is the reflectivity calculated by the observed returned radiation intensity and R the rain rate. The parameters α and β depend on the kind of rainfall and especially the so-called drop size distribution (DSD) (Ulbrich and Lee, 1999). The DSD describes the number of drops of various diameter classes within a volume of air and is a crucial parameter influencing the measurements of remote sensing devices. Typically, the values for α range between roughly 200 and 520 and those of β between 1.2 and 1.8 (Ulbrich and Lee, 1999). Considering the arrival time of the reflected signal also allows the positioning, i.e., the distance of the rainfall from the base station. Thereby, weather radars enable area-wide rainfall estimation in a radius of more than 100 km in the surrounding of the base station. However, the local accuracy is not comparable to that of rain gauges and usually the spatial resolution of radar products is at best 1 km $\times$ 1 km (Ochoa-Rodriguez et al., 2019). Furthermore, it is important to note that several processes such as ground clutter or (partial) beam blockage can corrupt this measurement (Berne and Krajewski, 2013). These effects limit the quality of rainfall estimation from weather radars especially in mountainous terrain. Moreover, the height above the ground of the measurement increases with the distance from the base station and hence the validity of the measurement for the actual precipitation at ground level diminishes. A relatively dense network that involves redundancy through overlapping observations of single radar stations can help to reduce the limitations. However, dedicated weather radars and especially dense networks of these exist only in limited parts of the world.

2.1.2 Used Data Sets

For the studies of this thesis, rain gauge data and a rain gauge-adjusted radar product (RADOLAN-RW[1]) of the German Weather Service (DWD) were used. Both the rain gauge and radar network have a high quality with respect to spatiotemporal coverage compared to the global average. RADOLAN-RW is based on data from 17 dual-polarization doppler radars that provide spatial rainfall information on a 900 km $\times$ 900 km grid with a 1 km $\times$ 1 km spatial and an hourly temporal resolution. The radar information is adjusted to the local information of over 1000 rain gauges via additive and multiplicative correction schemes (Bartels et al., 2004). These rain gauges are partly of the DWD network, but are supplemented by gauges organized on the level of German federal states and also by gauges of the meteorological services of all the surrounding countries. RADOLAN-RW is used as a reference data set throughout this thesis. RADOLAN-RW was chosen for this purpose as it is the official real-time product for quantitative precipitation estimation of DWD and has been used in several studies, such as Graf et al. (2020) and Polz et al. (2020).

Apart from the rain gauges used for the radar adjustment, rain gauges from DWD are also used for generating reconstructions. They are considered as input data in combination with CMLs in one of the two case studies (Chapter 7). The network used for this purpose comprises 953 rain gauges distributed over Germany (see Figure 2.2). These rain gauges provide minutely information on rainfall amounts which are aggregated to hourly amounts for their application in this thesis. Note that this data set is not independent but a subset of the one used for the rain gauge adjustment in RADOLAN-RW.

[1] `https://www.dwd.de/DE/leistungen/radolan/radolan.html`, last access October 13, 2023

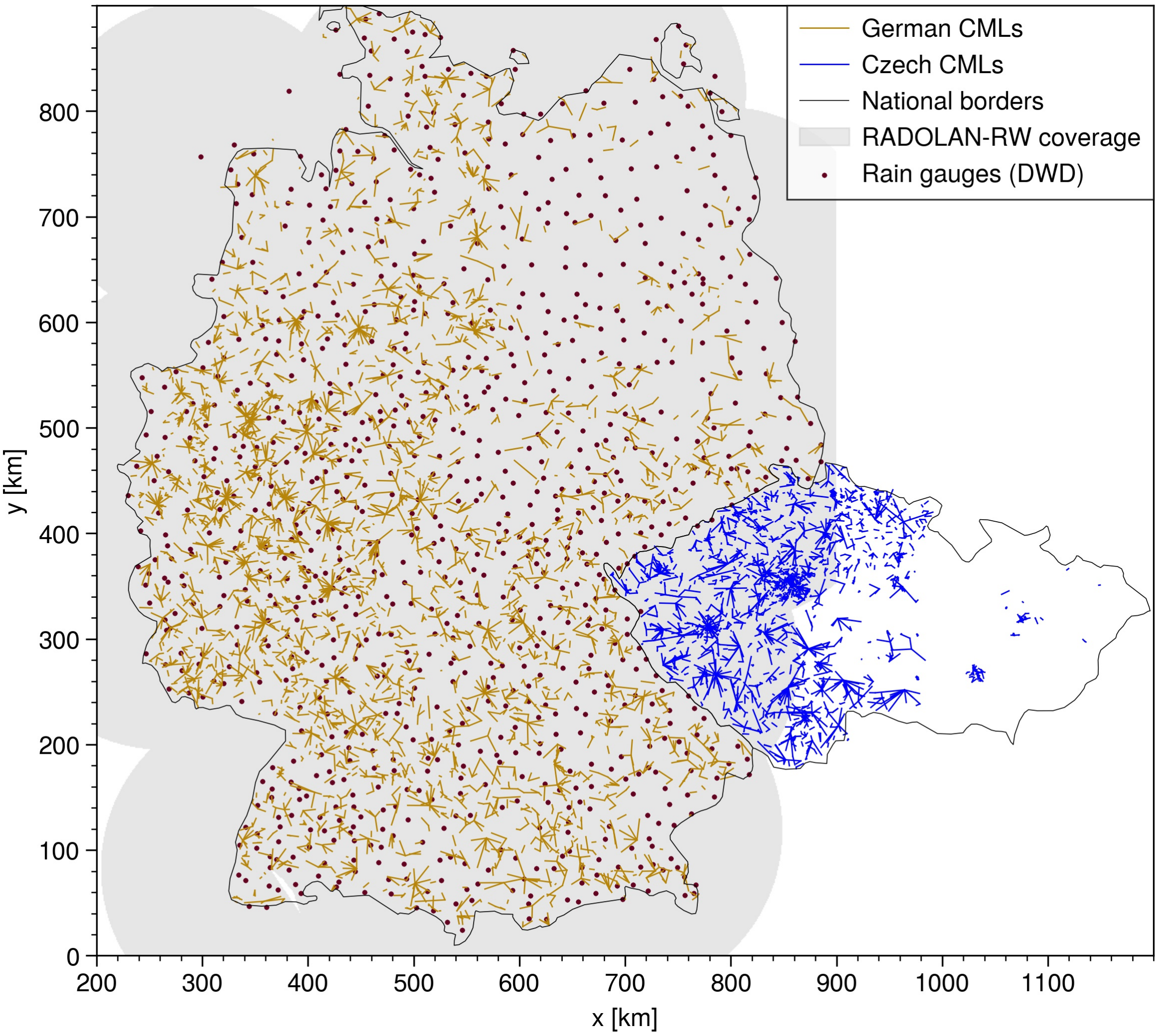

Figure 2.2: Map showing the spatial coverage of all used data. These are rain gauges and RADOLAN-RW of DWD, and CMLs from Germany and the Czech Republic. Note that the limited sensor density in north-eastern Germany and the eastern part of the Czech Republic does not represent a general lack of sensors in those regions, but only a lack of sensors of the particular providers from which the data is obtained. The coordinates represent the distance from the lower left corner of the RADOLAN-RW projection, which is used throughout this thesis.

2.2 Opportunistic Sensors: CMLs

2.2.1 Sensing Principle and Previous Applications

CMLs are part of cellular networks. While such networks can be used for different tasks that require regional data exchange, their typical purpose is the facilitation of cell phone communication. That is, they provide the infrastructure to forward telecommunication data across spatial distances. CMLs as the building blocks of these networks constitute the connection between two specific directional antennas mounted at nodes of the network. The connection is established via the exchange of microwave radiation at frequencies between approximately 5 GHz and 40 GHz (K-band) or 70–90 GHz (E-band). Regarding rainfall estimation the crucial property of this microwave radiation is the fact that it is significantly scattered and absorbed by rain droplets (see Figure 2.1). That is, if it rains along the path of a CML, the signal intensity is attenuated more than it would be without rainfall. Hence, the difference between the transmitted intensity at one antenna and the received intensity at the other antenna allows an estimation of the rain rate along the CML path. This effect, which is undesired from the perspective of the network operator, enables the exploitation of CML data in the realm of rainfall estimation.

The observable raw data of a CML usually consists of transmitted and received signal levels (TSL and RSL, respectively) recorded at the two involved antennas. Typically, values are recorded either instantaneously on minutely or even sub-minutely basis (Chwala et al., 2016; Fencl et al., 2015; Nebuloni et al., 2022), or as minimum and maximum values over a 15-minute period (Messer, 2006; Overeem et al., 2013). Note that the data transmission is bi-directional which means that from both antennas both transmitted and received signal levels can be obtained. The so-called two sublinks of a CML, which refer to the opposing directions, hence provide two sets of observations for the same path. The width of the traversed path, which is defined by so-called Fresnel zones, is very short such that for practical application it is usually not considered. From TSL and RSL of a given sublink, the attenuation (later referred to as total loss or TL) can be calculated. Then, considering aspects such as random noise and attenuation stemming from other sources (see Chapter 3), the data enables the estimation of the average rainfall along the CML path applying the following power-law relation:

$$k = aR^b. \tag{2.2}$$

In Equation 2.2, k is the specific attenuation in units dB/km, R is the rainfall rate in mm/h, a and b are parameters dependent on the frequency and polarization of the radiation, and of the DSD and drop temperature (Olsen et al., 1978). More details about the calculation are given in Chapter 3. A beneficial aspect of this equation for rainfall estimation is that it is almost linear, i.e., b is close to 1, for radiation of approximately 33 GHz frequencies (Atlas and

Ulbrich, 1977). A large part of CMLs operates relatively close to this frequency so that $b \approx 1$ can be assumed for them. Moreover, at these frequencies the equation is rather independent of the DSD (Chwala and Kunstmann, 2019). The *International Telecommunication Union* provides recommendations for values of a and b dependent on frequencies and polarizations (ITU-R, 2005).

While the rain-induced attenuation of microwave radiation of millimeter wavelengths has been known for many decades (Hogg, 1968), the usage of CMLs in the realm of rainfall quantification has evolved and become established over the past 15–20 years. The first applications show the potential via comparing the rainfall estimation from seven CMLs in Israel (Messer, 2006) and two CMLs in the Netherlands (Leijnse et al., 2007) to rain gauges and weather radar observations. After these initial studies that focused on feasibility, research has evolved to estimate rainfall maps at various scales considering cities (Fencl et al., 2015), regions (Zinevich et al., 2008; Roversi et al., 2020), or whole countries (Overeem et al., 2013, 2016b; Graf et al., 2020). However, data processing from raw observations to final products has always been a crucial and challenging aspect. The developed algorithms were not always physically based, but often heuristically adjusted to the available data sets. Hence, other studies focused on a better understanding of specific aspects that need to be considered in the processing, like classification of wet periods (Schleiss and Berne, 2010; Wang et al., 2012; Habi and Messer, 2018; Polz et al., 2020), the estimation of attenuation induced by wet antennas (Leijnse et al., 2008; Schleiss et al., 2013; Fencl and Vojtěch, 2018; Valtr et al., 2019; Moroder et al., 2020; Pastorek et al., 2021), or the best application of CMLs in mapping (Goldshtein et al., 2009; Zinevich et al., 2008; D'Amico et al., 2016; Haese et al., 2017; Eshel et al., 2020, 2021). These aspects are described in more detail in Chapter 3 and Chapter 4.

Many studies have focused on Europe or Israel where commonly dedicated observational networks like rain gauges or weather radar are present. However, since early on, it has been clear that the potential of CML-based rainfall estimation is largest in countries where other observations are scarce (Gosset et al., 2016). Burkina Faso provides an example for a country with no weather radar and very limited number of rain gauges, where, conversely, the availability of rainfall is particularly crucial for agricultural management and food security. There, the potential of CMLs for rainfall estimation was first shown by Doumounia et al. (2014) and recently the first purely CML-based rainfall maps have been generated (Djibo et al., 2023). The applicability has also been shown in Sri Lanka (Overeem et al., 2021) and Kenya in combination with satellite data (Kumah et al., 2022).

2.2.2 Used Data Sets

Two different CML data sets are used in this thesis. One of those comprises 3904 CMLs (Ericsson MINI-LINK) from Germany operated by Ericsson. The data is retrieved in real time with a 1-minute resolution (Chwala et al., 2016). The network comprises CMLs with a length distribution ranging from 0.2 km to 29 km whereas 50% (the interquartile range) of CMLs have lengths between 4 km and 11 km. The frequencies range from approximately 7 GHz to 39 GHz with an interquartile range from 19 GHz to 26 GHz (see Figure 2.3). Approximately 90% of the German CMLs have a vertical polarization.

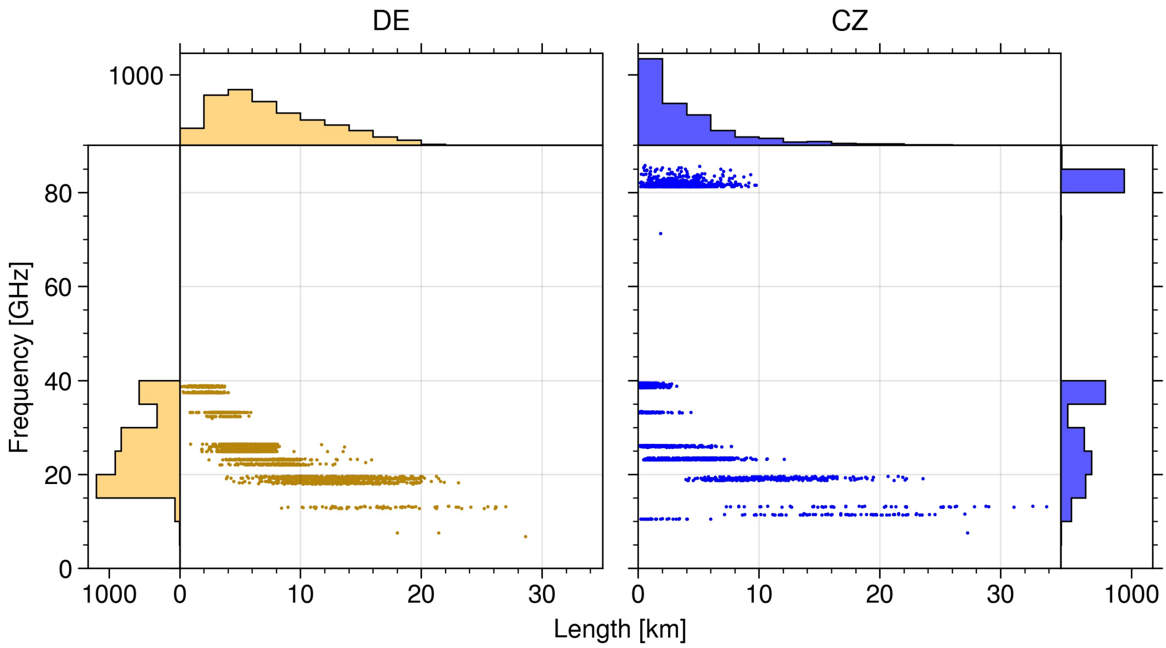

Figure 2.3: Length and frequency distributions of the two used CML data sets from Germany (DE) and the Czech Republic (CZ).

The second data set comprises CMLs from the Czech Republic. These are 2980 CMLs (also MINI-LINK from Ericsson) owned by T-Mobile Czech Republic, which provide data also with a 1-minute temporal resolution. The CMLs are located mostly in the Western part of the country (Figure 2.2). Compared to the German network, the Czech network is distinctly more variable with respect to length and frequency distributions. The lengths range from 0.03 km to 34 km (interquartile range: 1.0 km to 5.4 km) while frequencies range from 8 GHz to 86 GHz (interquartile range: 23 GHz to 81 GHz). The polarization of all Czech CMLs is vertical.

The German data set is used throughout this thesis while the Czech data set is only used in Chapter 6. The exact way of data processing differs among the studies and is explained in the respective Chapters 6 and 7. General aspects of CML data processing are presented in the following chapter.

Chapter 3

Methods: CML Data Processing

CMLs are opportunistic sensors that are not originally designed to provide reliable rainfall information. Hence, there are specific challenges involved in using them for rainfall estimation, which go beyond the ones that need to be considered when using dedicated sensors. This chapter is about these challenges and about common processing steps that enable the retrieval of rainfall information nonetheless. It deals with the aspects that need to be considered to generate path-averaged rainfall information; the aspect of using this rainfall information for spatial reconstructions is then covered in Chapter 4.

Section 3.1 deals with aspects of CML processing in general terms. It does not start with the raw data but also considers the aspect of accessing the data in the first place as this is a crucial procedural challenge in the application of CMLs as rainfall sensors. Regarding the subsequent data processing, the described aspects are rather universal, i.e., related to most CML data. However, the exact way of addressing them is highly adjusted to individual data sets. The common basis of the processing algorithms applied in this thesis is summarized in Section 3.2.

3.1 Deriving Rain Rates from CML Observations

3.1.1 Accessing the Data

In theory, the amount of CML data is enormous. CMLs are very abundant globally as they provide important infrastructure for communication networks that are increasingly deployed around the world. However, in spite of this huge potential, only a very low share of CML data could so far be used for research purposes. The major limiting factor is the difficulties involved in accessing the data. For this, an individual cooperation with the network providers needs to be established and maintained. The network providers, however, generally have no operational advantage in sharing the data. On the contrary, they are usually not inclined to have the locations of the CML antennas publicly available.

Even if access is granted, the technical infrastructure needs to be established to poll and store the data, ideally in real-time. Mounting data loggers at the antennas is usually not feasible due to the involved costs and efforts at least for large data sets (Chwala et al., 2016). Fortunately, the network operators usually store data for monitoring the quality of the connections via network management systems. This data can, from a technical perspective, be obtained relatively easily. However, the obtained data is not necessarily optimal for the usage in rainfall retrieval. Commonly, the data either comprises the instantaneous recording of transmitted and received signal levels (TSL and RSL) (Fencl et al., 2015; Chwala et al., 2016; Andersson et al., 2022) or minima and maxima of signal levels within periods of 15 minutes (Messer, 2006; Overeem et al., 2016b; Nebuloni et al., 2022).

3.1.2 Dealing with Data Quality Issues

The raw CML data obtained from the network provider needs to be investigated thoroughly and not all of it can be used for rainfall estimation. Usually, a considerable part of the data is affected by issues of low data quality.

CMLs can strongly be influenced by multi-path propagation, reflection, or refraction of the radiation (Upton et al., 2005). Also water vapor can lead to attenuation that impairs the observed signal (David et al., 2009; Fencl et al., 2020). Moreover, CML hardware characteristics such as the frequency of radiation and the length (i.e., the distance between the antennas) are crucial aspects affecting the sensitivity to rainfall. CMLs with low frequencies and short lengths, for instance, may not be usable for rain rate retrieval as they are very insensitive. While some CMLs generally provide non-usable data, e.g., based on the hardware characteristics, others may show only periods of bad quality. Sometimes the reasons for issues of data quality can be explained at least partly by physical (atmospheric) phenomena such as dew, wind, temperature or insolation, but sometimes they cannot. Some issues may instead depend on technical details of data logging or aspects of the engineering that are hardly identifiable without consultation with the network provider; such consultation, however, is generally not envisaged and not feasible under common arrangements between research institutions and the providers.

The data quality issues usually manifest as fluctuations, spikes, steps, drifts, or gaps in the time series of the raw data (see Figure 3.1). Unreliable CMLs are commonly filtered from the analyses in research applications. Fencl et al. (2015), for instance, did this filtering based on visual inspection which, however, is only possible in relatively small data sets. Overeem et al. (2013), Overeem et al. (2016b), and Roversi et al. (2020) remove CMLs based on the observations from the vicinity, and Graf et al. (2020) developed a routine that takes into account the rolling standard deviation of each CML's time series to filter those with high amount of fluctuations that cannot be caused by actual rainfall. Other more technical quality issues like implausible metadata or missing time steps are also addressed in Overeem et al. (2016a) and Graf et al. (2020).

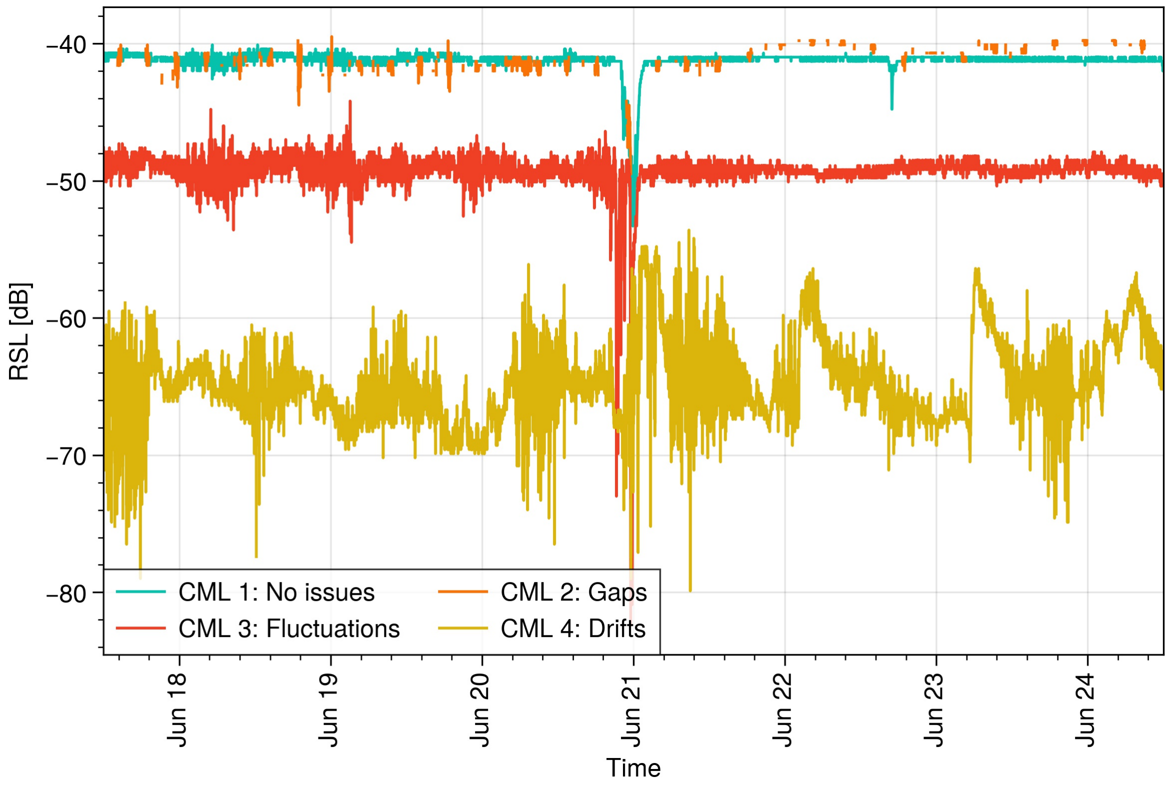

Figure 3.1: Examples of RSL time series of four different CMLs for a period of one week. One CML shows no apparent issue with respect to data quality while the others display data that is impractical to use for rainfall retrieval. Shown issues comprise: many gaps, strong fluctuation, or drifts in a diurnal pattern. The actual rain rate retrieval for the one CML without issues is shown for one rainfall event in Figure 3.2. Note that absolute RSL values can vary significantly between different CMLs which is why information about TSL is needed in addition.

3.1.3 Rain Rate Retrieval

Once a *clean* data set is available after quality control, the process of rain rate retrieval can begin. Although the erroneous data has been removed at this stage, noise is still present. Hence, the retrieval part involves several steps like the detection of rain events, the account for the background attenuation, and the correction for the attenuation induced by wet antennas. Considering these aspects is mandatory in order to estimate the attenuation that is actually induced by rainfall. Finally, the rain-induced attenuation is used to calculate the average rain rate along the CML path.

The recorded data consists of TSL and RSL either instantaneously sampled or given as minima and maxima over usually a 15-minute period. Often these signal levels are not independent of each other: that is, the TSL may be increased for compensation via automatic transmit power control (ATPC) when the RSL drops. In this case, the difference of TSL and RSL, referred to as total loss (TL)

$$TL = TSL - RSL \tag{3.1}$$

is required for inferences on rainfall. If no ATCP is active, the TSL values are mostly constant and hence the RSL values can be used directly (Overeem et al., 2016a).

Naturally, the signals are not free of random noise. In order to not estimate low rain rates at every noisy period, the actual rainy periods need to be detected. More precisely, it is important to classify every part of the time series as either *wet* or *dry*. A wrong balance of this classification can easily lead to overestimation and false positives, or underestimation and false negatives. Many approaches have been proposed to perform such a classification. Some of those are based on the patterns observed in the time series of single CMLs via classifying periods of high variability: via Fourier transform (Chwala et al., 2012), the rolling standard deviation (Schleiss and Berne, 2010; Wang et al., 2012; Graf et al., 2020), or machine learning in the form of convolutional neural networks (Polz et al., 2020). Furthermore, there are approaches that consider the information from neighboring CMLs (Overeem et al., 2016a) or from transmission errors (Habi and Messer, 2018). Also, other data sources like rain gauges are used for this step (Fencl et al., 2015).

The signal of CMLs is always attenuated, that is, TSL is higher than RSL even if it does not rain along the path. Hence, after the wet periods are identified, a baseline level (BL) needs to be defined for those periods. This BL can be subtracted from the TL. The approaches to define the BL depend on the way the data is recorded but usually consider a constant level (Roversi et al., 2020; Graf et al., 2020), or a linear interpolation between the end and start of the previous and following dry period, respectively (Fencl et al., 2015). The BL level is usually estimated for each rainfall event individually, as it can shift in between the events.

Another crucial aspect that needs to be accounted for, is the attenuation induced by wet antennas. Obviously, antenna covers often get wet during rainfall events that affect a CML. The wetness induces additional attenuation, which needs to be subtracted to derive the rain-induced attenuation. Methods to account for this wet antenna attenuation (WAA) range from considering a constant amount of WAA during the whole rainfall event (Overeem et al., 2011; Fencl et al., 2015) to more complex functions that depend on time (Schleiss et al., 2013), or on the rainfall intensity, CML hardware characteristics, and antenna properties (Leijnse et al., 2008). Other rain rate dependent approaches have been presented by Kharadly and Ross (2001) and Pastorek et al. (2021). Note that despite the amount of methods and the related research, a comprehensive physical explanation and a universal model for WAA is not yet available and many challenges remain (Tiede et al., 2023). The estimated WAA is subtracted from the remaining signal during the wet periods. In short,

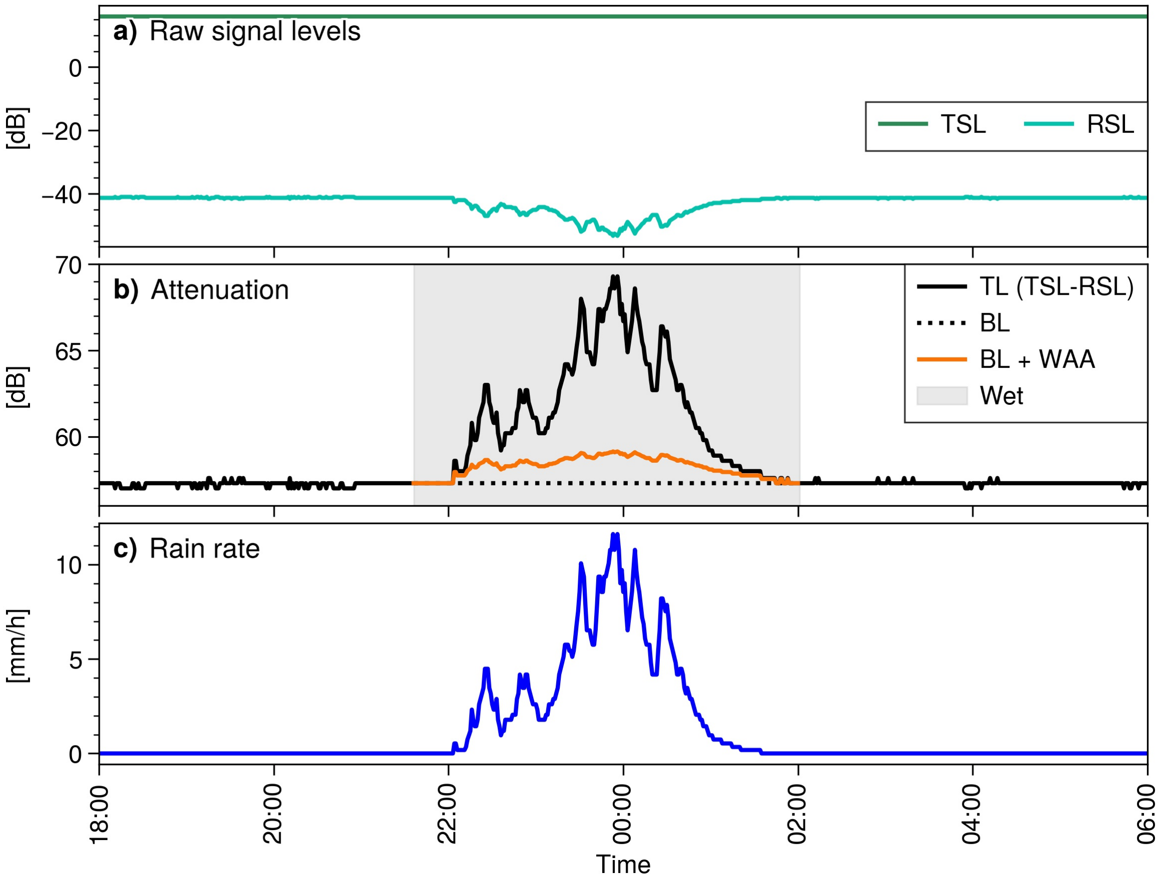

Figure 3.2: Exemplary rain rate retrieval for a CML time series of 12 h (a subset of the time series labeled *CML 1* in Figure 3.1). a) The raw data TSL and RSL. b) The attenuation TL, the period classified as wet, the estimated BL level and the estimated effect of WAA. c) the estimated path-averaged rain rate.

rain-induced path attenuation is considered to equal

$$A_R = TL - BL - WAA \tag{3.2}$$

and can then be used to calculate the path-averaged rain rate $\overline{R}$ in mm/h. First, A_R in dB can be expressed as the integral of the specific attenuation k in dB/km by

$$A_R = \int_0^G k(g)dg \tag{3.3}$$

where G is the CML length. By inserting the power-law relation defined in Equation 2.2, this can be formulated as

$$A_R = \int_0^G aR(g)^b dg \tag{3.4}$$

where $R(g)$ is the rainfall along the CML path. Since linearity of the power-law relation, that is $b \approx 1$, can be assumed for typical CML frequencies (Atlas and Ulbrich, 1977), Equation

3.4 can be simplified to

$$A_R = a\overline{R}^b G. \tag{3.5}$$

Simple rearrangement provides a value for the path-averaged rain rate:

$$\overline{R} = \left(\frac{A_R}{aG}\right)^{\frac{1}{b}} \tag{3.6}$$

The parameters a and b are dependent on CML frequency and polarization and can be retrieved from literature recommendations like the one provided by the *International Telecommunication Union* (ITU) (ITU-R, 2005) or fitted to reference data. Following the equations above, it becomes clear that the rain rate retrieval procedure is strongly influenced by the CML characteristics, that is, its frequency, length, and polarization.

3.2 Basis of the Applied Quality Control and Rain Rate Retrieval

The following describes the specific algorithms that are conducted in this thesis to account for the challenges addressed above. The processing described here is taken from Graf et al. (2020) who developed it for the same CML data from Germany that is used in this thesis. They adjusted the processing considering one year of data from September 2017 to August 2018. Their approach is applied in all the case studies of this thesis. However, specific extensions to the procedure will be introduced and applied both in Chapter 6 and Chapter 7. The whole algorithm considers the time series of each CML individually and uses the functionality of the Python-based software package pycomlink (Chwala et al., 2021).

The quality control starts with the removal of numerical *fill* values. Moreover, short gaps of up to 5 minutes in the time series are interpolated linearly. To account for fluctuations on different time scales two criteria are considered: For each CML, it is first tested whether the 5-hour rolling standard deviation of the TL time series exceeds 2 dB at least 10% of the time. Secondly, it is tested whether the 1-hour rolling standard deviation of the total loss exceeds 0.8 dB at least 33% of the time. The CML is removed from the analysis if it fulfills at least one of these criteria.

The classification of wet events is based on the variability of the TL time series. The applied approach is a modified version of the one presented in Schleiss and Berne (2010). The threshold value that separates low from high variability, and thereby dry from wet periods, is defined as

$$l = 1.12 \cdot q_{80}(std_{roll(60)}(TL)) \tag{3.7}$$

where $q_{80}(std_{roll(60)}(TL))$ is the 80^{th} percentile of the 60-minute-rolling standard deviation of TL. While the 60-minute period is adopted from Schleiss and Berne (2010), the 80^{th}

percentile is chosen heuristically: based on the assumption that it is generally dry a least 80 % of the time in the German climate, the 80$^{\text{th}}$ percentile represents fluctuations that are rather strong but most certainly not related to rainfall. The factor 1.12 accounts for a CML-independent adjustment and was fitted by Graf et al. (2020) to a subset of the data they used. Wet time steps are those for which the 60-minute-rolling standard deviation of TL exceeds l.

After the classification of wet and dry time steps, the BL for each time step is calculated. The BL is considered constant and equal to the last TL value before the given event started. The WAA correction is based on the estimation originally proposed by Leijnse et al. (2008). It assumes that WAA is dependent on water cover on the antennas which in turn is dependent on the rain rate via a power law relation. Moreover, frequency and antenna cover properties are considered (see Leijnse et al. (2008) for the exact formulation of the equations).

Finally, the rain rate is calculated via Equation 3.6 with the parameters a and b derived from the ITU recommendations (ITU-R, 2005). For the purpose of generating maps and comparison to the reference, the minutely rain rates in mm/h are aggregated to hourly rainfall amounts in mm.

Chapter 4

Methods: Spatial Reconstruction of Rainfall

This chapter is about the generation of rainfall reconstructions. First, fundamental theoretical aspects and several challenges specific to this thesis are introduced in Section 4.1. Then, the applied methods are described: Section 4.2 presents the standard methods Inverse Distance Weighting (IDW) and Ordinary Kriging (OK) and, finally, Random Mixing (RM) as the central reconstruction method of this thesis, is presented in Section 4.3.

4.1 Concepts and Challenges

4.1.1 General Purpose of Spatial Reconstruction

The term *spatial reconstruction* or just *reconstruction* is used in this thesis for the result of interpolating rainfall values in two-dimensional, horizontal space, i.e., generating a rainfall map. In other words it is the process of deriving gridded data from scattered data. First, a grid is defined that determines the resolution at which the reconstruction shall be conducted. Based on the local scattered observations of rain gauges or CMLs a value is computed at every grid point via one of the methods described below. This value is assumed to represent the surrounding grid cell such that discretized area-wide information is available. Note that such a reconstruction is generally not restricted to a two-dimensional field but can be carried out in more dimensions, e.g., when considering vertical height. However, the spatial reconstruction considered in this thesis is restricted to two-dimensional regular grids representing the land surface. A simple setting is illustrated by 16 grid cells, one rain gauge, and one CML observation in Figure 4.1.

Spatial rainfall information is crucial for all hydrological applications. The local observations are not sufficient to predict the water volume that enters a river system, for instance. Hence, reconstructions are an essential part of rainfall estimation.

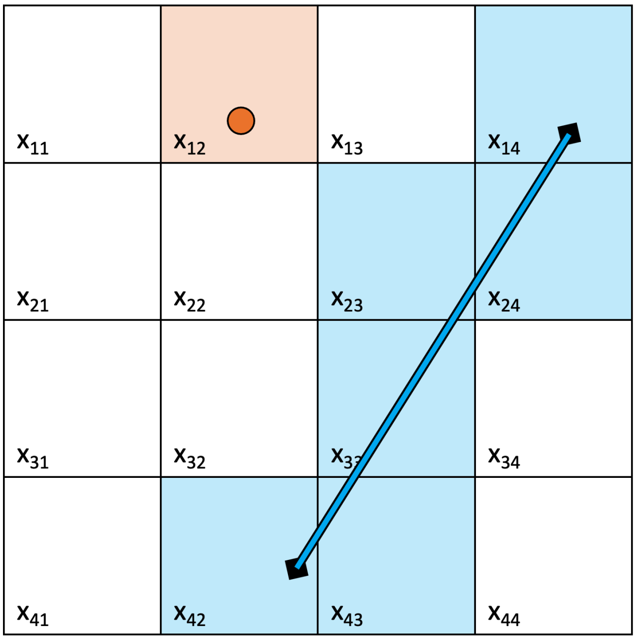

Figure 4.1: Minimal example to illustrate the goals and challenges of spatial reconstruction using rain gauges and CMLs. One rain gauge is represented by the orange circle and one CML by the blue line. While the rain gauge can be assumed representative for the grid cell it is in, it is less certain how to use the path-averaged information from the CML for the grid cells which are intersected by it, and even less certain what values may be estimated for the grid cells far away from the observations.

The basic prerequisite that enables reconstructions in the first place is a nonzero spatial auto-correlation, which is generally assumed to decrease with distance. That is, locations that are close to each other are likely to have experienced rather similar rainfall amounts. This characteristic allows estimates about the value at a location based on a value at a nearby observed location. Spatial auto-correlation can certainly be assumed for rainfall, and hence, local observations contain information about their surrounding. However, the spatial variability of rainfall is high, which means that the auto-correlation and thereby the certainty of an estimation drops fast with increasing distance from the observation. A basic challenge in the process of reconstructing is to determine a model for the degree of auto-correlation. That is, relating to the example of Figure 4.1: How much does the rain gauge observation affect the nearby grid cell x_{22} and how much still the farther away grid cell x_{32}? Considering the path-averaged CML information, these questions are even more difficult to answer.

As a first approach, a reconstruction can be achieved straightforwardly by various kinds of methods such as nearest-neighbor interpolation, (bi)linear interpolation, (bi)cubic interpolation, or triangulation. These methods usually expect observations that can be represented as points. Considering the data used in this thesis, the assumption of representing point data can readily be made for rain gauges. For path-averaged CMLs, it is less straightforward, but can be achieved, e.g., via considering the midpoints along the paths as virtual gauges. Such techniques can generate reconstructions that fit to the observations locally, however, the rainfall maps do generally not represent real rainfall as they do not have value distributions and spatial patterns that fit those of actual rainfall. Moreover, such reconstructions do not account for uncertainties involved in the process of deriving values at unknown locations. Before proceeding to more sophisticated methods, it is important to state what the specific goals for a reconstruction are.

4.1.2 Specific Goals of Spatial Reconstruction

Optimally, the reconstruction should fulfill the following goals:

- respect the observations locally
- respect the rainfall statistics
  - the correct marginal distribution
  - the correct spatial dependence structure
- quantify uncertainties

Obviously, the reconstruction should respect the observations, that is, at the locations where observational information is available, the reconstruction should have similar values as the observed ones. This is relatively straightforward to achieve for rain gauges if one considers the rain gauge representative for the pixel of the grid on which it is located. As stated above, this goal cannot be treated in the same way for path-averaged CML observations. The challenge of accounting for CML information in reconstructions is specifically addressed in Section 4.1.4.

If the reconstruction fits to the observations at their locations, it is, however, not necessarily a good solution yet. Another important aspect needs to be considered, which is the rainfall statistics (commonly also referred to as prior information, Zhou et al. (2014)). Here, the rainfall statistics are defined as being composed of the marginal rainfall value distribution on the one hand, and the spatial dependence structure on the other hand. In other words, the reconstruction should be in agreement with the observations not only at their locations but also it should share the statistical properties considering the full data amount. Optimally in fact, the rainfall statistics of the reconstruction would additionally be similar to general information on rainfall, perhaps taking into account the regional and temporal climatic rainfall characteristics.

Finally, it should be considered that it is impossible to generate a single perfect reconstruction for each event and each location. Inevitably, there are uncertainties involved in

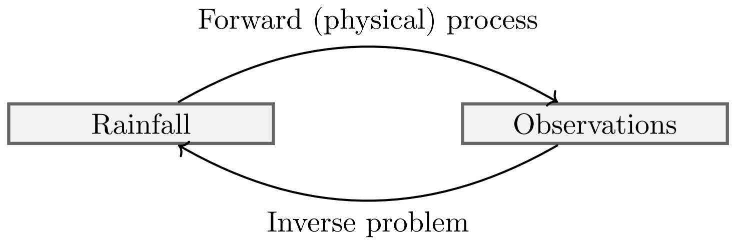

Figure 4.2: Illustration of the inverse problem. The physical process can be described by rainfall inducing observations. Hence, rainfall reconstruction is an inverse problem and as such involves several challenges.

the generated rainfall maps, even when assuming a perfect quality of the underlying data. Hence, the reconstruction method ideally provides a way to quantify these uncertainties.

Achieving all the outlined goals makes the generation of high-quality reconstructions a complex task. The limited area that is actually observed and the high spatial variability and intermittency of rainfall leave room for considerable uncertainty. The following provides useful concepts to address these challenges.

4.1.3 Inverse Problem Theory and Geostatistics

The challenge of reconstruction can be conceptualized as finding a linkage between the physical phenomenon (rainfall) and the observations. A forward model would represent the processes that lead from rainfall to observations. The goal pursued here, however, is to model rainfall starting from the observations which constitutes an inverse problem (see Figure 4.2). Tarantola (2005) defines inverse modeling as "use of the actual results of some measurements of the observable parameters to infer the actual values of the model parameters" (p. 2). In this regard, rainfall is the model parameter and the information from rain gauges and CMLs are the observational parameters.

A common feature of inverse problems is that they are ill-posed (Kabanikhin, 2012) which means that the solution is not existent, not unique, or not stable. Particularly, uniqueness is often not attained (Zhou et al., 2014). In the case of this thesis, the uniqueness is also not given: many reconstructions are imaginable based on a given set of observations. Such problems are usually addressed by algorithms that involve optimization. This means that reconstructions are ideally not deterministic solutions but represent the random uncertainties.

Methods that deal with such problems can be summarized under the term of geostatistics. The major factor distinguishing geostatistics from simple interpolation is that only the former treats the model parameter as a random variable. It assumes that the variable can be described by a random function at every point in space. More generally, Chilès and Delfiner (2009) describe geostatistics as "the application of probabilistic methods to regionalized variables" (p. 2). Geostatistics is a field initiated by works as that of Matheron (1965) and had its origin in the mining industry where problems are usually three-dimensional. Nevertheless, the concept is used in vast areas of all the geosciences, and is applicable to two-dimensional problems like the reconstruction of rainfall maps.

In geostatistics the notion is that a regional variable (which is rainfall in the present case) constitutes one of many possible realizations of a random function. This implies, for example, that observations at their given locations are one of many possible realizations. Furthermore, it is assumed that the random function is similar across space. More precisely, the assumption of intrinsic hypothesis states that expected value and variance of the random function remain unchanged regardless of the location (Abzalov, 2016). This assumption provides the link in space: When coupled with a function about the spatial auto-correlation, the probabilistic values at unobserved locations can be estimated. Theoretical semivariograms are functions that describe the variability in relation to the distance between two locations. That is, they are a model of the spatial dependence structure and provide a crucial foundation of geostatistics methods. Formally, a theoretical semivariogram is a function of the following form

$$\gamma(h) = \frac{1}{2} var(\Omega(x) - \Omega(x+h)) \tag{4.1}$$

where $\gamma(h)$ describes the variance of the parameter (e.g., hourly rainfall amount) dependent on a separation vector h. $\Omega(x)$ is the parameter value at the location x, $\Omega(x+h)$ the parameter value at location $x+h$, and $var()$ the variance function. A semivariogram function cannot be found this way in practice since not every location is observed and since the variability does not only depend on distance. Empirical semivariograms are usually obtained by calculating the variance for several distance classes and by fitting a semivariogram model to this data. Note that some ambiguity about the usage of the terms *semivariogram* and *variogram* (formally, twice the *semivariogram*) exists (Bachmaier and Backes, 2011) which is often not crucial in a conceptual application.

Empirical semivariograms can be estimated in various ways. For example, they are the result of calculating the variances between observations within classes of similar separation distances. Important characteristics describing the shape of the semivariogram function are *nugget*, *range*, and *sill*. The nugget accounts for random variation at zero distance displaying measurement uncertainty or variation below the level of resolution, the range accounts for the maximum distance in which there is correlation observable, and the sill accounts for the variation of values that are not spatially correlated, i.e., which are farther apart than the distance defined by the range.

A major advantage of geostatistical approaches and the application of semivariograms is that they provide a way to generate rainfall maps that follow a certain spatial dependence structure throughout the map extent. Under the assumption of second-order stationarity

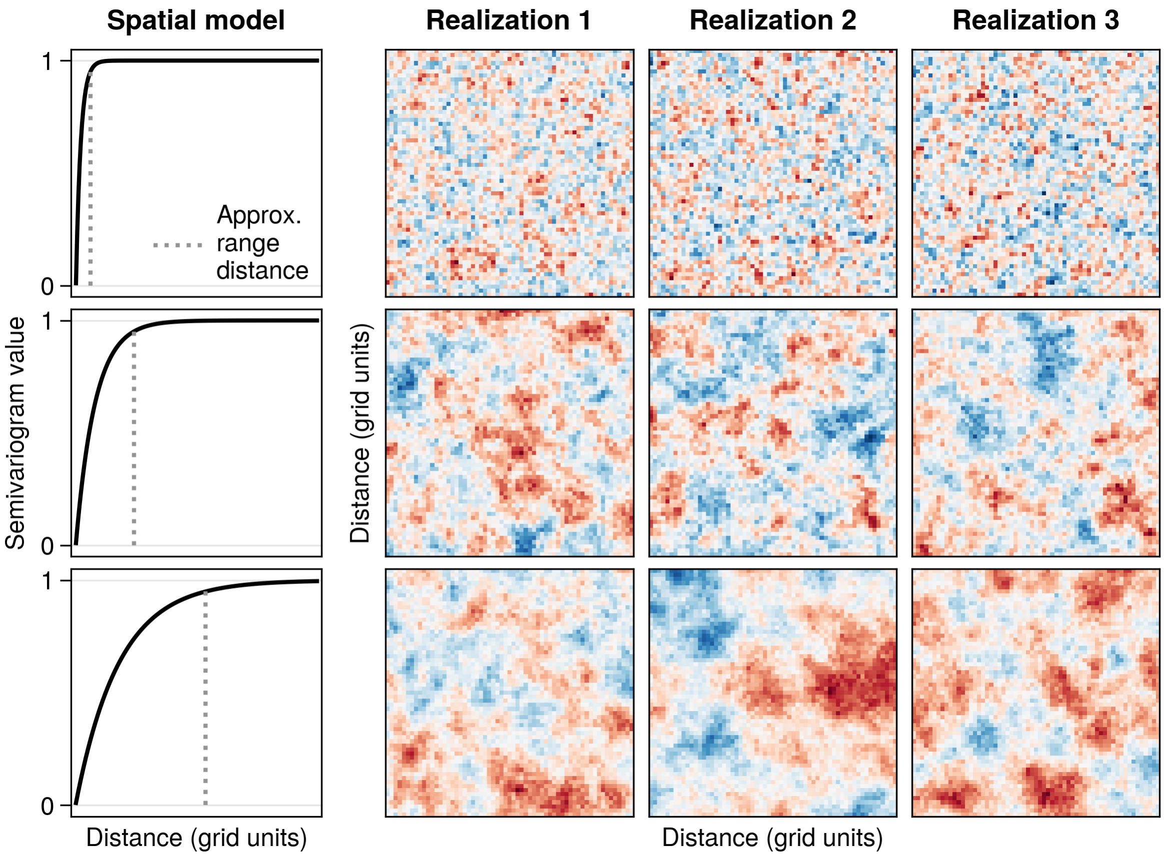

Figure 4.3: Examples of fields with a standard normal value distribution for three semivariogram models. Each semivariogram can be used to generate fields of a certain spatial dependence structure. All models in this figure have a nugget of zero and a sill of 1. As the sill is only approached asymptotically, the range parameter is defined by the distance at which the semivariogram value exceeds 95% of the sill. All fields (realizations) in a particular row are different with regard to the locations of high (red) and low (blue) values, but they have a similar spatial pattern. From top to bottom row the spatial dependence (auto-correlation) increases so that in the lower rows larger clusters of either high or low values exist.

the variogram is directly linked to the covariance of a field (Journel and Huijbregts, 1978). Hence, fields of a certain spatial structure can be derived from a semivariogram model. This aspect can be considered without any local constraints of data. Figure 4.3 shows several semivariogram models and related fields: While the location of high and low values differs among all fields, the spatial structure is similar if based on the same semivariogram model.

A particular class of geostatistic methods is composed of techniques that generate solutions in a stochastic manner (Zhou et al., 2014). They are similar to other geostatistic methods as they consider the variable the result of a random process. However, stochastic methods do not attempt to find a single optimal solution. They respect that there is variability and that different solutions may equally well represent the true situation, which is unknown. Hence, these methods enable the estimation of ensembles consisting of many equally valid solutions. The distribution of such ensemble members provides probabilistic results and the possibility for the quantification of uncertainties. Stochastic methods constitute the most sophisticated approach to fulfill all the goals outlined in Section 4.1.2.

4.1.4 Specific Challenges of CML-based Reconstruction

As mentioned before, there is not one best solution for using CML-based path-averaged rainfall information for spatial reconstruction. When CMLs are considered as virtual gauges at the center of the link paths as done in many studies (e.g., Overeem et al. (2016b); Graf et al. (2020); Roversi et al. (2020)), it is obviously not accounting for the full information and the related uncertainties about the exact position and amount of rainfall. For instance, if a CML is several tens of km long, the average rain rate does not tell whether the rainfall was close to the one antenna, or to the other, or, whether it was equally distributed along the path. Similarly, it may not reveal very high rain rates that affect only part of the CML paths as these get lost in the process of averaging. This effect is theoretically more problematic the larger the CML length and the shorter the range of the semivariogram model are. The effect of averaging along the path and thereby reducing the extreme values, is particularly problematic as many reconstruction methods involve reducing extreme values even further. This also implies that it is impractical to estimate the precise marginal distribution of rainfall via CML observations.

Aside from the challenges related to path-averaging, also the network topology is not necessarily optimal for generating maps. The individual CMLs are generally not equally distributed in space which results in areas with higher and lower sensor density. For example, the amount of sensors is commonly much higher in urban areas (Uijlenhoet et al., 2018). Moreover, the arrangement often is such that one central node is connected to several nodes, which leads to irregular clusters of observation. With low network density, the uncertainties of the reconstruction are larger, and the area for which a single CML is assumed to be representative is higher.

Despite the mentioned challenges, there are also benefits of the specific characteristics of CML observations. For instance, the path-based information of individual CMLs can represent greater areas than rain gauges and the total amount of data is often large. Hence, to make use of the opportunities, the challenges should ideally be addressed appropriately.

4.2 Deterministic Approaches: Inverse Distance Weighting and Ordinary Kriging

A popular straightforward approach of reconstruction via simple interpolation is Inverse Distance Weighting (IDW). The algorithm is the following: For a specific grid point, one considers a set of neighboring observations and calculates the weighted mean of those neighbors. The weights for each observation are estimated dependent on the distance of that observation to the grid point of interest, i.e., higher for nearby and smaller for far observations. IDW is straightforward at the cost of not considering the overall value distribution and spatial correlation, and not accounting for uncertainties. Extrapolation, that is generating values outside the range of measured values, is not possible.

The method is applicable to point data like rain gauges. Therefore, using IDW with CML data requires the path information be reduced to a virtual gauge. For the application of IDW in Chapter 6, the path-averaged values are hence assumed to be represented by the midpoints along the paths, as was also done by, e.g., Graf et al. (2020). Moreover, a maximum distance in which neighbors are considered is set to 30 km. The simple IDW method is applied in this case study as the focus there is on the transferability of processing algorithms and not on the details of reconstruction quality.

More sophisticated reconstructions can be achieved via Kriging methods. These are geostatistical methods which date back to independent works of Matheron (1965) and Gandin (1966). Kriging is arguably the most popular geostatistical method. It is, in fact, inseparable from the origin of geostatistics and the central aspect of traditional geostatistics. Kriging estimates spatial variability based on a semivariogram. It generates reconstructions in a deterministic way by considering the neighbors but also the spatial dependence structure and redundancy of observations. Even in more advanced methods that have evolved over the past decades, Kriging often plays a role as a sub-algorithm (Zhou et al., 2014).

In this thesis Ordinary Kriging (OK) is applied as a reference method in Chapter 7. OK is a Kriging variant in which the mean value is assumed to be unknown but constant over the neighborhood of the location that is being estimated. However, this assumption is not necessarily justifiable for rainfall due to its high spatial variability. That is, OK involves limitations that can be particularly severe in its application for rainfall estimation. Nevertheless it is widely applied in this context. In this thesis, the *PyKrige*[1] Python package (version 1.6.1) is applied, with an exponential semivariogram model and a moving window that considers the ten closest points. The parameters of the semivariogram are calculated by the package's default L1 norm minimization scheme. Like IDW, OK requires point data. Hence, also for OK the CML observations are reduced from path-averages to virtual gauges at their midpoints, similar to what was done by, e.g., Overeem et al. (2013, 2016b). OK generally allows the creation of values that are outside the range of observations. In its application, this led to nonsensical negative rainfall values in a few cases, which were set to zero prior to the analyses.

[1] `https://pypi.org/project/PyKrige/`, last access October 13, 2023

4.3 Stochastic Approach: Random Mixing (RM)

4.3.1 Introduction to RM

Random Mixing (RM) is a stochastic reconstruction approach that enables solving inverse problems and was first presented by Bárdossy and Hörning (2016b). It is based on the gradual deformation approach (Hu, 2000) but enables the consideration of parameters that do not exhibit a normal distribution. RM was originally developed to deal with challenges of inverse groundwater modeling (e.g., Bárdossy and Hörning (2016a)). In groundwater modeling there are linear and nonlinear constraints, e.g., hydraulic transmissivities and hydraulic head values, respectively. Later, it was found that the methodology also suits spatial rainfall estimation. Although rainfall has different statistical characteristics such as a different marginal distribution and spatial correlation, and different kinds of observations, the method proved to be applicable: Haese et al. (2017) used RM with a combination of rain gauges and CMLs on the scale of rather small river catchments. The point-like rain gauge observations can be considered linear constraints and the path-averages of CMLs nonlinear constraints. The mentioned study of Haese et al. (2017) showed benefits of RM over OK for reconstructions of maps for the small catchments. RM has been evolving over recent years and a notable technical improvement was the usage of the Whittaker-Shannon algorithm for faster optimization (Hörning et al., 2019).

A major benefit of RM is that it can account for such different constraints as those of point-like rain gauges and path-averages from CMLs, and that these can be regarded without corrupting the overall statistics of the field. Importantly, RM does not require the input data to follow a standard normal distribution, which rainfall (among many other variables) does not follow, indeed. To be suitable to problems of variables that are generally not distributed in a standard normal manner, a transformation from the actual values space to the standard normal space and its inverse need to be defined. For estimating the spatial dependence structure, RM makes use of copulas which are invariant to the marginal distribution and therefore outliers in the data (Nelsen, 2006). It is an important step towards generalization that the distribution in real space needs only be describable by a Gaussian copula (Bárdossy and Li, 2008). Furthermore, being stochastic in nature, RM allows for variability at unobserved locations, that is, at locations without any measurement as well as along the CML paths. Hence, there is not only one solution but the possibility to calculate ensembles of reconstructions which enables the quantification of uncertainties. In summary, RM can be used to reconstruct rainfall fields that represent gauge observations locally, account for CML observations, fulfill the rainfall statistics as inferred from the data, and provide a probabilistic solution. Hence it is capable of addressing all the goals defined in Section 4.1.2.

4.3.2 The Core Principle of RM

RM, like gradual deformation, works in standard normal space. That is, it first generates fields that have a standard normal value distribution and a spatial dependence structure that fits to the data.

Let $UF_i(x)$ be a number of unconditional random fields consisting of values for each grid location x. The UF_i are random as they do not account for any observations. However, all UF_i are constructed such that they have a standard normal marginal distribution, i.e., expected values $E(UF_i) = 0$ and variance $var(UF_i) = 1$, and a spatial correlation defined by a covariance matrix Γ equal for all UF_i. Then, a linear combination

$$NF = \sum_i \alpha_i UF_i(x). \tag{4.2}$$

constructs a new field with the same expected value, i.e., $E(NF) = 0$. By enforcing that the scalar weights α_i fulfill

$$\sum_i \alpha_i^2 = 1, \tag{4.3}$$

it follows that also $var(NF) = var(UF_i) = 1$ and $\Gamma_{NF} = \Gamma_{UF_i}$, which means that also the spatial dependence structure is preserved.

There are an infinite number of solutions for such NF. The observations can hence be used as additional constraints. This is done for linear constraints and nonlinear constraints separately. The field NF can also be expressed as

$$NF = IF + HF, \tag{4.4}$$

that is, as the sum of two fields, whereas IF and HF are each weighted linear combinations of unconditional fields UF_i. This formulation allows for the considering of linear constraints at their locations in IF, and adding random noise at other locations via HF (see Section 4.3.3 for the details). IF and HF do not each need to be of unit variance, that is, they do not need to have weights that fulfill Equation 4.3. However, their weights need to be chosen such that the combined weights guarantee unit variance for NF.

Linear constraints (rain gauge observations) are transformed to standard normal space before conditioning. Nonlinear constraints (CML observations) are regarded as the actual rainfall values and compared to the fields after these are back-transformed from their standard normal distribution to actual rainfall values. Repeated random selection of the unconditional fields in various linear combinations, constitutes the stochastic element of the approach.

4.3.3 The Algorithm as a Python Implementation (RMWSPy)

In the previous section, the core principle was briefly outlined. This section, in contrast, is a more detailed description of the algorithm according to the Python implementation (Hörning and Haese, 2021), or more precisely, its adaptation used in this thesis (Hörning and Blettner, 2022). Also the naming convention used here is partly adopted from the implementation. Figure 4.4 presents the algorithm in a flowchart whereas the shown numbers refer to the steps of the algorithm as defined below.

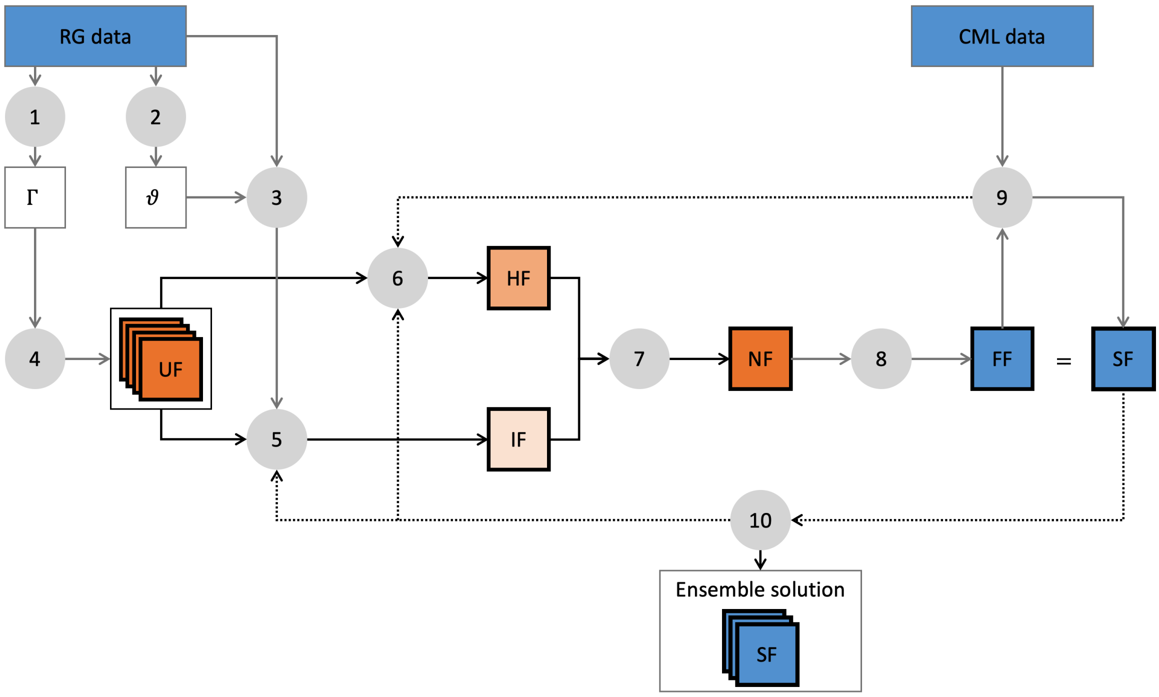

Figure 4.4: Random Mixing flowchart. Starting point is the rain gauge (RG) input data. The fields are indicated by squares with thick contours. Data and fields are colored according to their value space: orange for standard normal space and blue for actual rainfall. The intensity of orange color indicates the variance of the fields (while all *UF* and *NF* have a variance of 1, *HF* and *IF* have lower variances). Black solid arrows indicate linear combinations, dotted arrows indicate repetitions, and gray arrows all other processes. The encircled numbers refer to the steps described in Section 4.3.3.

Preparation: Locate the Observations on the Grid

Let P be the number of rain gauges and $(v_p)_{p\in[1..P]}$ their observed values. Moreover, let Q be the number of CML observations and w_q their path-averaged values. First, the locations of the observations need to be adjusted to a regular rectangular grid. For this, each rain gauge observation is shifted to the nearest grid point at the locations x_p. The CML locations are defined by the positions of the antenna pairs. To account for their full paths, the Bresenham Line Algorithm is applied which defines the pixels that are intersect by each path. While the v_p are used in several of the following steps, the usage of the w_q is described in Step 9 at the end of the algorithm.

Step 1: Derive the Spatial Dependence Structure

The observations from the rain gauges are used to estimate the spatial dependence structure represented by the covariance matrix (Γ). The covariance matrix is derived from a semi-variogram model that consists of a nugget, range, sill, and a core function that describes the variability dependent on the distance (e.g., the spherical or exponential function). In the standard normal value space the sill is always equal to 1. The nugget is predefined in the used implementation. Hence, the estimation of Γ requires only to find an appropriate range parameter and a core function, which are estimated in an iterative procedure. For this purpose, the values of the rain gauge observations are transformed to rank values of the interval $(0, 1)$ and grouped into random subsets of spatially close members. Then, the density of a Gaussian copula is computed for various combinations of a) the core functions, b) the range parameter, and c) arrangements of spatial subsets. Finally, the semivariogram model γ^* which result in the highest copula density, is chosen to define Γ as

$$\Gamma(h) = 1 - \gamma^*(h, nug, rng) \tag{4.5}$$

where nug is the nugget, rng the range, and h the distance in grid units.

Step 2: Derive the Transformation Function

In the next step, a transformation function that relates the value space of actual rainfall with the standard normal value space is estimated. The forward transformation that relates any rainfall value v^{rain} with its counterpart in standard normal space v^{stdn} is defined as

$$v^{stdn} = \vartheta(v^{rain}) = \begin{cases} \Phi^{-1}((1-p_0)\chi(log(\frac{v^{rain}}{10})) + p_0) & \text{if } v^{rain} > 0 \\ \Phi^{-1}(p_0) & \text{if } v^{rain} = 0 \end{cases} \tag{4.6}$$

where $\chi()$ is the marginal distribution of the rainfall obtained from the distribution of the rainfall observations, $\Phi^{-1}()$ is the inverse standard normal cumulative distribution function and p_0 is the percentage of dry observations. Note that the logarithm function and the factor 10 in Equation 4.6 have only numerical reasons.

The marginal distribution χ is retrieved via a kernel density estimation. For this, only the rain gauge data is used as it can be expected to better represent the true marginal distribution of rainfall compared to the CML data that involves path-averaging. Notably, extreme values of the CML observations could also be considered for the estimation of χ to enable their representation in the fields, if they exceed the extrema of the rain gauge observations.

Step 3: Transform the Rain Gauge Observation to Linear Constraints

The rain gauge observations are not only used to define ϑ but also they are transformed to standard normal space according to Equation 4.6 so that they can be accounted for as linear constraints on the Gaussian fields. However, Equation 4.6 first transforms all zero (dry) observations to the same value in standard normal space. For the conditioning, it is necessary that also the dry observations are spread over the standard normal space. This is achieved via a stochastic (Markov Chain Monte Carlo) subroutine called the Metropolis-Hastings random walk (MHRW), which takes into account the conditional mean and covariances of the observations. Consequently, dry observations that are close to wet observations are transformed to relatively higher values than dry observations which are far from wet ones. Nevertheless, these values all remain below the ones of wet observations, so that they end up to be zero in the final fields (cf. Step 8). Note that the wet observations are transformed in a deterministic way which needs to be done only once. The MHRW applied to the dry observations, however, involves a random distribution which is conducted every time the linear constraints are considered in the algorithm. In the following v_p refers to v_p^{stdn}.

Step 4: Generate Unconditional Fields

In this step, the inner part of RM starts. Unconditional random Gaussian fields $(UF_i)_{i\in[1..K]}$ are generated via inverse fast Fourier transformation considering the estimated covariance matrix Γ and thereby fulfilling the estimated spatial dependence structure. A large pool of such fields is generated at this stage of the algorithm. The exact number of fields K is not critical but should suffice the extent of the given problem and at least exceed the number of rain gauges considered. As a general rule, the more observations the more fields should be created (cf. Section 4.3.4). Albeit, the algorithm includes the possibility to generate fields afterwards, if the initial number was not sufficiently high.

Step 5: Create the Inner Field Representing the Rain Gauge Observations

In the next step the eponymous "mixing" starts. Linear combinations of a subset of the unconditional fields UF_i are calculated considering the linear constraints v_p to generate the *inner field*:

$$IF(x_p) = \sum_{i=1}^{I} \beta_i \, UF_i(x_p) = v_p. \tag{4.7}$$

The weights β_i are required to fulfill

$$\sum_{i=1}^{I} \beta_i^2 < \varepsilon_{IF}. \tag{4.8}$$

In general, ε_{IF} should be as low as possible and needs to be below 1 at least, so that IF has a low variance, which is desirable as it enables to add variability later on. To calculate such an IF, I must be at least as high as the number of linear constraints P. In an iterative manner, I is increased until the conditions are fulfilled.

Step 6: Create Random Noise via a Homogeneous Field

The next step is the generation of a *homogeneous field* (HF). Again, the generation is based on combining a subset of the unconditional fields (UF_i) in linear combinations. Now, in contrast to the previous step, not the linear constraints are respected but the constraint is that at those very locations the result of the linear combination is equal to zero. Formally,

$$HF(x_p) = \sum_{i=1}^{H} \gamma_i \, VF_i(x_p) = 0. \tag{4.9}$$

In Equation 4.9 the VF_i have the same properties as the UF_i, that is, $E(VF_i) = 0$, $var(VF_i) = 1$, and $\Gamma_{VF_i} = \Gamma_{UF_i}$. The different name is introduced only to clarify that not identical fields are used in Equation 4.7 and Equation 4.9. Both IF and HF have an infinite number of solutions once $I > P$ and $H > P$. The weights need to fulfill

$$\sum_{i=1}^{H} \gamma_i^2 = 1 - \sum_{i=1}^{I} \beta_i^2. \tag{4.10}$$

such that the variance of IF and HF add up to 1. Equation 4.9 guarantees that the *homogeneous fields* can be combined with the *inner fields* without corrupting the correct values of the *inner field* at the locations of the rain gauges.

Step 7: Combine the Inner Field and the Homogeneous Field

In this step, the fields constructed in Step 6 and 7 are combined according to Equation 4.4, to generate a *normal field* ($NF = IF + HF$). The definition of the weights in the previous steps guarantees the right spatial dependence structure of this normal field NF, which therefore follows the spatial dependence structure given by the covariance Γ. Moreover, it follows from the construction of IF and HF that NF respects the linear constraints v_p.

Step 8: Back-transform the Normal Field

The pixel values of NF can now be transformed to the value space of actual rainfall by the inverse of Equation 4.6. Formally, the transformation is given by:

$$FF = \begin{cases} \frac{1}{10} \exp\left(\chi^{-1}\left(\frac{\Phi(NF)-p_0}{1-p_0}\right)\right) & \text{if } \Phi(NF) > p_0 \\ 0 & \text{if } \Phi(NF) \leq p_0 \end{cases} \tag{4.11}$$

and provides a *final field* (FF) with actual rainfall values. The conditional definition of Equation 4.11 ensures that the percentage of zero values within FF is similar to that of the observations.

Step 9: Apply the CML Observations as Nonlinear Constraints

This step compares the CML observations w_q with the values of FF. Considering Q CML observations and J pixels along the path of a particular CML, $FF_{q,j}$ represents the values of FF at the pixels along the CMLs. The average along the path $\overline{FF_q}$ can be compared directly to the observed CML values w_q. The fit over all CMLs quantified by the Euclidean distance is defined as

$$\phi(w_q, \overline{FF_q}) = \sum_{q=1}^{Q} (w_q - \overline{FF_q})^2. \tag{4.12}$$

The objective function ϕ is minimized in an iterative manner via creating different homogeneous fields HF, that is, by entering the algorithm at Step 6 repeatedly until

$$\phi(w_q, \overline{FF_q}) < \varepsilon_{CML} \tag{4.13}$$

where ε_{CML} is a predefined threshold. For the optimization, the Whittaker-Shannon algorithm is applied which enables relative fast convergence by selecting appropriate HF (details on this part can be found in Hörning et al. (2019)). Note that additionally a maximum number of iterations of the optimization procedure is defined such that the algorithm terminates even if the threshold is not reached. If Equation 4.13 is fulfilled, HF is a complete reconstruction, then denoted as SF. It represents the rainfall statistics, the rain gauge observations at their locations exactly, and it matches closely with the CML observations.

Step 10: Generate an Ensemble

Finally, it is possible to create an ensemble of solutions. The one SF that has been calculated is not the only solution and other fields can fulfill the necessary conditions, too. Especially at unobserved locations but also along the CMLs' paths, different values are permissible that still are in accordance with the observations and the rainfall statistics. In order to calculate further ensemble members, the algorithm can be entered again at Step 5 by creating a new *inner field IF* and also a new *homogeneous field HF* (Step 6).

Chosen Parameter Values

There are several parameters that govern the RM algorithm and that are adjustable. A selection of crucial parameters and their chosen values is given in Table 4.1. The choice of values was not tested thoroughly, but mostly adopted from the existing RM applications. Only the choice for the nugget is based on a rough sensibility test and the ε_{IF} was increased slightly as a consequence of computational issues, which are discussed in the following section.

Table 4.1: Selection of internal parameters of RM and their chosen values in the applied version.

Meaning	Parameter	Value
Nugget of semivariogram model	nug	0.001
Number of unconditional fields	K	10000
Threshold for variance of inner field	ε_{IF}	0.2
Threshold for CML fitting	ε_{CML}	0.4
Maximum number of iterations for CML fitting	-	300

4.3.4 Technical Challenges and Computational Complexity

Being a stochastic method, RM requires considerable computational resources, which is why this aspect is covered in this separate section. Note that the following refers to the Python implementation RMWSPy (Hörning and Haese, 2021). RM involves the continuous storage of fields (mainly the unconditional fields, UF_i) as they are combined in various linear combinations throughout the algorithm. Hence, there is no easy solution to prevent the occupation of working memory by these fields. Obviously, the issue scales with the problem size, i.e., mainly the considered grid size, which is relatively large in the analyses of this thesis. Similarly, the computation time rises with increasing problem sizes. A detailed analysis of this can be found in Chapter 7.

The RM algorithm, though successfully applied in several smaller scale studies before, was initially (i.e., at the start of the work on this thesis) not capable of dealing with large amounts of rain gauges and CMLs. On the one hand, the computational complexity was very high for the large data sets and a large target grid size; in fact the implementation available in the beginning would have required more than the available resources. However, it was not only an issue of computational resources. Even more crucially, the algorithm did not terminate. More precisely, the computation of the *inner field IF* which requires adjustment to the linear constraints in an optimization loop did not converge.

These issues required adaptations to the code: Primarily, to allow the algorithm to terminate at all for a high number of rain gauges, but also to make large-scale computations feasible on a moderate-sized high performance computer. This was required to allow for an analysis of not only a large grid and a large number of observations, but also over a considerable time span.

Thorough investigations revealed that with regard to the optimization of the *inner field* a major issue were the observations that recorded no rainfall (dry observations). For hourly rainfall estimation, there were, naturally, a large share of dry rain gauge observations. As stated before, dealing with dry observations, i.e., the intermittency of rainfall is a common challenge of rainfall quantification. In the RM algorithm dry rain gauge observations are transformed within the standard normal value space to enable the computation of the *inner field* (see Step 3 of Section 4.3.3.) The MHRW algorithm was improved by a much higher but determined number of iterations and a more suitable decision criterion at each step to raise the quality of the distribution of values. The adjustment of the MHRW implementation enabled the necessary step of calculating the *inner field* that fits to the rain gauge observations.

The computational complexity could then be alleviated by several adaptations: specific Python packages were replaced by more efficient alternatives (e.g., by replacing *NumPy*[2] by *SciPy*[3] functionality in several cases); parallel computing was introduced in the part where the *final field* (FF) is compared to CML data (Step 9 above); the code was refactored as to avoid the superfluous creation of copies of variables. These adaptations made it possible to run the code on the available high-performance computing cluster and to conduct the central case study presented in Chapter 7. Nevertheless, RM is still computationally demanding. Both computation time and working memory requirements are crucial aspects if using large amounts of data or a grid with many cells. Hence, Chapter 7 includes an analysis of computational aspects. Note that the adaptations outlined above were conducted in collaboration and are documented in Hörning and Blettner (2022).

[2] `https://pypi.org/project/numpy/`, last access October 13, 2023
[3] `https://pypi.org/project/scipy/`, last access October 13, 2023

Chapter 5

Methods: Validating Rainfall Estimates

Once rainfall fields are generated the major goal of QPE is accomplished; these fields could be fed into hydrological applications. However, if possible, it is important to assess the quality of the reconstruction to estimate their value for follow-up applications. In fact, it is helpful to assess the quality also at intermediate steps along the rainfall estimation process. In this thesis, validation is done for path-based rainfall estimates of CMLs and for the final spatial reconstructions. Ideally, the estimates (whether they are rainfall amounts along CML paths or rainfall maps) would be compared to the true rainfall, which, however, is generally unknown. Nevertheless, the possibility of quality assessment arises when reference data is available, with which the estimates can be compared, and which can be assumed to represent the truth reasonably well. A standard approach of validation is to calculate performance metrics based on a comparison between the estimations and a reference. The purpose of such metrics is to help interpret the degree of similarity. This is commonly achieved by reducing the dimensionality and by providing a numerical value which is often bound to a certain range or at least has an optimal value. Thereby, the complexity of the comparison is reduced.

This chapter provides the theory and applications of how rainfall estimates are analyzed. First, the validation based on CML path-based rainfall amounts is described in Section 5.1. The main focus, however, lies on rainfall maps and their validation, which is the topic of Section 5.2.

5.1 Path-based Validation

To validate CML rainfall estimates directly requires reference information along the CML paths. Such reference data generally does not exist, however, it is possible to derive path-based values from a gridded reference. In this thesis, path-based reference data is derived from RADOLAN-RW. To achieve this, a weighted mean of the pixel values that have an intersection with a given CML are considered. The weights are proportional to the lengths of the intersection between each pixel and the CML path.

The analysis then consists in a comparison between estimates and reference and the calculation of several performance metrics. The metrics used in this thesis are mean absolute error (MAE), Pearson correlation coefficient (PCC), and bias ($BIAS$), which are calculated for every CML by aggregating over time. Formally, the metrics are defined as

$$MAE_{time} = \mu_{time}(|R_{est} - R_{ref}|), \tag{5.1}$$

$$PCC_{time} = \frac{cov_{time}(R_{est}, R_{ref})}{\sigma(R_{est})\sigma_{time}(R_{ref})}, \tag{5.2}$$

$$BIAS_{time} = \frac{\mu_{time}(R_{est} - R_{ref})}{\mu_{time}(R_{ref})}, \tag{5.3}$$

where R_{est}, R_{ref} is the rainfall amount for all time steps of the estimation and the reference, respectively. The functions $\mu_{time}()$, $cov_{time}()$, $\sigma_{time}()$ (defined in Appendix A) denote the arithmetic mean, the covariance, and the standard deviation over time, respectively.

The mentioned performance metrics all quantify different aspects of the quality of the estimation. The MAE is an accuracy measure that can take values of the range $[0, \infty)$. The closer its value is to zero the better the estimation fits to the reference. The MAE is scale-dependent and preserves the units of the data. The PCC quantifies the degree to which a linear correlation exists between the estimation and the reference. It takes a value of the range $[-1, 1]$ and is not defined if either of R_{est} and R_{ref} has zero variance. For a perfect positive correlation its value is 1, for a perfect negative correlation - 1, and for no correlation it equals 0. In contrast to the MAE, the PCC has no units and is therefore independent of scale. The bias quantifies systematic errors. The above definition allows values in the range $[-1, \infty)$ as rainfall amounts represented by R_{est} and R_{ref} are always positive. The $BIAS$ is not defined if the mean of R_{ref}, and hence all values of R_{ref}, are 0. A negative $BIAS$ reveals underestimation while a positive $BIAS$ shows overestimation. Its optimal value is zero, which represents that there is no systematic error. Like the PCC, the $BIAS$ has no units.

5.2 Spatial Validation

5.2.1 General Aspects of Spatial Validation

The evaluation of the rainfall maps is particularly important as large uncertainties lie in the process of reconstructing described in Chapter 4. Hence, it is extremely valuable to quantify the quality of reconstructions before using them, e.g., in hydrological applications. However, the selection of means to validate, i.e., the selection of performance metrics, is nontrivial as different metrics quantify different aspects.

Two major challenges can be distinguished when trying to evaluate maps. On the one hand, a trustworthy reference is required, and, on the other hand, it is not necessarily clear how to best validate the similarity between reconstruction and reference. Often no spatial reference of sufficient resolution exists and where it exists, it is not free of shortcomings itself. Nevertheless, validation usually needs to make the assumption of the available reference representing the truth. Moreover, in many cases the reference needs to have the same grid dimensions as the reconstruction. Regarding the validation method, a crucial question is: what aspect of the field should be assessed? Not only the reference but also the validation methods, i.e., the performance metrics have their limitations and need to be chosen carefully. As stated above, performance metrics usually provide metrics that reduce dimensionality. That is, rather than considering the differences of two rainfall maps directly, only two scalar values need to be considered which makes the interpretation clearer. However, many performance metrics are available and different metrics can provide quite contrary suggestions about the reached quality.

A common approach of validation is to compare the simulated field with a reference field on a pixel basis. That is, if the fields have the same spatial resolution each pixel is compared to the respective pixel of the reference field. The quality of the whole field can then be described by metrics like the mean error, root-mean-square error, bias, or correlation coefficients, which are metrics that aggregate the information gathered from all pixels into a single value. This provides a straightforward way to assess the likeliness of two fields and is often considered in spatial analyses. However, it has several shortcomings. A common issue is that reconstructions with spatial offsets of objects, such as rainfall cells, may score particularly bad according to those metrics. This effect is known as the double-penalty problem (Ebert, 2008) that can be illustrated by an example: at one location there are high values only in the reference, so that the metrics punish the underestimation; close by, the values are high only in the reconstruction and the metrics punish the overestimation. In fact, however, the reconstruction may be good as it did produce the rainfall object, regardless of the (perhaps small) offset. This effect is amplified for situations with high spatial variability (relative to the grid resolution) as often encountered in rainfall fields. That is, convective rainfall, for example, may affect only a few grid cells. If the rainfall occurrence is displaced even only by a few grid cells the double penalty issue is fully effective as it is possible that no wet grid cell of the reconstruction coincides with a wet grid cell of the reference. The metrics are then often better if the reconstruction is rather smooth but does not represent the spatial correlation, just because this reduces the double-penalty problem. However, the spatial correlation is a crucial aspect and a reconstruction should be rewarded for representing this correctly.

In the attempt to overcome such issues, many other methods have been developed. Gilleland et al. (2009) distinguishes four groups of spatial verification methods that go beyond the pixel-by-pixel comparison. Those are a) neighborhood / fuzzy methods which consider neighborhoods of connected pixels instead of the pixels individually, b) scale-separation methods which consider different spatial scales for validation whereas these scales are often adjusted to physical patterns such as convective cells, c) feature-based / object-based methods that distinguish and compare objects which are constituted of connected pixels, and d) field deformation methods which analyze what spatial deformation would be required to approximate the reconstruction to the reference considering the whole field at once.

In this thesis, emphasis is put on a validation approach belonging to the class of object-based methods. It distinguishes rainfall cells as connected pixels on the grid and treats them as separate objects with specific characteristics. The applied method which calculates a structure, an amplitude, and a location error (SAL) was proposed by Wernli et al. (2008) and later extended by Radanovics et al. (2018). The method is described in detail in Section 5.2.3. Before, standard pixel-based metrics, which are also applied in this thesis, are introduced in the following.

5.2.2 Pixel-based Comparison

For pixel-based validation, three common metrics are applied in this thesis. These are the root-mean-square error (*RMSE*), the Pearson correlation coefficient (*PCC*), and the bias (*BIAS*). Note that the *PCC* and the *BIAS* have already been defined in Section 5.1 where the metrics were calculated for every CML by aggregating over the dimension of time. Here, on the contrary, the metrics are calculated for every time step by aggregating over the spatial dimension. The difference is denoted via the use of the suffixes *time* and *space*. In the chapters presenting the results, the suffixes are generally omitted as it is clear from the context which of the two set of metrics is applied, that is, the path-based analysis is only considered in Chapter 6 while the spatial analysis is only considered in Chapter 7. The spatial pixel-based performance metrics are defined by

$$RMSE_{space} = \sqrt{\mu_{space}((R_{rec} - R_{ref})^2)} \tag{5.4}$$

$$PCC_{space} = \frac{cov_{space}(R_{rec}, R_{ref})}{\sigma_{space}(R_{rec}) * \sigma_{space}(R_{ref})} \quad (5.5)$$

$$BIAS_{space} = \frac{\mu_{space}(R_{rec} - R_{ref})}{\mu_{space}(R_{ref})} \quad (5.6)$$

where R_{rec}, R_{ref} is the rainfall amount for all pixels of the reconstruction and the reference, respectively. The functions $\mu_{space}()$, $cov_{space}()$, and $\sigma_{space}()$ (defined in Appendix A) are the arithmetic mean, the covariance, and the standard deviation, respectively.

A general description of the metrics MAE, PCC, and $BIAS$ has been given in Section 5.1. For the spatial validation, the *RMSE* is used instead of the similar MAE. They are both measures of accuracy, but with the main difference that *RMSE* is more sensitive to outliers.

5.2.3 Pattern Analysis via (e)SAL

A set of spatial performance metrics called SAL was first introduced by Wernli et al. (2008). The three components that are abbreviated by the letters S, A, and L are structure error, amplitude error, and location error. In this thesis, also the performance metrics $eSAL$ are applied. These metrics constitute an extension to SAL introduced by Radanovics et al. (2018). The novelty of eSAL is its possibility to calculate the error metrics for ensembles. Whenever the term (e)SAL is used in the following, this relates to both methods and there is no need to discriminate between the two.

The validation via (e)SAL has been developed specifically for rainfall field validation. Obviously it is not limited to this application, but fits it very well. A central aspect of (e)SAL is its consideration of objects. That is, instead of considering single pixels, the field is divided into objects. These are defined as connected pixels with values above a certain threshold value. Such a separation of objects from their surrounding can usually be done effectively for rainfall which often occurs as separate cells with dry regions in between if the aggregation times are not too long. The (e)SAL methodology is helpful if spatial patterns should be analyzed. The reconstructions by RM (see Section 4.3) are designed to account for the spatial patterns of rainfall. Hence, the (e)SAL performance metrics constitute an appropriate method to validate whether the pattern representation was actually achieved by the RM reconstructions.

The three metrics structure, amplitude, and location error are designed to quantify distinct aspects of the fields and the correlation between them is close to zero. The structure error quantifies the disagreement of the shapes of rainfall objects. It is a measure of the relation of the volume and the peak of a rainfall cell. A negative structure error represents the case in which the rainfall objects in the reconstruction are rather narrow with regard to spatial extent or have rather high peaks, i.e., maximum values within the object. The case of a positive structure error signifies rather widespread or not very peaked objects. By definition, the value range for the structure error is $[-2, 2]$. The amplitude error quantifies overall underestimation or overestimation. In fact, it is directly related to the spatial $BIAS$ and does not consider rainfall objects. It is negative if the reconstruction shows less overall rainfall than the reference, and positive if it shows more. Similar to the structure error, also the amplitude error ranges between - 2 and 2. The location error quantifies displacements in space. It consists of two components L_1 and L_2. L_1 does not consider rainfall objects but the centers of mass of the whole fields. L_2 considers the centers of mass of the individual objects. A discrepancy of location causes a location error which is defined such that it can range between 0 and 2.

The extension to SAL introduced by eSAL enables the quantification of ensembles without the ensemble dimension in the resulting metrics. That is, whether a single field is evaluated or an ensemble of many fields, the calculation yields a single value for each of the three SAL parameters. In theory, both reconstruction and reference can be ensembles, however, in this thesis the reference is always a single field.

The aspect of the (e)SAL validation marking the crucial difference to the aforementioned pixel-based metrics is its consideration of objects. Thereby (e)SAL allows for a validation that takes into account a typical property of rainfall which is its occurrence in separate cells. It is thereby also closer related to a visual qualitative validation of the fields, whereas the quantitative metrics enhance comparability. Note, however, that the objects are actually only considered for the calculation of S and L. The parameter A, on the other hand, quantifies the overall domain-wide rainfall independent of the objects. In fact, it is a function of the bias but with a value range that is in accordance with S and L and hence allows useful direct comparison to those two parameters.

5.2.4 Algorithm of the (e)SAL Calculation

Within the scope of this thesis, the computation of (e)SAL parameters has been made available as Python code (Blettner, 2022). This section describes the implementation which is adopted from the original definition of Wernli et al. (2008) and the ensemble-related extensions of Radanovics et al. (2018). In terms of nomenclature, it partly follows the mentioned publications which are not fully consistent among each other. A clarification of the nomenclature and its usage in the studies is provided in Table 5.1.

Calculating the (e)SAL parameters involves calculating properties of reconstructed and reference fields, and of rainfall objects within these fields. Fields, in this sense, can refer to the reconstruction or the reference, and, if an ensemble is involved, the term refers to an individual ensemble member. That is, in the case of ensembles, first the properties are calculated for each member and afterwards they are combined to describe the whole ensemble. Before calculating the field-specific parameters, the way by which to distinguish objects and

Table 5.1: Nomenclature of parameters used for (e)SAL calculation (cf. Figure 5.1).

Meaning	Parameter
Rainfall threshold	R^*
Threshold factor	f
95th percentile of rainfall	R^{95}
Maximum domain distance	d
Average rainfall of field	D_f
Center of mass of field	$\boldsymbol{x_f}$
Center of mass of object	$\boldsymbol{x_o}$
Maximum rainfall of object	R_o^{max}
Rainfall sum of object	R_o^{sum}
Scaled volume of field	V_f
Scaled distance	r_f
Number of objects in field	O
Number of ensemble members	M

the maximum distance on the grid need to be defined. Figure 5.1 visualizes the procedure and gives an overview of the calculated parameters.

Preparation

The first step is to define a threshold that defines how to distinguish the rainfall objects. It marks the boundary between rainfall amounts that are high enough to be counted to a rainfall object and those amounts that are lower and comprise the areas in between objects. An object is a cluster of connected pixels with values above the threshold. The thresholds (R^*) for the reconstruction and reference are calculated as

$$R^*_{rec} = R^{95}_{rec} \cdot f \tag{5.7}$$

$$R^*_{ref} = R^{95}_{ref} \cdot f \tag{5.8}$$

where the threshold factor f is defined as

$$f = max\left(\frac{1}{15}, \frac{0.1mm}{R^{95}_{ref}}\right) \tag{5.9}$$

and R^{95}_{rec}, and R^{95}_{ref} are the 95th percentile rainfall amount of reconstruction and reference, respectively. In the case of the reconstruction or the reference being an ensemble, R^{95}_{rec} or R^{95}_{ref} take into account all the ensemble members. While the thresholds for reconstruction and reference are different from one another, the threshold factor (Equation 5.9) depends always only on R^{95}_{ref}. That is, the threshold factor is $\frac{1}{15}$ except for situations where this would lead to a threshold below the precision limit of the reference. It depends only on the reference rainfall amount, as no precision limit is given in the reconstructions. The value $\frac{1}{15}$ was introduced by Wernli et al. (2008) without objective reasoning. More details

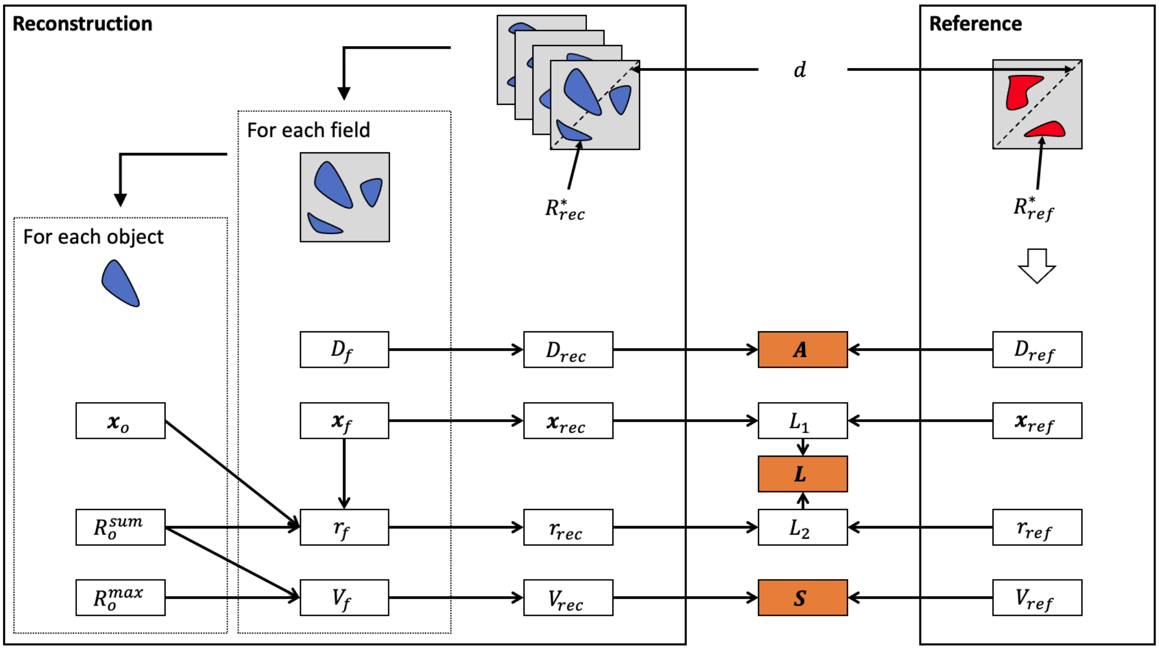

Figure 5.1: Illustration of the (e)SAL calculation. The connection between the parameters that are calculated for individual objects, fields, and full ensembles are shown. The principle remains the same also if no ensemble is considered. The detailed parameter connections are only shown for the reconstruction. For the reference, the procedure is the same. Further explanation can be found in the text and in Table 5.1.

related to the calculation of the thresholds can be found in Radanovics et al. (2018) who also conducted a sensitivity analysis to assess the appropriate definitions. Importantly, the above definition implies that the threshold, which defines objects, can differ between the reconstruction and the reference. This guarantees that the SAL metrics are largely independent from one another as the object classification is not influenced by a potential overall bias.

For the calculation of the L parameter of (e)SAL, the maximum distance d within the domain is required. This is considered to be the length of a diagonal of the rectangular grid. Note that this definition differs from the one of Radanovics et al. (2018) who consider d to be equal to the longer of the two grid axes. The definition chosen here, guarantees that both L_1 and L_2 are within the interval $[0, 1]$ such that L is in the interval $[0, 2]$.

Field-specific Properties

With the threshold values and the maximum distance defined, the field-specific properties can be calculated. They depend on the object-specific properties and can be aggregated to ensemble-specific properties if applicable. Both in Figure 5.1 and in the following part of the text the procedure is described for the reconstruction. A similar procedure is done for the reference but not explicitly outlined to avoid redundancy.

First, for each field the *total center of mass* ($\boldsymbol{x_f}$) is calculated. This defines the location of the center of gravity when virtually converting rainfall amounts to mass. It considers all pixels directly, regardless of whether they belong to objects. Moreover, the average rainfall D_f is calculated as the arithmetic mean of all pixel values.

Subsequently, the rainfall objects are defined via image processing. Connected pixels with values above the threshold R^*_{rec} are identified and each such set of pixels is considered an independent object. Then, the following parameters of the individual objects are calculated: the *local center of mass* $\boldsymbol{x_o}$, the maximum rainfall amount R_o^{max}, and the rainfall sum R_o^{sum}.

With these object-specific parameters the following quantities concerning the whole field are calculated. The normalized volume V_f is defined via the rainfall sum of the objects normalized by the maximum rainfall amount of that object and the overall rainfall sum of all objects, formally

$$V_f = \frac{\sum\limits_{o=1}^{O} R_o^{sum} \frac{R_o^{sum}}{R_o^{max}}}{\sum\limits_{o=1}^{O} R_o^{sum}} \tag{5.10}$$

where O is the number of objects within the field. Moreover, the distances between the objects' specific local centers of mass ($\boldsymbol{x_o}$) to the total center of mass of the field ($\boldsymbol{x_f}$) are calculated. This is normalized by the domain sum of rainfall amount to yield the weighted averaged distance, formally

$$r_f = \frac{\sum\limits_{o=1}^{O} R_o^{sum} |\boldsymbol{x_f} - \boldsymbol{x_o}|}{\sum\limits_{o=1}^{O} R_o^{sum}} \tag{5.11}$$

In the case of ensembles, the above field-specific parameters are calculated for each member that is part of the ensemble. The corresponding parameters (V, D, $\boldsymbol{x}$, and r) that represent the whole ensemble are then derived straightforwardly. V, D, and $\boldsymbol{x}$ are obtained simply via averaging over the ensemble dimension of V_f, D_f, and $\boldsymbol{x_f}$, respectively. That is,

$$V = \frac{1}{M}\sum_{f=1}^{M} V_f, \quad D = \frac{1}{M}\sum_{f=1}^{M} D_f, \quad \text{and} \quad \boldsymbol{x} = \frac{1}{M}\sum_{f=1}^{M} \boldsymbol{x_f} \tag{5.12}$$

where M is the number of ensemble members. For r, in contrast, the set containing all r_f is considered, that is,

$$r = (r_f)_{f \in [1..M]}. \tag{5.13}$$

Note that no special treatment for non-ensembles ($M = 1$) is required: in this case, V, D, and $\boldsymbol{x}$ are equal to V_f, D_f, $\boldsymbol{x_f}$ following Equation 5.12; and for r, the set simply contains only one element.

The four parameters V, D, $\boldsymbol{x}$, and r are used for the calculation of the (e)SAL error metrics together with the corresponding parameters of the reference that are derived similarly. In the following, the subscript rec or ref is used again to discriminate whether a parameter describes the reconstruction or the reference, respectively.

Actual (e)SAL Metrics

For the calculation of the S parameter, the volume parameters of reconstruction (V_{rec}) and reference (V_{ref}) are required:

$$S = \frac{V_{rec} - V_{ref}}{0.5(V_{rec} + V_{ref})} \tag{5.14}$$

For the calculation of A, none of the object specific parameters is required. A is defined as

$$A = 2 \cdot \frac{D_{rec} - D_{ref}}{D_{rec} + D_{ref}}. \tag{5.15}$$

The L parameter is the sum of the two components L_1 and L_2. L_1 considers the total centers of mass, while L_2 considers the aggregated, weighted distances of the local centers of mass of the individual objects to the total center of mass of the fields. Formally,

$$L = L_1 + L_2 \tag{5.16}$$

with

$$L_1 = \frac{dist(\boldsymbol{x_{rec}}, \boldsymbol{x_{ref}})}{d} \tag{5.17}$$

where $dist()$ is the Euclidean distance function, and

$$L_2 = 2 \cdot crps\left(P\left(\frac{r_{rec}}{d}\right), P\left(\frac{r_{ref}}{d}\right)\right). \tag{5.18}$$

In Equation 5.18 the function $crps()$ (defined in Appendix A) is the continuous ranked probability score, and $P()$ the empirical cumulative distribution function. The function $crps()$ provides a measure of distance between two cumulative distribution functions. In the case in which no ensembles are considered, it is equal to the mean absolute error.

5.2.5 Interpretation of (e)SAL and Pixel-based Performance Metrics

While the calculation of the SAL metrics has been introduced above it may not yet be clear what inferences can be drawn from their values and how they relate to other metrics. Figure 5.2 provides basic constructed examples showing edge cases in each of which only one of the three parameters is affected. This visualizes that the parameters can quantify aspects of the field independent of one another. The reference in Figure 5.2 is always the same (top left). If the reconstruction is the same (Rec 0) all metrics are zero. Rec 1 is a reconstruction which has the same overall amount as the reference (hence, A is zero), however, a different, more peaked and narrow shape. Consequently, the S parameter is negative. For Rec 2, on the other hand, the reconstruction shows a widespread not so peaked rainfall object. Again, the overall amount is similar to the reference, but here, the structure error is positive. Rec 3 and Rec 4 show examples where only the amplitude error changes as there are only differences in the overall amount. The structure error remains at zero in these examples as the relation between maximum values and the volume remains constant. The last example (Rec 5) shows a displacement of the rainfall object. The total amount and the shape of the objects are similar. The different location leads to a nonzero location error. The error is rather small, however, because only the component L_1 deviates from zero whereas L_2 is always zero if only a single object exists.

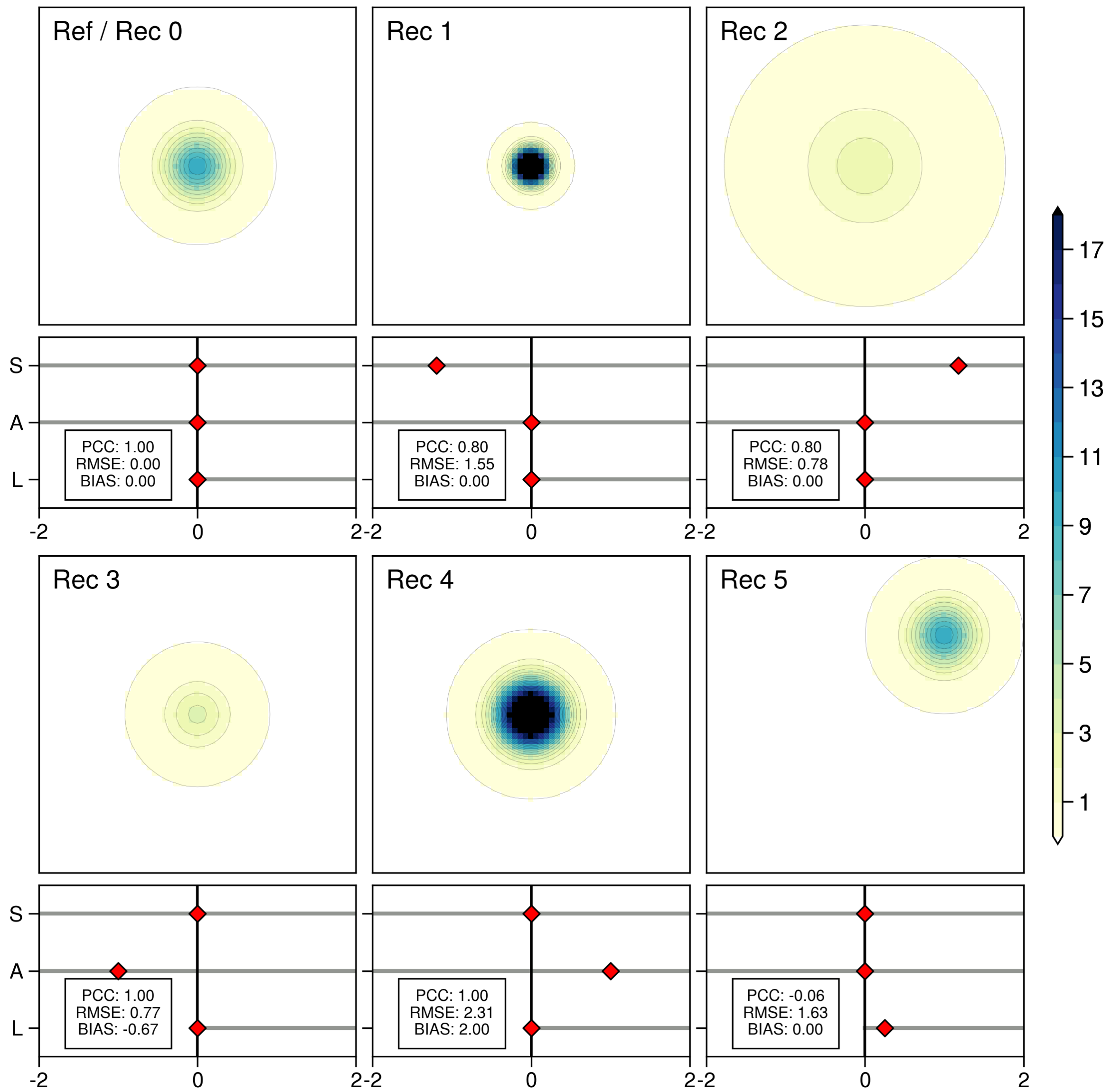

Figure 5.2: Illustration of SAL metrics via constructed exemplary fields. The upper-left field is the reference for all reconstructions (Rec 0 – Rec 5). Below the fields the respective SAL (and standard) metrics are shown. Units of field values are omitted as they are irrelevant for the calculation of the metrics.

Figure 5.2 additionally shows standard metrics $RMSE$, $BIAS$, and PCC as defined in Equations 5.4, 5.5, and 5.6, respectively. The two examples with nonzero structure errors show no bias and a similarly high PCC. The $RMSE$ is nonzero in both of those cases and larger in the case of the narrow peaked reconstruction (Rec 1) as in the case of the widespread smooth reconstruction (Rec 2). This reveals an interesting difference between the quantitative range of the errors: According to S both Rec 1 and Rec 2 resemble Ref equally well, and only differ in their sign; according to $RMSE$, on the other hand, the too widespread object is not as bad as the too narrow one, and according to PCC, Rec 1 is slightly better. With respect to Rec 3 and Rec 4, there is no error according to PCC. $RMSE$ is nonzero but much higher for the case with very high rain rates in the reconstruction (Rec 4). The $BIAS$ always shows the same tendency as A but via a different value range, which is not centered around zero, but within the interval $[-1, \infty)$. The last example of displacement (Rec 5) receives a very poor PCC value, which represents approximately the quality of a random guess. Also the $RMSE$ is considerably high. According to the $BIAS$, on the contrary, Rec 5 represents a perfect fit, i.e., no systematic error exists. This latter example of Rec 5 in particular shows how standard metrics, like PCC and $RMSE$, can be misleading as a result of the double-penalty problem described above.

These constructed cases show clearly how important it is to select suitable parameters for validation. It is necessary to decide on the aspects of the reconstruction that are most relevant in a particular case of application. Note that these examples show only single rainfall objects. (e)SAL is of course not restricted to such simple cases and many objects may be present and their number may be different in reference and reconstruction. In Chapter 7 the (e)SAL validation is applied to real scenarios.

Chapter 6

Results: Transboundary Rainfall Reconstruction

This chapter presents the results of the case study on generating transboundary CML-based rainfall maps. The main research question being addressed in this chapter is: Can two large independent CML data sets be combined and processed jointly to generate consistent transboundary rainfall maps? While data and methods have been introduced in Chapters 2–5, this chapter starts with Section 6.1 describing the specific data and methods used only in this case study. Subsequently, the results are presented in Section 6.2.

6.1 Case-related Data and Methods

The case study presented in this chapter uses the CML data from both Germany and the Czech Republic and focuses on transferability of CML processing algorithms. Hence, several new methodological aspects of this processing are introduced here. An overview of the setting of the case study is given in Figure 6.1.

This case study covers a one-month period (June 2021) and focuses on the border region between Germany and the Czech Republic. The two respective CML data sets are described in detail in Section 2.2. Overall data from approximately 3900 and 2900 CMLs are available from Germany and the Czech Republic, respectively. In the analyses of this chapter, 1167 (Germany) and 2244 (Czech Republic) CMLs are considered, which are located in the border region as defined in Figure 6.2.

In the context of this case study, it is important to note that the two used CML data sets vary significantly with respect to spatial distribution, frequencies and lengths. The Czech data set has a significantly higher CML density in populated regions (e.g., the city of Prague), whereas in Germany the CMLs are more evenly distributed across the country. In Germany, CML frequencies essentially vary between 12 and 39 GHz while in the Czech

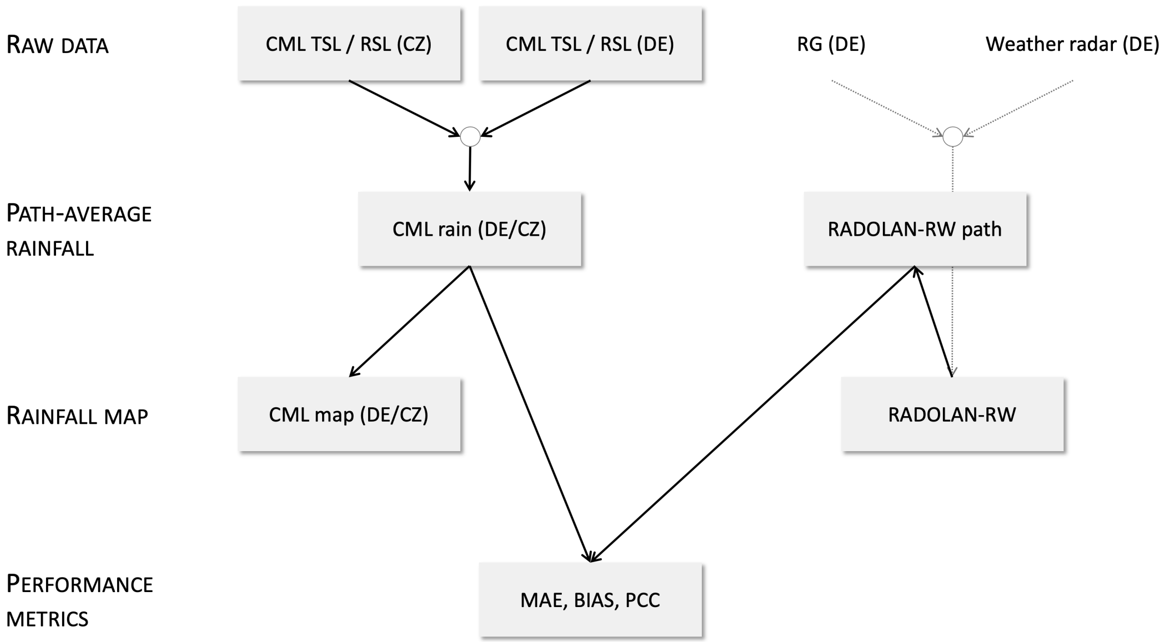

Figure 6.1: Overview of the design of the first case study with the focus on transboundary rainfall maps. Two CML data sets from Germany (DE) and the Czech Republic (CZ) and the rain gauge-adjusted radar product RADOLAN-RW are used. The CML data is combined and processed to obtain path-averaged rainfall information. The path-averaged rainfall information of the CMLs is used to generate transboundary maps, and compared to path-averaged rainfall information derived from RADOLAN-RW to calculate the performance metrics MAE, $BIAS$, PCC.

Republic the data set comprises approximately 30% E-band CMLs with frequencies above 70 GHz. The CML length in Germany is above 1 km in 99% of the cases. In the Czech Republic, 26% of CMLs have a length below 1 km and 1% even below 0.1 km.

These differences have a strong effect on the sensitivity of the path attenuation on rainfall, that is, on the CML's detection limit DL, a parameter used throughout this case study. It is defined as

$$DL = \frac{A_q}{G \cdot a(freq, pol)} \tag{6.1}$$

where A_q is the quantization which is assumed to be at 0.33 dB for all CMLs. The parameter G represents the CML length and a is the factor of the k-R relation (Equation 2.2) which is dependent on the frequency ($freq$) and polarization (pol), and is obtained from the ITU recommendations (ITU-R, 2005). By this definition, the detection limit quantifies the minimum rain rate that is required to induce an observable difference in the signal. Also, it roughly determines the precision of the retrieved rain rate. The detection limit is dependent on frequency and length which have a wider range of values in the Czech data, and hence, also the range of detection limits is larger in the Czech data. The Czech CMLs have detection limits from 0.04 to 132 mm/h, whereas the detection limit of the German data lies mostly between 0.2 and 1 mm/h, and only two German CMLs exceed a detection limit of 2 mm/h. Note that a crucial difference in this regard is the presence (for the Czech Republic) and absence (for Germany) of E-band CMLs which are generally rather sensitive to rainfall. The E-band CMLs that are longer than a few kilometers have an exceptionally low detection limit below 0.1 mm/h. This property is beneficial for sensing light rainfall but these highly sensitive CMLs are also more prone to experience very high attenuation. Strong rainfall can therefore even lead to a loss of connectivity along the CML as the receiver fails to record below a certain level (see Polz et al. (2023) and the description of blackout gaps in Section 6.2.2).

As a reference, the gridded rain gauge-adjusted weather radar product RADOLAN-RW is used and described in Section 2.1. Despite the fact that two countries are considered in this case study, RADOLAN-RW serves as the only reference. This is done to avoid additional potential error sources stemming from combining independent reference data sets. Unfortunately, there is no gridded data set of comparable resolution and quality available that covers both Germany and the Czech Republic completely. Nevertheless, the border region considered in this case study is covered by RADOLAN-RW to a large extent (see Figure 6.2), and hence RADOLAN-RW can be considered a suitable reference.

In this case study, the estimated rainfall maps are compared to RADOLAN-RW directly (Section 6.2.5), but also, rainfall retrieval based on the CML paths is evaluated (Section 6.2.4). For the path-based evaluation, reference values along the paths need to be derived. Therefore, a weighted sum of the RADOLAN-RW pixel values along the path of every CML is computed. The weights are proportional to the length of the intersection of pixels and CML paths (cf. Figure 4.1 where the weight of pixel x_{33} would be larger than that of pixel x_{23}, for instance).

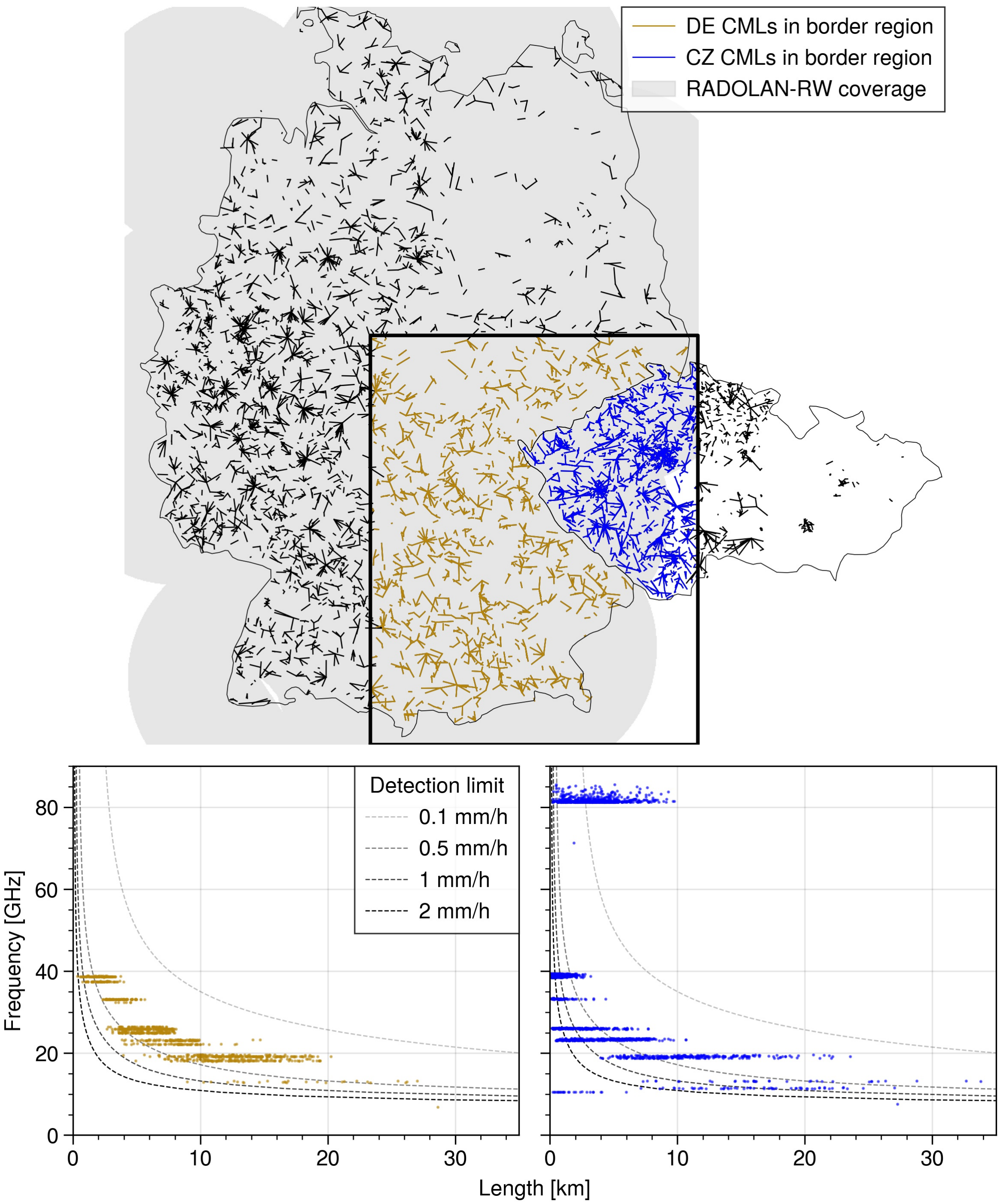

Figure 6.2: Data overview. Top: Sensor locations with the analyzed border region defined by the black box; the shaded background shows the coverage of RADOLAN-RW. Bottom: Distribution of frequency versus length of CMLs within the analyzed region (German and Czech CMLs in left and right panel, respectively); dashed lines show levels of detection limit.

The CML processing algorithms are primarily based on those applied in Graf et al. (2020), which originally were adjusted to a purely German CML data set and a different period than considered in this case study. The processing can be subdivided into two aspects: a) dealing with erroneous data, that is, quality control (QC), which is particularly relevant for opportunistic data with its potentially high number of error sources associated with engineering details rather than atmospheric aspects; and b) rain rate retrieval and mapping which involve steps that are related to well-understood challenges but nonetheless are associated with considerable uncertainties. The difference between the German and Czech CML data sets required some adaptations and extensions to the QC part of the established algorithms.

The results involve an investigation of data quality issues, QC algorithms that are adapted to the observed patterns, and their effects in Sections 6.2.1–6.2.3. In Section 6.2.4, the quality of path-averaged CML rainfall amounts on an hourly basis is quantified in a comparison to RADOLAN-RW along the paths using the performance metrics MAE, PCC, and $BIAS$ as defined in Section 5.1. Finally, in Section 6.2.5, the rainfall maps are evaluated qualitatively.

6.2 Results of the Case Study

6.2.1 Identifying Issues of Data Quality

Investigating the data sets reveals the necessity for quality control algorithms. Before describing the individual algorithms conducted in this regard, the main observations that justify them are summarized. The justification is largely based on the physical limits of rainfall, its statistics and the knowledge of how rainfall can and cannot be reflected in CML observations. For most described patterns, an example is given in Figure 6.3.

Anomalous data points and periods are observed in several CMLs. For instance, a limited number of unreasonably low or high values leads to spikes in the time series. Moreover, the time series of some Czech CMLs show periods in which the baseline of received signal levels (RSL) drops to values far below the median and then stays at approximately (but not exactly) this level for several minutes, hours or even days before it leaps up again. These patterns are referred to as *plateaus*. Furthermore, gaps in the time series of the RSL are encountered at presumably rainy periods, when the signal before or after the gap is significantly lower than the median of the whole time series. Those gaps are considered *blackouts*, that is, they are gaps caused by a failure of the receiver to process RSL values below a certain threshold in the case of heavy rainfall (Polz et al., 2023). Moreover, short gaps in the time series can be observed, due to outages in the acquisition or other technical aspects. These are not considered blackouts if the RSL is not particularly low before or after the gaps.

In addition to the period-based observations, there are issues that affect CMLs as a whole. Most prominently, several CMLs show high fluctuations throughout the raw signal time series. These fluctuations may occur in daily or random patterns and are often clearly stronger and affect more time steps than the fluctuations induced by rainfall. Moreover, the Czech data includes CMLs with very high detection limits. These CMLs are, by definition, not capable of measuring weak rainfall. Furthermore, they are less precise even if the rainfall exceeds the detection limit. The quantization of the recorded signal only allows a coarse estimation in these cases.

The above mentioned observations led to the definition of the following steps that are applied to improve data quality. Of those, the first four affect only single data points of the time series, while the latter two affect CMLs as a whole.

6.2.2 Adapted Quality Control Algorithms

Step 1: Removing Specific Fill Values

Missing values are often given as numerical *fill* values, for which there is not a strict convention. Signal levels are set to missing values if they have any of the following values: - 99.9, - 99, 255, or approximately 1e37. Of course, other fill values might occur in other data sets. Nevertheless, this step is defined in a specific way as each fill value might have a different unknown reason and meaning, which makes it useful to identify them and to address them directly.

Step 2: Filtering Plateaus

The *plateau filter* applies to data points that fulfill both of the following conditions: a) the centered rolling maximum RSL of three data points is below - 85 dB, and b) the centered rolling standard deviation of RSL of three data points is smaller than 0.5 dB. Additionally, data points that are adjacent (next and second to next) to such plateaus are filtered. The threshold of - 85 dB was chosen as the distribution of RSL exhibits a peak for lower values, which is not explicable by rainfall induced attenuation.

Step 3: Filling Blackout Gaps

Following the approach of Polz et al. (2023), a period of missing values is considered to be a blackout gap if the last RSL value before the gap or the first value after the gap is below - 65 dB. In this step, these gaps are filled by the lowest RSL recorded by the CML over the whole month. Note that the maximum period that can be filled does not exceed 1 h, that is, at maximum 0.5 h after a gap starts and 0.5 h before the end of a gap. The gap is not filled at all if its length exceeds 1 h. Note that periods that are considered blackout gaps are always classified as being wet in the rain rate retrieval part of the processing.

Step 4: Filling 5-Minute Gaps in the Time Series

The steps above depend on RSL. Step 4, in contrast, is based on the total loss (TL), that is, the difference between transmitted signal level (TSL) and RSL. If there are gaps in the TL time series and if they do not exceed 5 minutes, they are interpolated linearly. If they exceed 5 minutes they remain unaffected by this step.

Step 5: Filter due to Fluctuations in the Time Series

This filter comprises two tests: a) the 5-hour rolling standard deviation of the TL exceeds 2 dB at least 10% of the time; b) the 1-hour rolling standard deviation of the TL exceeds 0.8 dB at least 33% of the time. All CMLs that fulfill at least one of these conditions are removed in this step. Note that this step and the previous Step 4 are similar to what was already done by Graf et al. (2020); however, they are specified here to explicitly state the full QC sequence.

Step 6: Filter by Detection Limit

The detection limit is defined as the minimum rainfall required to induce an observable change in the signal of a CML. It is calculated via Equation 6.1. Step 6 removes CMLs with a detection limit of at least 2 mm/h. This threshold was chosen heuristically but based on the fact that a large proportion of the rainfall amount in the Central European climate can be attributed to rain rates below this value. Hence, CMLs that cannot sense such low intensity rainfall are neglected.

Application of the Algorithms

For the following part of the analyses, three processing lines are distinguished, which differ in the selection of the steps defined in this section. These processing lines are referred to by the terms *No Filter*, *Graf 2020*, and *Full*. In the *No Filter* case, only the basic Step 1 is performed. In the *Graf 2020* case, additionally Steps 4 and 5 are performed. These steps have been adopted from Graf et al. (2020), and hence, this processing line represents a current standard approach of dealing with data quality adjusted to a purely German data set. In the processing line *Full*, all steps defined in Section 6.2.2 are performed. The steps are always conducted in the order used above. The effect of the different processing lines is considered in Sections 6.2.4 and 6.2.5. In Section 6.2.3, on the contrary, the individual steps of the *Full* processing line are considered and their effects are analyzed separately.

6.2.3 Effect of Quality Control Algorithms

Figure 6.3 showcases the effect of steps introduced in Section 6.2.2 via exemplary time series. The first example shows that there would be extremely high hourly rainfall amounts towards the end of the shown period, if the *plateau filter* was not active. The second example shows how *blackout gap filling* can help to capture a rain event that otherwise would have been missed. In the third example, a strongly fluctuating CML yields rain events far too often and without correlation to the reference. The fourth example presents a CML with a high detection limit; although it captures most of the rain events, the amount is generally far too high and even minor changes in RSL suggest strong rain. In the latter two examples, the respective CMLs are removed completely from the analysis when considering the *Full* processing line.

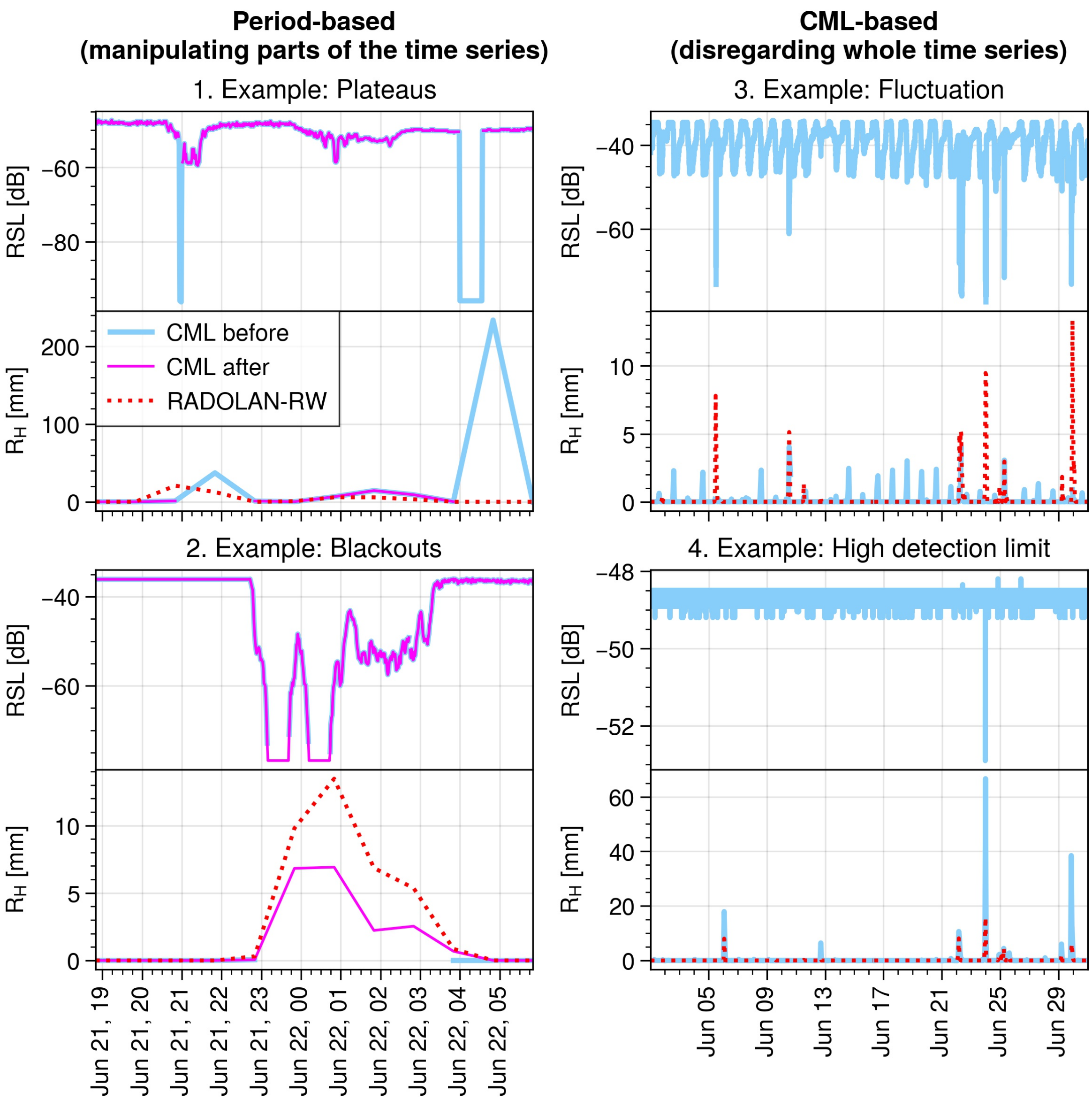

Figure 6.3: Examples of data quality issues and QC algorithms. Four exemplary time series are shown of which each has been treated by one of the steps of Section 6.2.2. The left column treats period-based steps, and the right column steps that affect CMLs as a whole. For each example, the received signal level (RSL) and hourly rainfall sums (R_H) are shown.

Figure 6.4 provides statistics about the amount of data that is influenced by steps of QC. It shows that only a small amount of data is affected by the *plateau filter* and the *blackout gap filling*. Affected hours are defined as hours in which at least 10 minutes are labeled either as a *plateau* or as a *blackout gap*. Only for the class of data points that are associated with high reference rainfall amounts and either very low or very high detection limits, the *plateau filter* affects a larger share. For the *blackout gap filling*, there is a clear positive correlation between the amount of affected hours and reference rainfall amounts. Moreover, CMLs with lower detection limit are affected more often. Similarly, mostly the CMLs with low detection limits are affected by high *fluctuation*. By definition, the filter based on the detection limit affects only the class with the highest detection limit. The effect of filtering CMLs on the spatial sensor density can be seen in Figure B.1 in the Appendix.

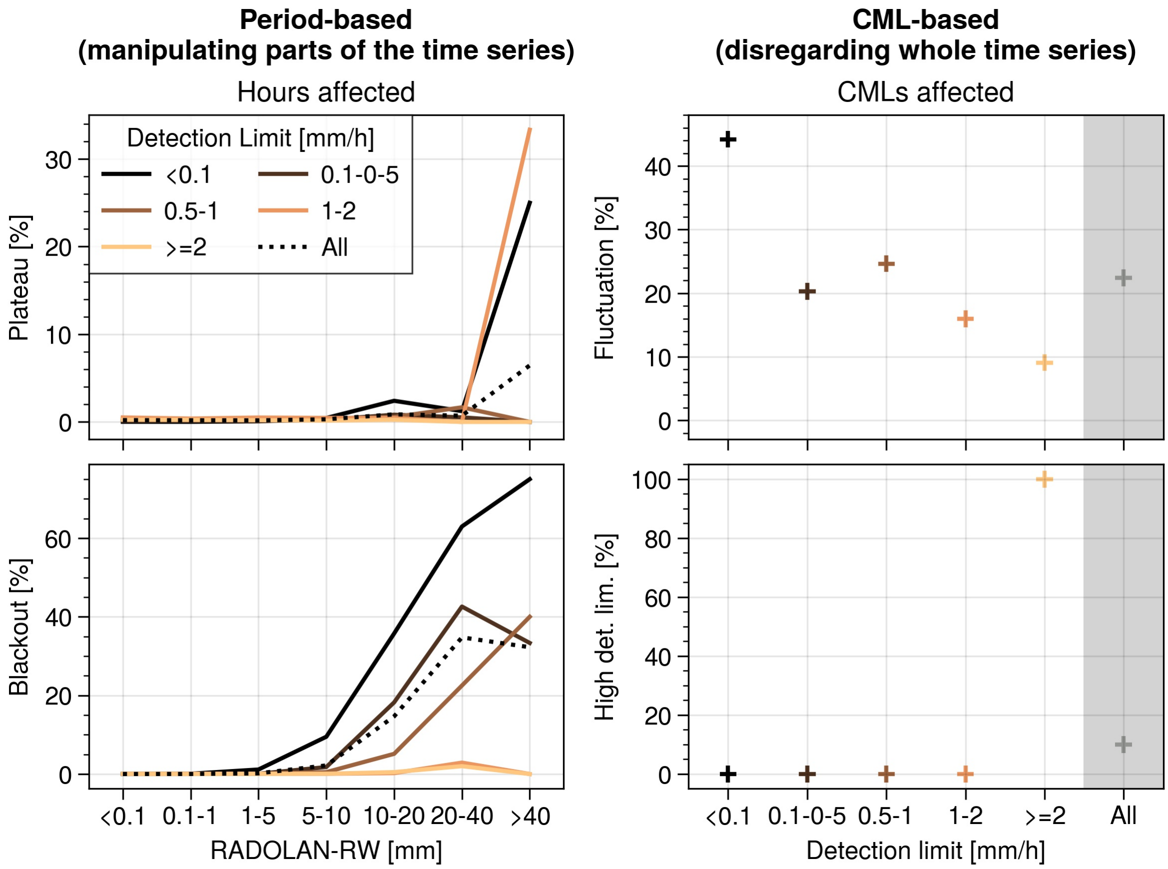

Figure 6.4: Effects of QC algorithms shown via statistics about the abundance of occurrences of data quality issues. The left column treats period-based steps, and the right column steps that affect CMLs as a whole (cf. Figure 6.3). In the left column affected means that at least 10 minutes per hour are either filtered (*plateau filter*) or filled (*blackout gap filling*). In the right column, the percentage of CMLs affected by either fluctuation or high detection limit is shown. Note that this analysis relates to the processing line *Full* in which all the steps of QC are conducted.

6.2.4 Path-based Quantitative Analysis

Path-averaged rainfall amounts of the CMLs in the border region for one month are evaluated by comparison to RADOLAN-RW along the CML paths and by analyzing the performance metrics. Figure 6.5 shows CML quantities and the performance metrics dependent on detection limit, the kind of QC algorithms, and the country. The boxplots indicate the spread over the CML dimension.

The different range of detection limits of the two data sets can be seen in the upper row of Fig 6.5. The filtering involved in the QC algorithm causes a general reduction of the number of CMLs. While this reduction affects the data sets of both countries, it is clearly more pronounced for the Czech data set. Starting from *No Filter* the additional filtering of *Graf 2020* affects CMLs of all classes of detection limits. The additional steps (*Full*) almost only affect the Czech CMLs and primarily the ones of high detection limits.

The values of the performance metrics and their distributions depend on the detection limit. All three metrics deteriorate towards the classes of high detection limits. This can be seen by worse median values, and, in a more pronounced manner, by the worse mean values and the marked skewness of the distributions. A skewed distribution can especially be observed for the detection limit classes > 0.5 mm/h. The *BIAS* additionally shows a general increase with detection limit: While CMLs with very low detection limit (e.g., the ones of E-band frequency) tend to underestimate the rainfall amounts, the ones with high detection limits tend to overestimate. The effect of the detection limit can mainly be seen in the Czech data where each class contains a considerable number of CMLs. For Germany, the effect is less clear due to the small number of CMLs with detection limits above 1 mm/h in the German data set. Nonetheless, outliers in *MAE* and *BIAS* are more prevalent for the detection limit class of 0.5–1 mm/h compared to the class 0.1–0.5 mm/h, also in the German data. Note that for readability not all outliers of *MAE* and *BIAS* are shown in Figure 6.5.

The performance metrics also depend on the three processing lines and the two countries. Considering the effect independent of the detection limit, that is, focusing on the shaded parts of Figure 6.5, a reduction of outliers with extended processing can be observed throughout. While the median of the *MAE* varies only little for the different processing lines, the number of outliers is clearly reduced by the enhanced processing. This can particularly be seen for the Czech data by the improved mean values: for example, the *MAE* of the Czech CMLs has the values 0.19 mm, 0.19 mm, 0.11 mm, for the *No Filter*, the *Graf 2020*, and the *Full* processing lines, respectively (an overview of the metrics is provided in the Appendix in Tables B.1 and B.2). A similar observation can be made for the *BIAS*, where the medians are very close to zero for all processing lines, but where the mean values of *No Filter* (0.46) and *Graf 2020* (0.46) are clearly higher than those of the processing line *Full* (0.02). Independent of the country, the *PCC* improves with increasingly effective processing both in terms of the median (from 0.89 over 0.91 to 0.93 for the German data, and from 0.84 over 0.84 to 0.86 for the Czech data) as well as by a reduction of the number of outliers and increasing mean values.

The effect of the processing lines can also be seen within individual classes of detection limit. Especially for the category of CMLs with detection limits in the range 0.5–1 mm/h, the extended processing affects the mean of *MAE* and *BIAS* strongly, while the effects on the quantiles depicted in the boxplots are small. This shows that the extended processing mainly reduces the number of outliers and thereby their influence on the metrics.

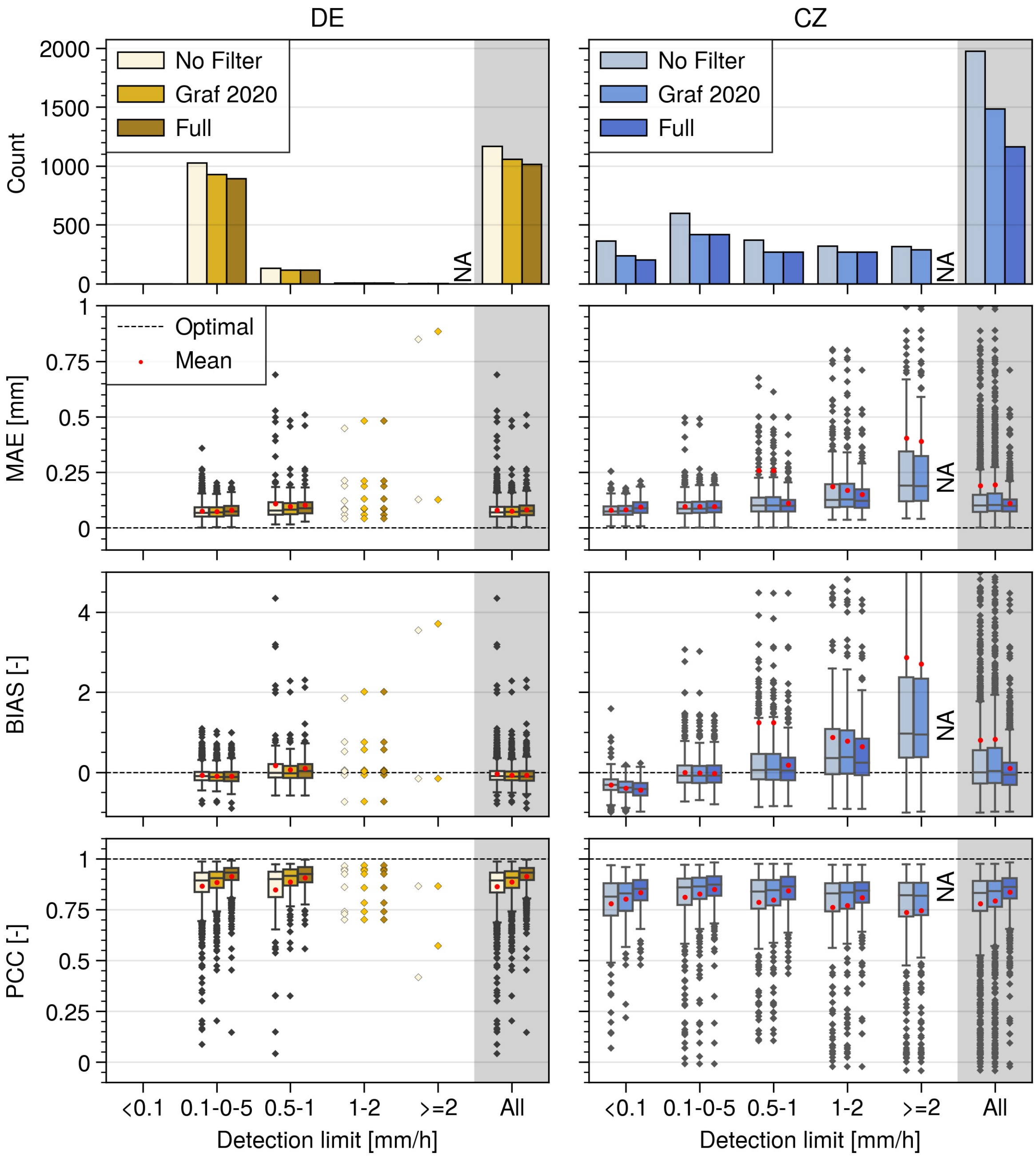

Figure 6.5: A path-based quantitative analysis for the whole month (June 2021). The CMLs are categorized into classes of detection limit and three different processing lines are shown by different color intensities of bars and boxplots. By definition, CMLs are not available (NA) in the *Full* processing for the highest class of detection limits. The first row shows the amount of CMLs in each class. The latter three rows show the mean absolute error (*MAE*), the *BIAS*, and the Pearson correlation coefficient (*PCC*), respectively. The shaded part of the figures considers all CMLs independent of their detection limits. The left and right column consider the German and Czech CMLs, respectively. For Germany, two classes of detection limit contain very few CMLs and for those the metrics are shown as individual points for each CML instead of boxplots. Note that not all data points lie within the presented range of values for the *MAE* and the *BIAS*.

6.2.5 Spatial Rainfall Reconstruction

Figure 6.6 shows rainfall maps for an event (June 21st, 21:50 to June 22nd, 4:50) that traverses the German-Czech border. Via all of the processing lines (first three rows in Figure 6.6) it is possible to generate maps that reproduce the overall pattern of the event. Nevertheless, particularly for the *No Filter* processing line several shortcomings can be observed. For example, there are spots of overestimation. These appear most prominently in the cities and towns in the Czech Republic where the CML networks are dense. (e.g., in Prague located within the red square in the upper left map of Figure 6.6, and Strakonice encapsulated by the orange square in the panel of the last time step). Moreover, there are white spots of underestimation within the rainfall field, particularly, at the time stamp 01:50 (highlighted by a purple square). Furthermore, for the first two time steps in which the rainfall is mostly located over Germany (region highlighted by magenta square), the high spatial variability as well as the high amounts observable in the reference is only weakly represented in the CML-derived maps.

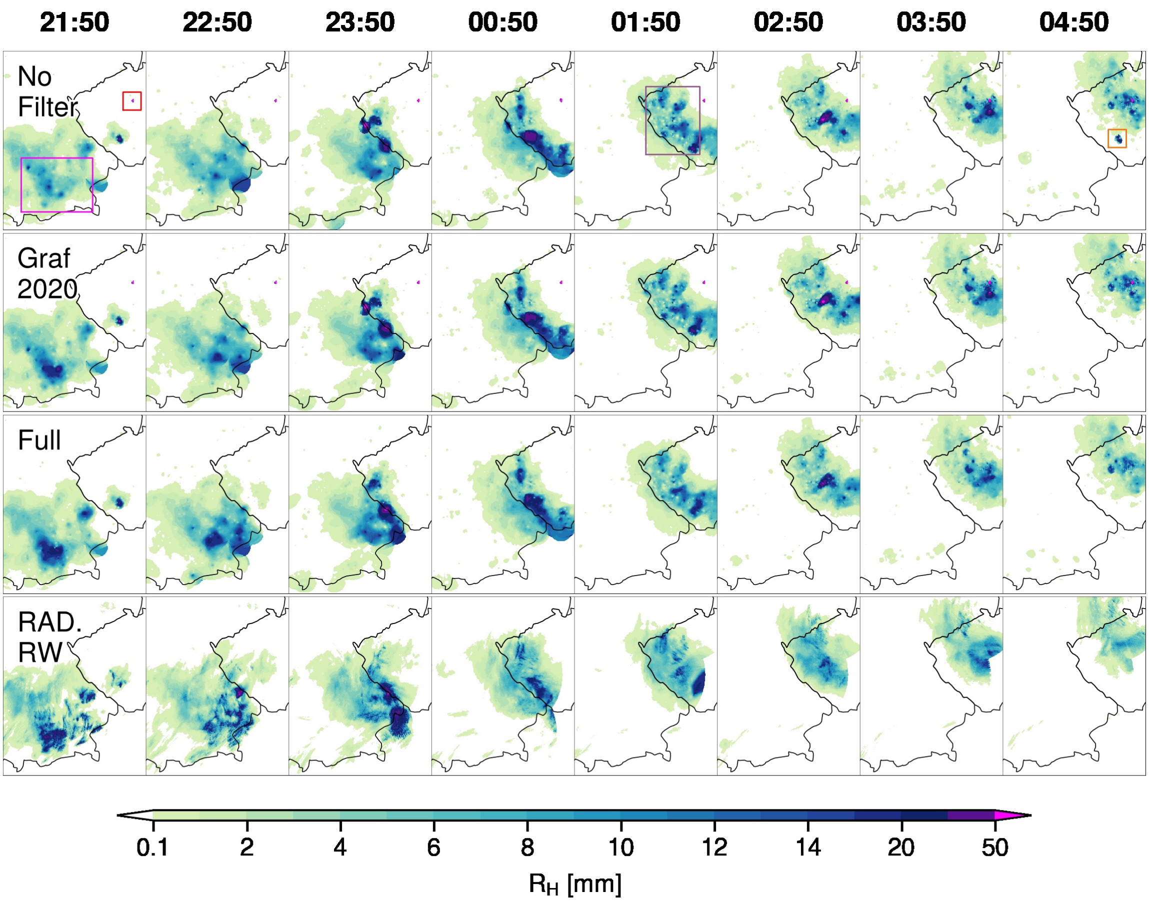

Figure 6.6: Maps of a rainfall event (June 21st, 21:50 to June 22nd, 4:50) (time progressing from left to right). The first three rows are interpolations based on CMLs for the different processing lines. The bottom row is the reference RADOLAN-RW. A comparison of the *Full* processing and RADOLAN-RW in a movie sequence can be found in Blettner (2023). Another event is shown in Figure B.2 in the Appendix.

Positive effects of extended QC algorithms can be observed by comparing the different processing lines in Figure 6.6. The spots of overestimation in the Prague region are present in all time steps for the *No Filter* case, and also in the *Graf 2020* case, but not anymore when applying the *Full* processing. The local false rainfall in Strakonice is already removed via the *Graf 2020* processing. The extended processing also helps to reduce some white spots that appear while the rain event is located over the westernmost part of the Czech Republic (e.g., time step 01:50), though several of these spots persist. The underestimation in the time steps 21:50 and 22:50 is reduced from the *No Filter* to the *Full* processing lines, even though the representation of the spatial variability remains limited.

While hourly rainfall sums are depicted in Figure 6.6, their sums over the whole analyzed month are presented in Figure 6.7. For the processing lines *No Filter* and *Graf 2020*, areas of very strong rainfall can be observed within the Czech Republic and along the border. Similarly high values cannot be found in the reference, and their occurrence can clearly be attributed to individual outliers in the observations that have a strong influence on their surrounding in the IDW interpolation. While only minor effects can be seen by the processing of *Graf 2020*, the extreme overestimations are strongly reduced considering the *Full* processing line. The map of the *Full* processing line is roughly comparable to the reference: Whereas finer structures cannot be captured in the monthly sum (which is partly explicable by the application of the simple IDW interpolation) the broader areas of high and low rainfall sums coincide, and also the total amounts are in the same order of magnitude.

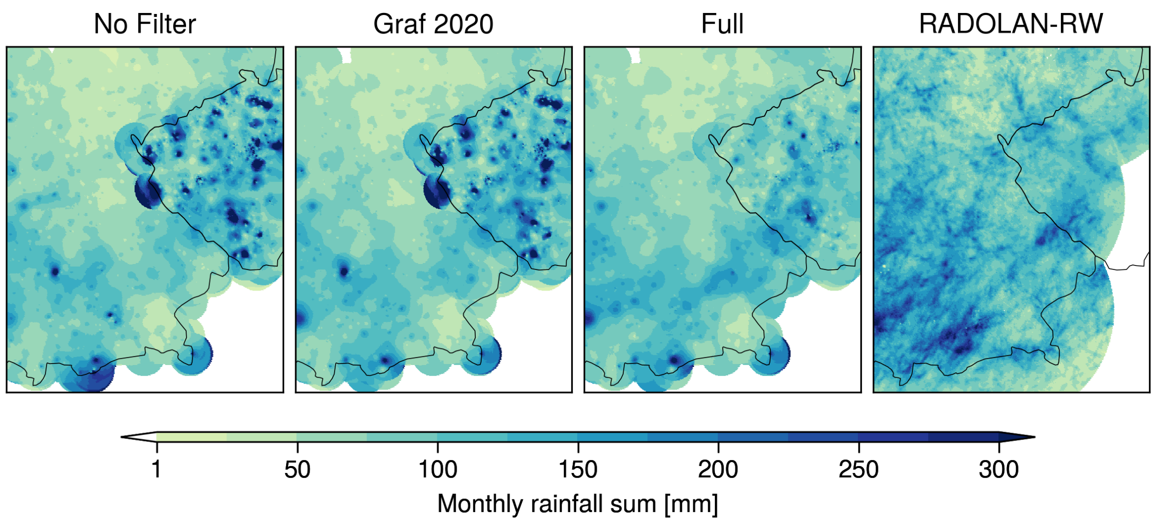

Figure 6.7: Maps of the monthly rainfall sum for June 2021. From left, the first three maps are interpolations based on CMLs for the different processing lines. The map on the right is the reference RADOLAN-RW.

6.3 Summary and Discussion

It was found that two individual CML data sets can be processed consistently with acceptable results even when applying algorithms that had been adjusted to only one of them and for a different period. However, while this holds for many CMLs and over most periods, it produces unrealistic rainfall amounts in some situations, which, despite their rarity can have strong influence on the maps.

Thereby, this case study confirmed that it is crucial to deal with quality control (QC) when using CML data for rainfall estimation. Not only the frequency and the length distributions that determine the detection limit of the CMLs, but also unreliable periods or gaps in the time series of individual CMLs need to be considered. Some issues such as blackout gaps and CMLs with high fluctuations in the signal exist in both data sets. Others, like the periods that are referred to as *plateaus* are essentially only observable in the Czech data set. Global processing algorithms are required that address the individual characteristics but still allow for a consistent treatment of all available data. The need to extend the set of algorithms developed for one data set when applied to a different independent data set, shows precisely the degree to which established routines are transferable, and where they are insufficient.

QC algorithms, which were partly adopted from Graf et al. (2020) and partly developed in this case study, were applied and analyzed. These algorithms involve filtering, that is, a reduction of the amount of data, which is generally not desirable. However, filtering is less problematic for generating rainfall maps if the sensor density is high in relation to the resolution of the map. In this case study, the majority of filtered CMLs is in the Czech Republic and often in the cities where the network is dense enough so that the loss of several devices with questionable observations is justifiable.

Note that a set of steps to improve data quality is described and analyzed, which is not necessarily considered optimal and exhaustive, but which help to deal with the major challenges that were encountered. There is room to improve the algorithms and to add additional ones. For example, the classification of wet and dry events may be improved by including a spatial consistency check similar to what was done by Overeem et al. (2016a), instead of basing it purely on the time series of individual CMLs.

In this case study, the feasibility of combining heterogeneous CML data sets to generate transboundary rainfall maps is shown. Furthermore, straightforward algorithms that can help to deal with issues of data quality are presented. Thereby, another step was made towards minimizing erroneous data points, which need to be expected, given that CMLs are opportunistic rainfall sensors. The persistence of minor issues of data quality does not prevent the generation of consistent transboundary maps. This shows the potential of CMLs providing a basis for even larger-scale (e.g., continental) rainfall maps, which is a challenge even for dedicated sensors.

Chapter 7

Results: Countrywide Reconstruction via Random Mixing

This chapter presents the results of the case study that focuses on the stochastic reconstruction of countrywide rainfall maps for Germany. The main research question being addressed in this chapter is: What are the benefits of rainfall maps generated by stochastic reconstruction via Random Mixing (RM) using large CML and rain gauge data sets? While data and methods have been introduced in Chapters 2–5, this chapter starts with describing the specific data and methods used in this case study in Section 7.1, before presenting the results in Section 7.2.

7.1 Case-related Data and Methods

7.1.1 General Setting

In this case study data from CMLs and rain gauges in Germany is used, the RM and Kriging method for reconstruction are applied, and the results are analyzed by comparing them to gauge-adjusted radar data RADOLAN-RW via standard and the (e)SAL performance metrics. An overview of the design of the case study is given in Figure 7.1.

The analyses of this chapter consider a period of three months (June through August 2019) with an hourly resolution. The rain gauges are from the network of DWD and comprise 953 devices (see Section 2.1 and Figure 7.2). Note that the rain gauges used for the reconstructions are also deployed for the radar adjustment. The CML data set is that of Germany described in Section 2.2 consisting of 3904 sensors. In the analyzed months, there are several periods in which almost no CML data is available due to failures of the data acquisition system (see shaded parts in the time series in Figure 7.3). Such periods are disregarded in the analysis entirely. This reduces the total number of 1-hour time steps from 2208 (three months) to 1885.

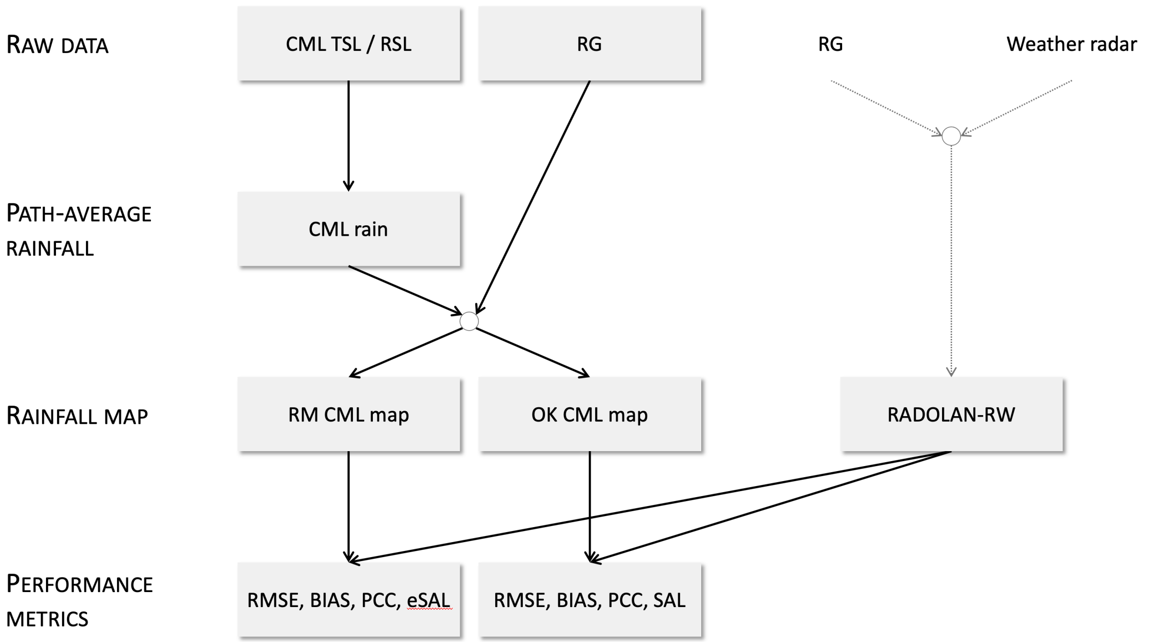

Figure 7.1: Overview of the design of the case study on countrywide rainfall maps via RM. CML data is processed to path-averaged information and then combined with rain gauge (RG) data. Two types of maps are constructed from this: one via RM and one via Ordinary Kriging (OK). The maps are validated via a comparison to RADOLAN-RW that provides a set of performance metrics. Note that the RG input data set used for the reconstruction is not independent from the RG data used for radar adjustment in RADOLAN-RW (see Chapter 2).

The sensor locations are projected onto the polar stereographic coordinate system used for RADOLAN-RW. One of the rain gauges lies outside the grid extent and thus is disregarded. The projection differs slightly between the reconstruction methods applied in this case study: For the use in RM, the locations are projected onto the grid points, while for Kriging, the exact (off-grid) values are kept.

Then, a filtering routine is applied, which concerns CML data only, and goes beyond steps that are described in Graf et al. (2020) and Section 3.2. It is a spatial sanity check in which single observations at given time steps are excluded from the analysis if they measured values that are distinctly different from the ones of neighboring sensors. As was acknowledged by Graf et al. (2020) and Polz et al. (2020) there still is a considerable amount of false-positive CML rainfall values in the used data set, despite the quality control routines that have been applied. Compared to these two studies, the focus here lies on spatial rainfall estimation and an analysis of the derived rainfall patterns. Hence, eliminating spatially isolated false-positive CML rainfall, which impacts its whole surrounding area, has a higher importance in this case study. Thus, the following heuristic filtering scheme is applied to remove spatially isolated suspicious data points: For any wet (nonzero) observation $qObs$, it is tested whether the neighboring observations are all dry. For this, only neighbors in a radius of 15 km are

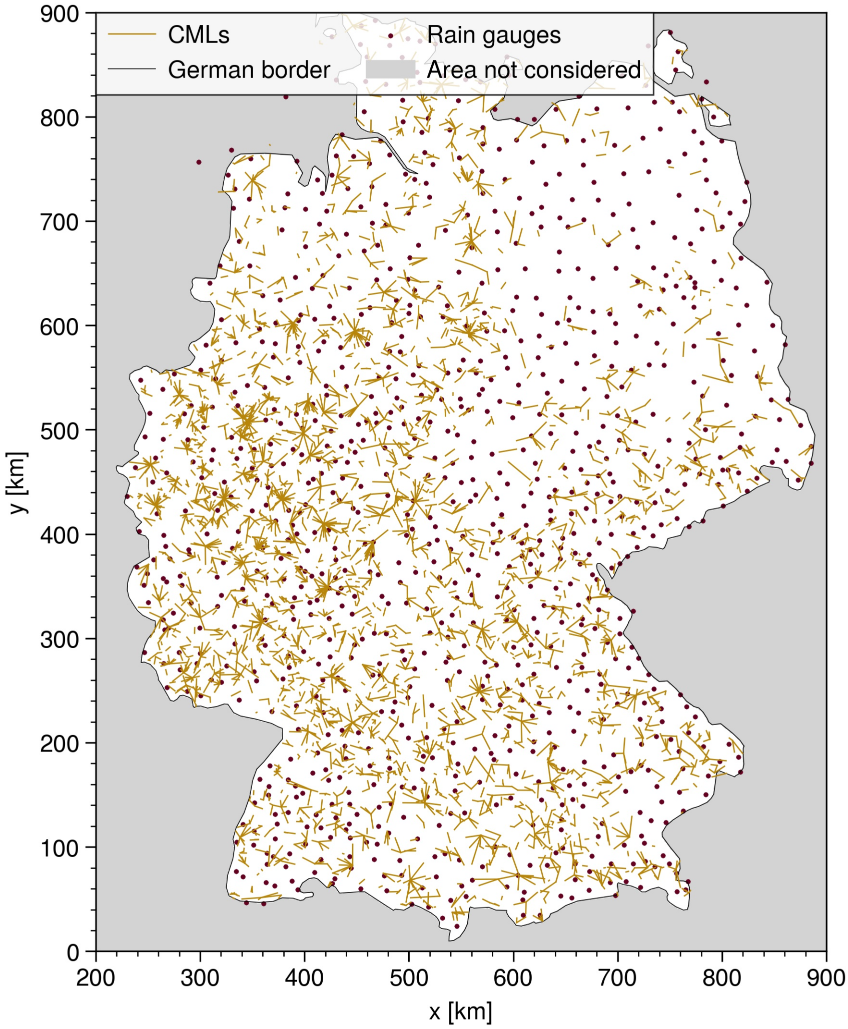

Figure 7.2: Locations of sensors. Areas outside the German borders are not considered in the evaluation. The coordinates represent the distance from the lower left corner of the RADOLAN-RW projection.

considered. If there exist at least five such neighbors and if they all observe no rainfall, the observation in question *qObs* is disregarded. This way, approximately 2.8% of CML data is removed. Two examples of the effect of this filter can be found in Figures C.5 and C.6 in the Appendix. Note that this filter is similar to the nearby link approach (Overeem et al., 2016a), which has been applied in several studies (e.g., de Vos et al. (2019), Roversi et al. (2020)) for identifying wet periods and filtering outliers. An important difference is that the filter applied here uses processed rainfall amounts instead of the raw signal.

Furthermore, whole time steps are disregarded if they are *too dry*. That is, only time steps are considered in which at least five percent of rain gauges and five percent of CMLs record some rainfall. One reason for this is the observation-based estimation of the spatial dependence structure which requires a minimum of nonzero observations. Moreover, most interesting are rainfall events that cover considerable spatial extents to allow for a meaningful pattern analysis. This measure further reduces the number of total time steps from 1885 to 819. The disregard of many rather dry time steps limits the applicability to operational use, for which a different approach to the calculation of the spatial dependence structure would be required.

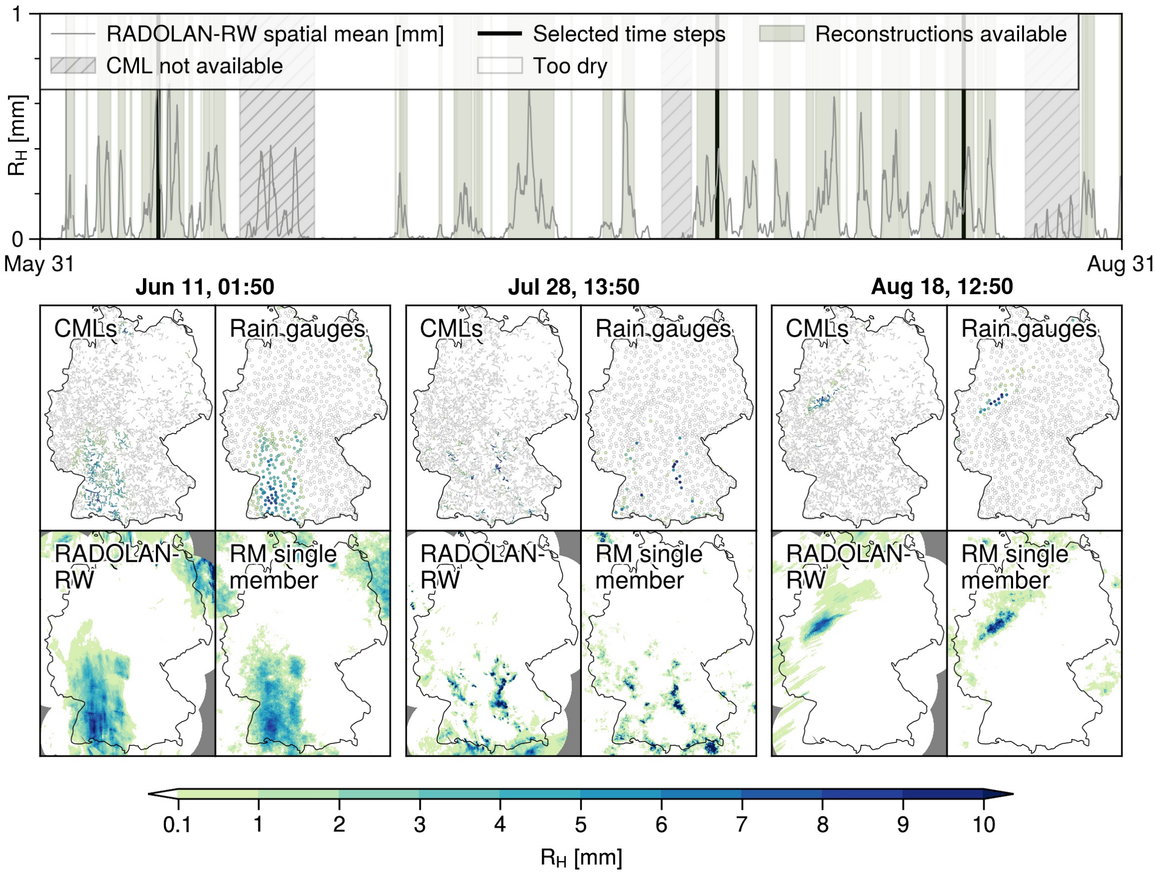

Figure 7.3: Overview of the analyzed period and the selected events. Top row: Time series of the analyzed period (June–August 2019) including spatial mean rainfall of the RADOLAN-RW reference, and indications where reconstructions were calculated and which time steps were selected for the event-based analyses. Below: For each of the selected time steps, hourly rainfall sums (R_H) of CML observations, rain gauge observations, RADOLAN-RW, and a single RM reconstruction are shown. Areas that are not covered by RADOLAN-RW as well as observations that did not record values are colored in gray.

Via the RM reconstructions, an ensemble of 20 single realizations is calculated for each time step. This number is sufficiently high to see several effects that the ensemble calculation features. At the same time, performance metrics are not expected to vary by much for greater ensemble sizes (see Section 7.2.4) and the computational complexity which depends on the ensemble size, needs to be considered as a limiting factor in RM calculations (see Section 7.2.5).

7.1.2 Selected Events: Synoptic Situation

The analysis covers the three months June, July, and August 2019. During the summer months, there is generally almost no solid precipitation, but a mixture of convective and stratiform rainfall patterns over Germany. Throughout the country, this summer was characterized by warm and dry conditions. However, several intense rainfall events took place particularly in the southern parts of the country.

In addition to the analysis over the three month period, three time steps are selected for a detailed analysis of rainfall patterns. One rainfall event from each of the analyzed months is chosen. Those events differ in terms of rainfall location, type, and synoptic conditions. All three time steps represent synoptic conditions that are common in Germany (Werner and Gerstengarbe, 2010).

The first selected time step is June 11 at 01:50 a.m. The synoptic condition at this time was dominated by high pressure over Central Europe. Germany was influenced by anticyclonic patterns. For several days the weather in Germany was characterized by strong thunderstorms which had particular strong severity in southern parts of the country. At the selected time step there was widespread intense rainfall over southwestern Germany and several rainfall cells along the Baltic Sea and the border to Poland. The second selected time step is July 28 at 13:50. The conditions were characterized by a high pressure zone over the Atlantic and low pressure over western Asia. Especially in the southern half of Germany there were local and partly very intensive convective rainfall cells. The synoptic condition of the third time step (August 18 at 12:50) was dominated by zonal westerly directions of inflow and a cyclonic regime. There was a center of low pressure over the northern Atlantic between Iceland and the British Isles, and a belt of high pressure reaching from the Azores through central Europe and Germany, to Russia. Over Germany, there was a decline in pressure from the Alps to the North Sea. These conditions led to cyclonic frontal rainfall over northwestern Germany. The synoptic conditions were derived using archived weather charts[1] and the classification defined in Werner and Gerstengarbe (2010).

7.1.3 Setting of the Computational Complexity Analysis

In addition to the quality of reconstruction, RM is analyzed with respect to working memory and run time requirements in Section 7.2.5. This involves a focused consideration of the three selected time steps described in Section 7.1.2 and subsets of the full data amount. In contrast to the other analyses presented in this chapter, the number of unconditional fields is reduced to 5000, only one ensemble member is considered, and the spatial extent is varied to assess the effect of problem sizes on the computational complexity. The arbitrarily defined problem sizes are shown in Table 7.1. They represent subregions of Germany starting with

[1] `https://wetter3.de/archiv_gfs_dt.html`, last access October 13, 2023)

a 50 km $\times$ 50 km grid (of 1 km $\times$ 1 km resolution) that is extended gradually to a size of 450 km $\times$ 450 km. The spatial extents are shown in Figure C.7 in the Appendix.

Table 7.1: Setting of the computational complexity analysis. The table shows the grid sizes, the number of observations, the number of unconditional fields K (cf. Section 4.3.3), and the number of ensemble members for the various subregions considered in the computational complexity analysis. Also, the full extent considered in the other analyses of this chapter is given for comparability. A map showing the extents of the subregions is provided in Figure C.7 in the Appendix.

Label	No. Pixels	No. CMLs	No. RGs	K	No. Ens. Memb.
Subregion “tiny”	50 $\times$ 50	9	6	5000	1
Subregion “small”	150 $\times$ 150	227	51	5000	1
Subregion “medium”	250 $\times$ 250	526	137	5000	1
Subregion “large”	350 $\times$ 350	709	194	5000	1
Subregion “huge”	450 $\times$ 450	890	274	5000	1
Full extent	700 $\times$ 900	3904	953	10000	20

7.1.4 Setup of the Analyses and Nomenclature

Figure 7.3 shows which time steps of the three months periods are considered and gives an overview of observational data, reference data, and an RM reconstruction for each of the three selected time steps. In the following section, first SAL results for these events will be presented, followed by the SAL statistics for all calculated time steps. Subsequently, Section 7.2 will cover the analysis based on standard performance metrics, and an analysis of the ensemble means of different ensemble sizes which range between three and the total of 20 ensemble members that have been calculated via RM. Finally, aspects of computational complexity are addressed.

It is generally referred to RM reconstructions by eRM, sRM, and mRM(M) if the whole ensemble, a single ensemble member, or the mean of M members are considered, respectively. Kriging reconstructions are denoted KRI. Note that for the (e)SAL analysis it is generally referred to the parameters by S, A, L omitting the leading e. For eRM, this implies that S is actually eS (likewise for A and L), i.e., a single value describing the whole ensemble.

7.2 Results of the Case Study

7.2.1 (e)SAL Analysis for the Selected Events

For the selected time steps, rainfall maps of reference, KRI, and one of the sRM reconstructions are presented together with the SAL parameters in Figures 7.4, 7.5, and 7.6. Note that in the case of RM, SAL parameters are shown for the whole ensemble (eRM) as well as for the individual ensemble members (sRM). Similar figures showing the aggregates (mRM) can be found in the Appendix (Figures C.1, C.2, and C.3).

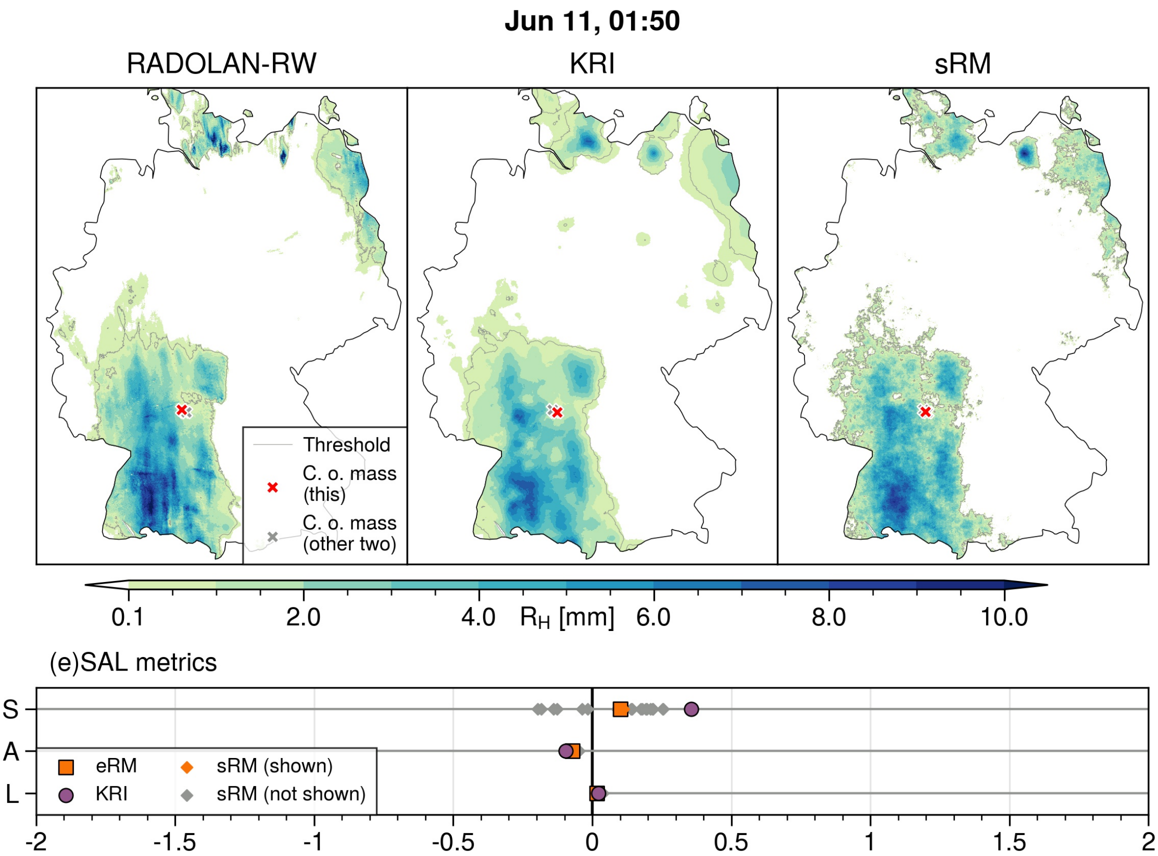

Figure 7.4: Rainfall maps and (e)SAL metrics for the first selected time step (Jun 11, 01:50). Top row: Rainfall maps for reference, KRI reconstruction, and sRM reconstruction (a single ensemble member), with centers of mass indicated by the crosses (all three crosses are shown in each map), and threshold values that encapsulate the rainfall objects (see Section 5.2.3 for details). Below the maps, the (e)SAL error metrics are shown: The framed squares represent eSAL results of eRM, smaller squares represent SAL results of all individual ensemble members, and the circles represent SAL of KRI.

On June 11, 2019 at 01:50 (Figure 7.4) there was considerable rainfall over southwestern and northeastern Germany. By visual comparison, both the sRM and KRI reconstructions are in good agreement with the reference. The spatial extent as well as rainfall amounts are well represented in the reconstructions. Comparing sRM and KRI, a general difference in the structure can be seen along the edges of the rainfall objects: KRI objects have straight edges while for sRM they are rather convoluted. This displays a high spatial variability in sRM.

The visual observations can be supported by the SAL metrics. Table C.1 in the Appendix gives an overview of metrics that are discussed in the following. The S parameters for eRM and for KRI are positive which shows that both eRM and KRI produce too widespread or less peaked objects. However, for eRM ($S = 0.100$) this value is clearly smaller than for KRI ($S = 0.355$) which indicates that the structure is better captured in eRM. The tendency for too smooth spatial gradients is implicit in OK as the variability is strongly constrained by local observations. RM, on the other hand, enables a reconstruction that does not involve this tendency. The A parameter reveals that the error in representing domain-wide rainfall is small for both eRM and KRI. Both reconstructions suffer from slight underestimations that are similar in magnitude. The amplitude errors for eRM ($A = -0.072$) and KRI ($A = -0.096$) represent approximately 93% and 91% of the reference rainfall, respectively. The L parameters show that dislocation is generally small. The domain-wide dislocations measured by L_1 indicate a shift of approximately 10 km for both eRM and KRI (both with $L_1 = 0.009$).

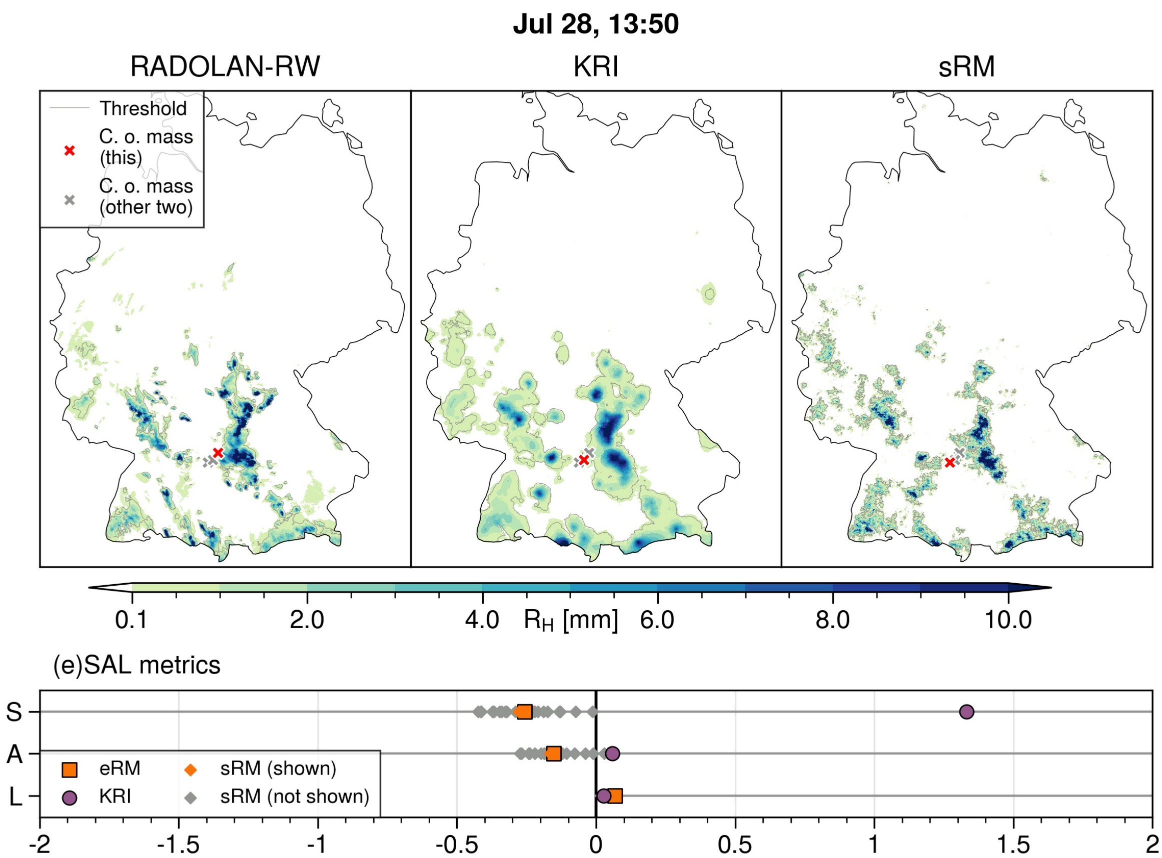

Figure 7.5: Rainfall maps and SAL metrics for the second selected time step. The maps show the reference data, a Kriging reconstruction, and a single sRM reconstruction, with centers of mass and threshold values that encapsulate the rainfall objects. Below the maps, eSAL results for eRM are shown by the framed squares, SAL of individual sRM members by the smaller squares, and SAL of KRI by the circles (cf. Figure 7.4).

The second selected time step (July 28, 13:50, see Figure 7.5) is characterized by several convective cells with large rainfall amounts over southern Germany. As for the first event, the overall picture is captured by the reconstructions. For this time step, strong differences are observable in the representation of the rainfall structures between sRM and KRI. sRM represents the small scale spatial variability and produces many narrow but peaked rainfall objects. KRI, on the other hand, is characterized by much broader objects and less locations with very high rainfall amounts. The sharp spatial gradients observable in convective conditions are not captured in KRI. Instead, fewer features are present that are connected over relatively large extents.

The difference in structure that can be seen in the maps, is also represented by the S parameter which is very high for KRI ($S = 1.331$) and much closer to zero for eRM ($S = -0.257$). Again, the large structural error demonstrates that rainfall objects are too smooth and widespread in the KRI reconstruction, and confirm that KRI has shortcomings in producing adequate peaks and finer structures. The amplitude error reveals that KRI represents the overall rainfall amount well. Its A value of - 0.058 relates to a representation of approximately 94% of reference rainfall. For eRM, an underestimation ($A = -0.152$) is observed, which translates to approximately 86% of reference rainfall. As in the aforementioned example, the location error is small for both eRM and KRI. The displacement of the total center of mass is towards the south-west for both the shown sRM ensemble member and KRI. The L_1 component of eRM (0.029) and KRI (0.014) indicate dislocations of the total center of mass of approximately 33 and 16 km, respectively.

The third selected time step (August 18, 12:50, Figure 7.6) is characterized by frontal rain that covers the northern parts of Germany. In contrast to the other examples, a clearly anisotropic rainfall pattern can be observed, i.e., rainfall objects are elongated in SW-NE direction in the reference. The elongation can also be seen in the reconstructions on a large scale. However, on a smaller scale, e.g., when focusing on single peaks, the elongation is not well represented in the reconstructions. Moreover, some of the rainfall objects of rather low amplitudes that are visible in the reference are not present in both sRM and KRI. On the other hand, there are several small objects that are present in KRI but not in the reference or sRM. These might be attributed to false-positive rainfall values of the CMLs that were missed by the applied filter (see Section 7.1). With regard to the relation of spatial extent, sRM and KRI reconstructions differ substantially. For KRI, a large area is covered by moderate rainfall, while for sRM the spatial extent is smaller but the peaks are higher. Especially in the northern and western parts of the domain, KRI produces widespread objects and sRM several smaller ones.

Similar to both events discussed above, the structure error is smaller for eRM ($S = 0.158$) than for KRI ($S = 0.376$). The amplitude error is slightly positive and similar for KRI and eRM. Their values ($A = 0.220$ for KRI) and ($A = 0.142$ for eRM) represent approximately 125% and 115% of reference rain, respectively. Location errors for the eRM and KRI are particularly small.

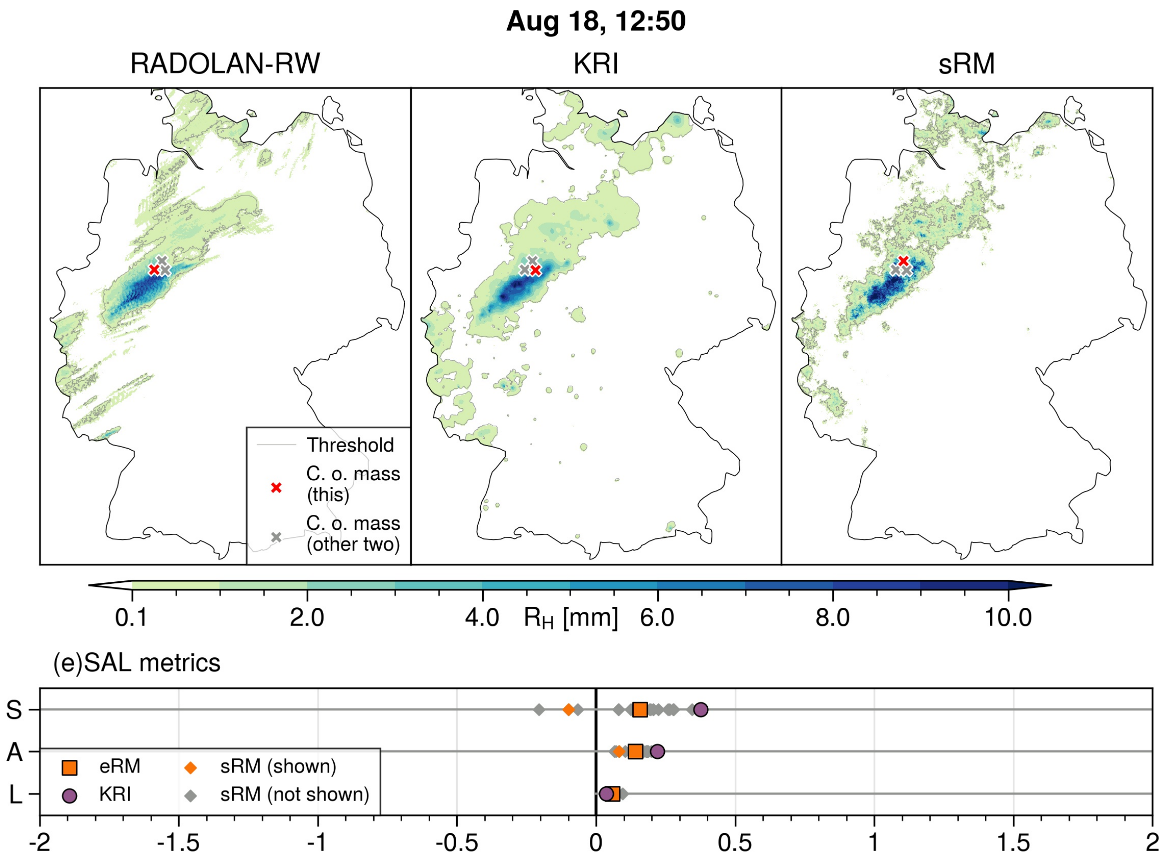

Figure 7.6: Rainfall maps and SAL metrics for the third selected time step. The maps show the reference data, a Kriging reconstruction, and a single sRM reconstruction, with centers of mass and threshold values that encapsulate the rainfall objects. Below the maps, eSAL results for eRM are shown by the framed squares, SAL of individual sRM members by the smaller squares, and SAL of KRI by the circles (cf. Figure 7.4).

7.2.2 (e)SAL Analysis: Overall Statistics

The following presents the SAL results for the whole analyzed period. Figure 7.7 shows boxplots of the parameter distributions for eRM, mRM(20), and KRI over time. Note that sample sizes of the parameters do not differ among the three cases. While S of KRI and mRM(20) is mostly strongly positive (median of 0.583 and 0.530, respectively), S of eRM displays smaller values (median of - 0.110). This shows the tendency of KRI to produce rather widespread, flat objects, while eRM has only a weak tendency for too peaked objects. mRM(20) is similar to KRI with regard to the structural error. For the A parameter, there is, by definition, no difference in eRM and mRM(20). From median values of - 0.159 it follows that 85% of the reference rainfall amount is represented by eRM. For KRI, the median A value is - 0.035 which corresponds to approximately 97% of the reference rainfall amount. Compared to S and A, the location error is relatively small for eRM, mRM(20), and KRI. Moreover it shows a narrow range of values. Median values of 0.042 (eRM), 0.057 (mRM(20)), and 0.059 (KRI) reveal a slight advantage for eRM with regard to representing the location of rainfall. The median L_1 parameter of eRM (and mRM(20)) is 0.021 which corresponds to a distance in the location of the total center of mass of approximately 24 km. For KRI, the median L_1 is only slightly higher (0.023).

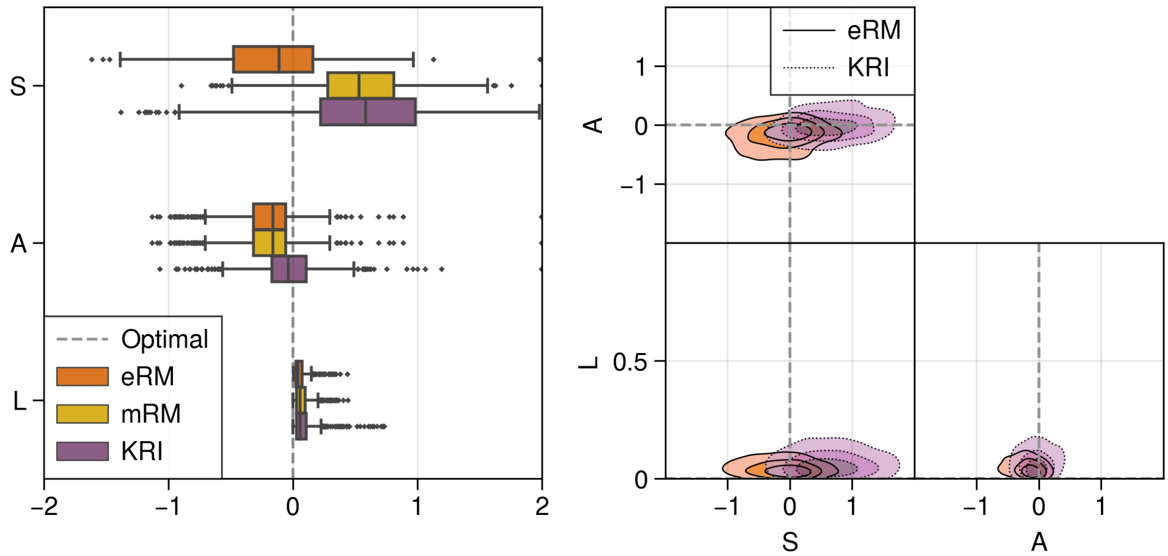

Figure 7.7: Distribution of the (e)SAL metrics for the whole analyzed period. Boxplots for eSAL of eRM, SAL of mRM(20), and SAL of KRI (left); probability density of the SAL value distribution in contour plots (right) of A vs. S, L vs. S, and L vs. A. For each of the reconstructions, the outer, middle, and inner contour represent a probability density of 25%, 50%, and 75%, respectively.

Figure 7.7 also presents the internal mutual dependencies of the three SAL parameters. It should be noted that the SAL parameters are constructed (e.g., by applying field dependent rainfall threshold values and scaling of objects for the calculation of S) such that they measure distinct features and do not exhibit strong correlation. In fact, Figure 7.7 (right) suggests that the parameters can be considered largely independent from one another.

On the contrary, a clear correlation can be found when considering the overall rainfall amount. Figure 7.8 shows all data points in the time series colored according to the spatial mean rain of the RADOLAN-RW reference. For all parameters and particularly for A, it can be seen that time steps with little rain display a larger scatter. Moreover, a small positive correlation is observable between A and S in cases with little rainfall. Strong rainfall on the other hand is associated with smaller SAL errors and smaller scatter. These observations are similar for eRM and KRI. Since the (e)SAL parameters are relative measures, they are likely to be more sensitive and more correlated under conditions of little total rain.

7.2.3 Analysis by Standard Performance Metrics

To put the results from the SAL analysis into perspective, the reconstructions were also analyzed using standard performance metrics that are based on a pixel-by-pixel comparison. A summary of these metrics for eRM, mRM(20), and KRI is shown in Figure 7.9. Note that

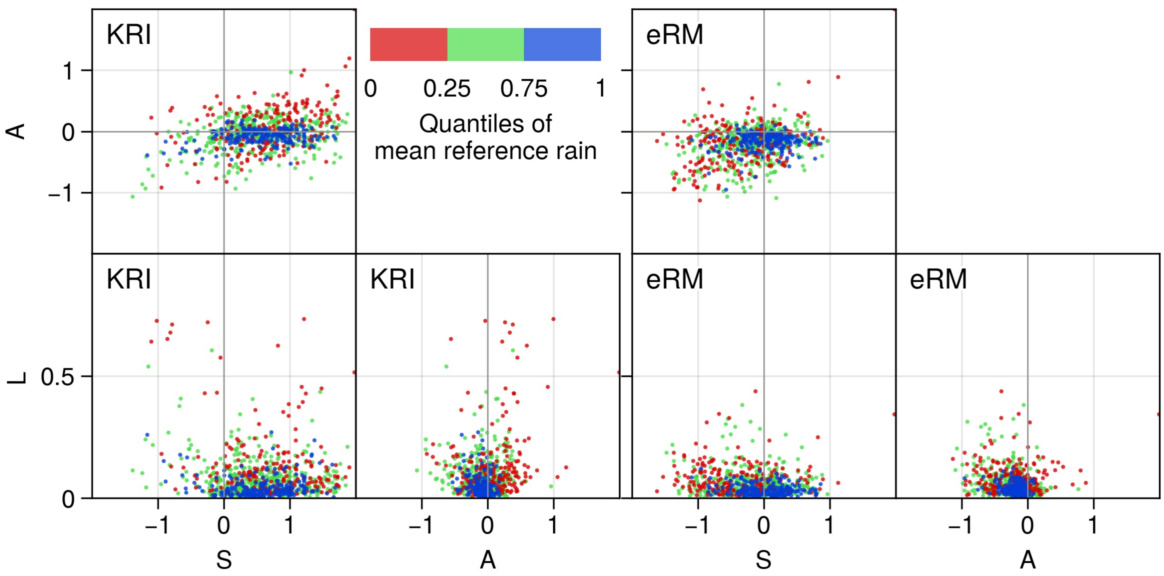

Figure 7.8: Relation of (e)SAL parameters as scatter plots for all available time steps shown separately for KRI (left) and eRM (right). The markers are colored according to rainfall amount for which three categories are considered: 25% time steps with least, 50% with intermediate, and 25% with highest mean rainfall amount of the RADOLAN-RW reference.

for eRM, the median over the ensemble dimension is considered. The metrics for sRM are shown in Figure C.4 in the Appendix.

The correlation index *PCC* shows a wide range of positive values in all three cases. eRM performs worse than KRI with regard to this metric. The median (over time) *PCC* is 0.651 and 0.762 for eRM and KRI, respectively. mRM(20) (median of 0.766), however, shows correlations that are slightly higher than KRI correlations. In a similar manner eRM generally performs worse than KRI with regard to *RMSE*. Higher errors can be seen for eRM (median of 0.274 mm) than for mRM(20) and KRI (median of 0.164 mm and 0.159 mm, respectively). *RMSE* shows a strongly skewed distribution with several outliers that have high errors. The *BIAS*, which is directly related to the *A* parameter of the SAL analysis, is similar for eRM and mRM(20) (median of - 0.151 and - 0.147, respectively). It is also negative but of lower magnitude for KRI (median of - 0.034). All the reconstructions show a tendency for underestimation.

The analysis of standard performance metrics displays a contrast to the SAL analysis above, and thereby highlights that metrics based on pixel-by-pixel comparison cannot account for all relevant features of a reconstruction. Focusing on *PCC* and *RMSE*, KRI has an advantage over eRM. The pattern analysis, on the other hand, suggested that eRM is capable of reproducing the structure better than KRI. In both regards, mRM(20) is closer to KRI than eRM. That is, the shortcoming of eRM with regard to *PCC* and *RMSE* is more than compensated when considering mRM(20); however, at the same time, the advantage of eRM with regard to the structure is reduced for mRM(20). So far, only single fields have been

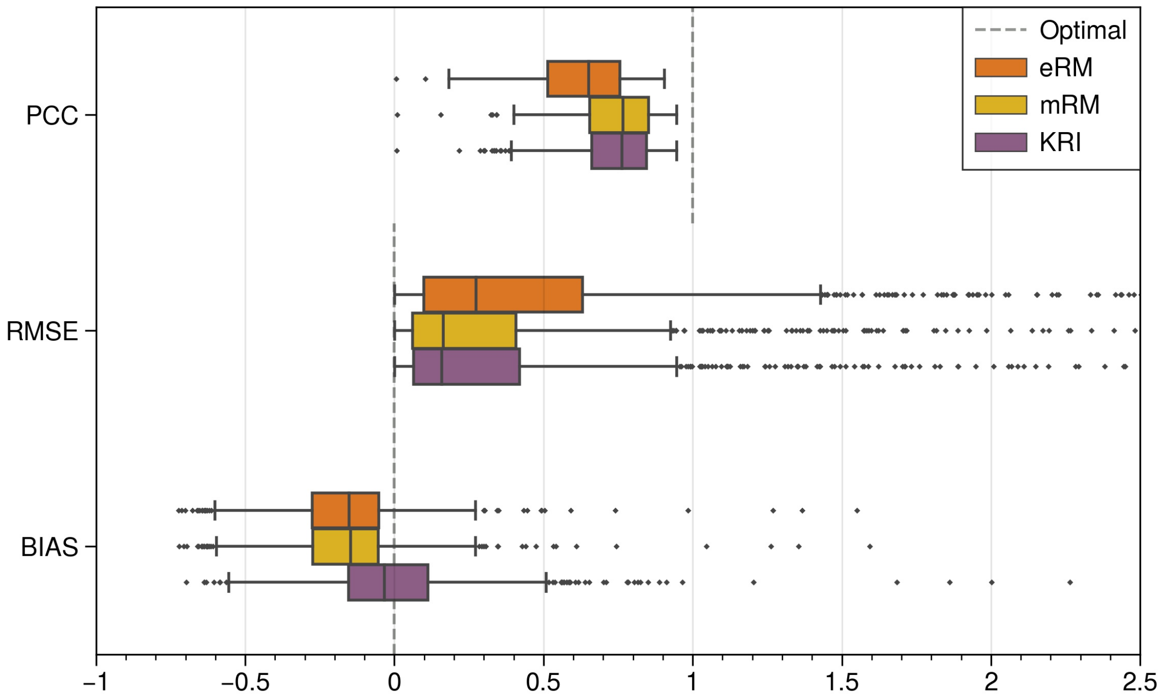

Figure 7.9: Pixel-based performance metrics for the whole analyzed period. For eRM, the median of the ensemble is considered.

compared with the mean of the whole ensemble containing 20 single members. The next section will present an analysis that takes into account averages over different ensemble sizes.

7.2.4 Analysis of Ensemble Averages

It was shown that eRM has benefits over KRI with respect to pattern representation and shortcomings with respect to standard performance metrics, and that considering mRM(M) ensemble means can be used to reduce the differences in both cases. So far, single fields and the mean of the whole ensemble which consists of 20 members were considered. Now, the performances of various aggregation sizes $M \in [1, 3, 5, 10, 20]$ are compared (Figure 7.10), whereas mRM(1) is equivalent to sRM. Apart from the case $M = 20$, a subset of the ensemble is selected randomly. Various combinations of random selections were tested, which showed that the selection does result only in negligibly small variance of the metrics. Note that the number of possible combinations is different and can be very large depending on M, such that the calculation of all combinations is not practicable.

It is found that standard metrics like *PCC* and *RMSE* that indicate a relatively low performance of sRM improve significantly once ensemble mean fields even of small sizes are considered. Both *PCC* and *RMSE* are very close to KRI for mRM(5) and almost equal for mRM(10). As seen above, mRM(20) already performs slightly better than KRI. However, it can also be seen that the rate of change levels out for the large ensemble sizes. The

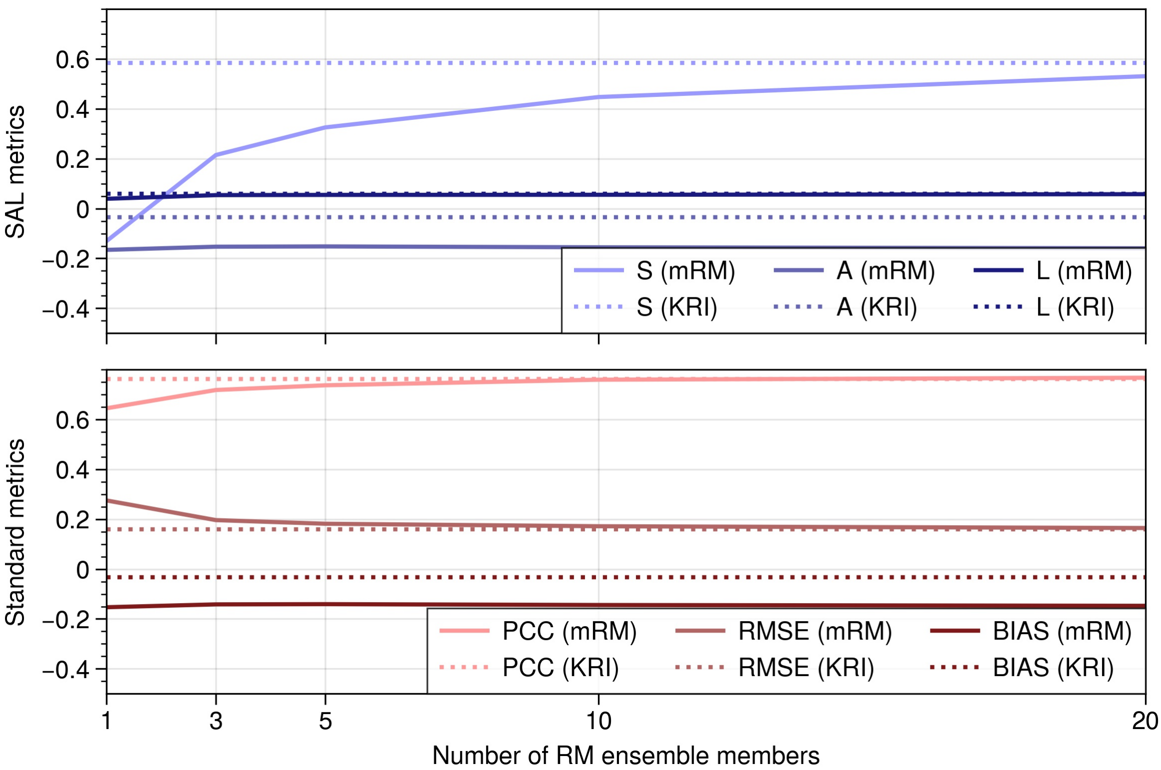

Figure 7.10: Various performance metrics for ensemble mean fields of different ensemble sizes. Solid lines represent mRM and dotted lines KRI. The latter is represented by a single value and not dependent on the ensemble dimension.

structure error S, on the contrary, deteriorates with increasing M. While it is -0.130 for a single sRM member, it is 0.325 for mRM(5). It further increases for larger M but levels off, too. In all cases the structure error of mRM is clearly below S of KRI. The location error is also lowest for sRM single fields. It increases slightly for mRM(3) but does not change for larger M. Besides, it is almost equal to L of KRI once $M > 1$. The A parameter and the $BIAS$ are generally not influenced by the ensemble size, and slightly worse for sRM and mRM compared to KRI.

These comparisons highlight the potential that comes with the ensemble calculation in RM. Single fields show better structure representation but worse standard metrics. However, averaging over the ensemble dimension can help to remove the shortcomings of RM with regard to the latter set of metrics. Although the structure representation of these ensemble averages is worse than that of RM single fields, it is still better than that of KRI. The ensemble size considered for averaging can be adjusted to specific use cases, depending on which aspect of the field is of most interest. No large changes in the metrics are expected for ensemble sizes that are greater than the one considered in this case study, since Figure 7.10 clearly shows the convergence of the metrics with increasing number of RM ensemble members. Moreover, the size suffices to achieve PCC and $RMSE$ values for mRM that are similar to KRI. Only the overall underestimation of RM cannot be reduced by averaging over the ensemble dimension.

7.2.5 Analysis of the Computational Complexity

In addressing the research question in the previous sections, RM was compared to OK. Hence, it is of interest how these two methods differ with regard to their computational complexity. Being a stochastic method, RM is computationally clearly more demanding than OK. Considering the full data extent, the time to compute an RM ensemble for one time step was on average 3.8 h with most time steps requiring less than 2 h but a few even more than 10 h (using *AMD EPYC™ 7452* computers with 32 cores and 2.35 GHz frequency[2]). OK, on the contrary, produced solutions (albeit no ensembles) generally in less than 1 minute per time step. Moreover, RM requires large working memory resources in the case of the consideration of a large grid. For the countrywide case study, approximately 30 GB and 1 GB of working memory per time step were required for RM and OK, respectively.

To assess computational demands in more detail, RM is examined in a smaller setting as defined in Section 7.1.3. For this analysis, an *Intel® Xeon® Processor E5-4650 v3* with 12 cores and 2.1 GHz frequency was used[3]. Figure 7.11 shows time and working memory requirements of the RM algorithm and selected subroutines depending on the size of the problem and for the three independent time steps. It can be observed that regarding both time and memory requirements, the generation of unconditional fields plays a major role. In terms of memory it is obviously the single dominant aspect. Regarding time, also the fitting of CML data and the Metropolis-Hastings random walk (MHRW) contribute significantly to the overall demand. The MHRW also requires a noticeable share of the total working memory while the fitting to CML data does not. The initial aspect of fitting the spatial model requires no significant amount of working memory and not much computation time despite being an iterative process. The general picture is similar in all three time steps, however, time requirements vary much more between the time steps than do memory requirements. Moreover, time requirements vary more between the independent model runs (indicated by the shaded areas in Figure 7.11) compared to memory requirements. An exemplary evolution of used working memory over time is shown in the Appendix in Figure C.8.

Regarding computation time, it is important to consider the ensemble size when assessing the share of the subroutines. The unconditional fields need to be constructed only once, regardless of the number of ensemble members that are generated. The MHRW is partly dependent on the ensemble size as it needs to be conducted for each new ensemble member, whereas it requires significantly less time for the second and all following members. The part

[2]https://www.amd.com/en/product/8801, last access October 13, 2023

[3]https://ark.intel.com/content/www/us/en/ark/products/85762/intel-xeon-processor-e5-4650-v3-30m-cache-2-10-ghz.html, last access October 13, 2023

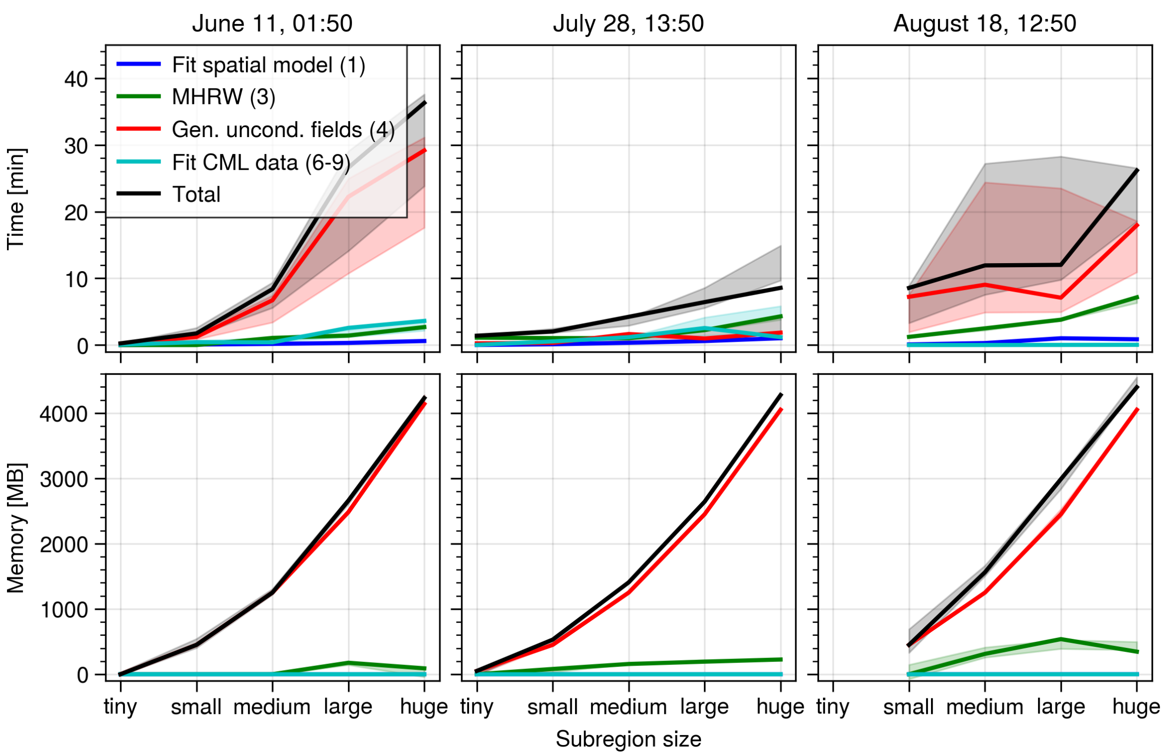

Figure 7.11: Computational complexity of selected parts of the RM algorithm for the three selected time steps and dependent on subregions of various sizes (see Table 7.1 and Figure C.7 in the Appendix). In each case, only one ensemble member is generated. The computation was run 10 times for each case and the shaded area represents the mean ± one standard deviation of those independent runs. The solid lines all represent a particular randomly selected run. For the time step Aug, 18, the *tiny* case could not be calculated due to too few wet observations. Note that the black line *Total* refers to the full algorithm and not only to the sum of the selected subroutines. The numbers behind the subroutines refer to the steps described in Section 4.3.3.

associated with fitting the CML data, on the contrary, is fully dependent on the number of ensemble members that are calculated and can therefore become significant for large ensembles. Moreover, this subroutine is not deterministic and can be variable in speed dependent on how fast an appropriate solution is found.

While the observations show the rising computational demands for large-scale reconstructions, they also reveal potential for improvement. For instance, memory requirements might be reducible by tuning the number of unconditional fields K to the problem size. However, optimizing the method was not focused upon in this thesis.

7.3 Summary and Discussion

The RM method was applied for producing countrywide spatial rainfall estimates based on CML and rain gauge data and a validation was applied using (e)SAL, a specific set of metrics for structure, amplitude and location errors of spatial data. It was found that

RM reconstructions show a reasonable agreement with the reference data. Moreover, when comparing RM reconstructions with Ordinary Kriging reconstructions (KRI), it was shown that the former has advantages in reproducing rainfall patterns, while at the same time, the single RM fields display lower performance than KRI fields when analyzed via standard performance metrics.

RM works fundamentally different from KRI. It does not interpolate observation values in space, but rather generates possible rainfall fields that agree with the observations. The generated rainfall fields follow a specific spatial dependence structure derived from the observations. This explains the much better performance of RM rainfall fields with regards to spatial structures compared to the KRI fields which are always much too smooth. Especially for complex patterns this aspect is crucial. The greatest advantage of RM over KRI was found for the case of convective conditions, where spatial variability is particularly pronounced. However, the fact that RM generates possible rainfall fields can result in large variations further away from the observations which constrain the generation process. Hence, single RM rainfall fields can show large deviations from the reference in regions without observations, leading to relatively weak performance according to standard metrics. When considering an ensemble of rainfall fields, this variation does, however, reflect the uncertainty of the rainfall field reconstruction.

The possibility of RM to generate an ensemble of possible rainfall fields that fit to the point observations of the rain gauges and the path-averages from CMLs is a major advantage. Considering ensemble averages, a reduction of the variability that is present in the single ensemble members can be achieved. Such averages are similar to a KRI reconstruction with regard to most performance metrics. They show a slightly worse pattern representation, but enhanced pixel-based metrics, compared to single ensemble members. Thus, RM allows the consideration of a spectrum of solutions, from single ensemble members to ensemble averages of various sizes, depending on the application.

A disadvantage of RM observed in this case study is its stronger (compared to KRI) tendency for underestimation. This, in contrast to the other analyzed properties of the fields, cannot be influenced by the consideration of ensemble aggregates. However, the underestimation might be minimized by adjustments in the RM algorithm. For instance, the estimation of the marginal distribution can probably be optimized and calibrated to reduce this bias. Furthermore, shortcomings were observed in representing the anisotropy of rainfall objects, which might be accounted for in future applications. Also, the inherent computational complexity provides an obstacle to the applicability of RM. This, however, could also be mitigated by optimizations of the code and the choice of parameters.

In spite of the limitations, it could be shown that RM has the potential to produce valuable estimates that can outperform standard methods depending on the use case. For certain hydrological models, it might be useful to consider single RM ensemble members that give a true representation of spatial gradients. This allows the assessment of expected spatial extents relative to the total rainfall amount of a rainfall object. That is, RM can reduce overestimation of spatial extents as well as underestimation of peaks. One can further use different ensemble members as model input for the estimation of uncertainties, or consider ensemble averages which are less variable and more conservative.

This shows that RM constitutes a suitable method for precipitation estimation. It is capable of dealing with a combination of different and extensive observational data appropriately, produces fields with high quality pattern representation, and allows for different perspectives via the consideration of ensemble aggregates.

Chapter 8

Conclusions

This chapter aims at bringing the results presented above into a broader perspective. First, the research questions posed in the beginning are answered directly in Section 8.1. In Section 8.2, the strengths and limitations of the methods are discussed. Finally, Section 8.3 presents an outlook for further related research.

8.1 Answers to the Research Questions

Can two large independent CML data sets be combined and processed jointly to generate consistent transboundary rainfall maps?

Two CML data sets from Germany and the Czech Republic, each containing thousands of sensors, were combined in the first case study of this thesis. Initially, the data was processed by algorithms of quality control (QC), rain rate retrieval, and a spatial reconstruction, which had been developed for the German data set. Applying these algorithms, acceptable transboundary rainfall maps for the border region of Germany and the Czech Republic could indeed be generated.

However, the resulting maps were of limited quality and not sufficiently consistent throughout the considered domain. Particularly, several artifacts induced by a few but strong outliers could be observed. It was found that a reason for these issues was poor data quality that affected a considerable amount of raw data. For instance, signal levels that could clearly not be attributed to rainfall or any other atmospheric process persisted for periods of various lengths. Moreover, strong periodic fluctuations, or gaps in the time series induced the artifacts in the maps. Such issues of data quality can partly be explained by the CML hardware characteristics which influence the way rainfall reflects in the observable signal. As the hardware characteristics differ significantly between the data sets, so do the observed issues. However, direct physical explanation for the issues cannot be found in all cases. Technical details of data collecting and storing might explain some aspects but these are not easily accessible. Regardless of their reasons, issues of data quality proved to be the crucial obstacle for achieving consistency and a satisfying level of quality of the maps.

Hence, the QC aspect of the applied algorithms required particular attention as the measures that had been developed for a single data set were not capable of addressing all data quality issues of the combined data sets. Accordingly, new algorithms were developed that filter periods of clearly impaired data, fill gaps where the signal loss is assumed to stem from heavy rainfall, or remove whole sensors due to inadequate hardware characteristics. The large amount of data required automatic algorithms that could be applied universally to both data sets even if the issues were not all present in both data sets. Overall QC involved a reduction of data which is acceptable given a high sensor density particularly in regions where the filtering was most effective. While QC required adjustments, the other parts of the processing, namely, rain rate retrieval and reconstruction could be applied to the combined data set without substantial changes. It was shown that the renewed QC improved both the path-based rainfall estimates as well as the consistency of the rainfall maps.

The results show that it is possible to combine two CML data sets from Germany and the Czech Republic to generate seamless transboundary rainfall maps for the border region of the two countries. The full processing from raw data to consistent transboundary rainfall maps could be conducted jointly via universal algorithms. These first transboundary CML-based rainfall maps constitute a step towards using CMLs for addressing hydrometeorological questions on continental scale or inter-state border regions.

What are the benefits of rainfall maps generated by stochastic reconstruction via RM using large CML and rain gauge data sets?

Generally, RM is capable of producing rainfall reconstructions which represent both the rainfall statistics as well as the local observations. The marginal distribution and spatial structure of rainfall can be inferred directly from the data. Moreover, rain gauges and CMLs can be treated as independent constraints considering their point-like and path-based nature. Via the creation of ensembles, RM additionally provides a probabilistic solution.

Countrywide rainfall reconstructions were generated for the first time via RM using a large CML and a large rain gauge data set. The results show that RM ensemble members represent the rainfall patterns better than Ordinary Kriging (OK) reconstructions. Especially the tendency for producing smooth spatial gradients, which is an inherent feature of most standard reconstruction methods including OK, was not observed when applying RM. This advantage could be quantified by the object-based eSAL validation approach which showed significantly smaller structure errors of RM compared to OK. The possibility to reconstruct rainfall patterns and thereby spatial variability of rainfall more accurately constitutes an important benefit: particularly, for events of strong but local convective rainfall, it can be crucial not to overestimate the spatial extent or underestimate the maxima of rainfall cells to assess the hydrological response correctly. In fact, RM showed the strongest advantage for the selected event that represented such convective conditions.

However, the reconstructions generated by RM showed a stronger general underestimation than the ones generated by OK. Also, the RM reconstructions showed weaknesses when evaluated by standard performance metrics that compare the individual pixels directly. The discrepancy between quality assessments via the pixel-based comparison and the eSAL approach shows the importance of choosing appropriate performance metrics. Different metrics can highlight different beneficial aspects but they cannot provide a universal measure of quality.

Despite some ambiguity of the benefits, RM has the clear advantage of allowing an ensemble calculation and thereby providing a bandwidth of perspectives ranging from the consideration of single ensemble members to ensemble averages. Single members provide highly variable solutions with a good pattern representation that might be punished in a pixel-wise comparison. Ensemble averages, on the contrary, are closer to a deterministic *best guess*, thereby reducing errors at unobserved locations at the cost of reducing pattern representation quality. Nevertheless, by averaging over an appropriate number of ensemble members, the RM reconstruction shows similar standard metrics but still an advantage in the structure representation compared to OK. Moreover, the uncertainty about estimates is reflected by the ensemble variability and can provide valuable insights when using the reconstructions for hydrological applications. Thereby, RM proved to be the more flexible approach when various aspects of the rainfall reconstruction should be considered. It needs to be noted, however, that the flexibility provided by the stochastic RM approach involves a significant computational effort when considering large amounts of data. While this could certainly be optimized, it is likely to remain clearly higher than that required for OK.

8.2 Strengths and Limitations

This thesis confirmed that CMLs are valuable opportunistic rainfall sensors and that they have an enormous potential for large-scale rainfall maps. The first transboundary CML-based rainfall maps constitute an important step towards continental scale rainfall maps which are so far only provided by satellites or merged radar products with limitations in either accuracy, spatiotemporal resolution, or spatial extent (Huffman et al., 2020; Haase and Johnson, 2018). However, many steps remain towards achieving CML-based continental rainfall maps. They would involve combining not only two but many independent data sets. And, while the data sets used in this thesis have been very different from one another in terms of network characteristics and data quality issues, some potential challenges did not have to be addressed. For example, common ways of raw data sampling involve recordings of minimum and maximum values over 15-minute periods (Messer, 2006; Overeem et al., 2016b; Roversi et al., 2020; Overeem et al., 2021; Nebuloni et al., 2022) as well as the instantaneous sampling of the used and other data sets (e.g., Andersson et al. (2022)). Combining data sets with different sampling strategies might involve additional difficulties compared to combining two data sets that are similar in this regard. However, it can be considered promising that only QC needed to be extended in the presented case study and that the main algorithms for rain rate retrieval proved to be transferable. This indicates that the retrieval algorithms are relatively robust despite many remaining limitations in the understanding of additional factors that cause attenuation (Van Leth et al., 2018). Nevertheless, it cannot be assumed that the extended QC conducted in the presented case study is sufficient to deal with all potential issues that might be found in other data sets. Hence, thorough investigation of the data is expected to be a general requirement for their usage and combination. As was done in this thesis, the presented QC algorithms should generally be defined to be universally applicable. For other data sets other algorithms might be required but this is not necessarily problematic as long as the erroneous data of one set is not easily confused with the sound data of the other set, and as long as there is enough useful data still available after QC.

In testing the feasibility of generating transboundary maps, the first case study put less focus onto the aspects of the most adequate consideration of the path-averaged nature of CML observations in reconstructions. In this case study, CML observations were reduced to virtual gauges. Although the disregard of the CML path can be considered state of the art for large-scale CML-based rainfall maps (Overeem et al., 2016b; Graf et al., 2020), it is certainly a simplification which diminishes the underlying information. The consequences of this simplification depend on the path lengths and the spatial structure of the rainfall and can be severe if long CMLs are considered in situations of highly variable convective rainfall. Therefore, the second case study aimed at adequately representing the path-based CML observations, for which RM was selected. It deals with CMLs in an adequate manner as it considers all values along the paths in the matching of the reconstruction with the observations. The uncertainty about the exact location of rainfall along the path can then be represented via the ensemble spread.

Besides these advantages in the path-representation and the capability of generating accurate rainfall patterns, this thesis also revealed the challenges of applying RM with large amounts of data. The algorithm had to be adjusted until finally the considered data was manageable. Further increase of data, e.g., as would be required when considering transboundary or continental-scale rainfall maps, may be difficult. The usage with almost a thousand rain gauges and approximately 3900 CMLs was already computationally demanding and hence technical issues could inhibit the applicability for even larger data sets. And even given feasibility, long calculation times might strongly inhibit the usage of the method for close to real-time application. This aspect is obviously dependent on the computational resources and whether the method can be optimized in this regard.

RM was not only good in representing CML observations but very suitable to the combination of CMLs and rain gauges as it can account for both types of observations separately. Despite this advantage for regions where both sensor types exist, a considerable limitation of RM is that it cannot easily be applied with CML data only. It requires point data like rain gauge observations to estimate the rainfall statistics, that is, the marginal distribution and the spatial dependence structure. Consequently, RM could only be applied with a pure CML data set if the statistics were derivable from CMLs. This would require, for example, to reduce CMLs to virtual gauges only for the derivation of the statistics but to consider full paths for the conditioning of the fields. However, the path-averaged values would lead to a marginal distribution that does not represent extreme values, and also to a spatial model that might overestimate correlation distances. Another method has been presented to enable the estimation of the spatial model accounting for the effect of path-averaging by Eshel et al. (2022). However, it has so far not been used within the RM algorithm or with any real CML data. Notably, rainfall statistics can also be obtained from climatological data as done, e.g., by Overeem et al. (2013) and Overeem et al. (2016a) for their Kriging-based reconstructions. This, however, requires additional data, which may, in general, not represent the statistics of the considered event accurately. The difficulties in using RM with CMLs only constitute a significant limitation, especially since the largest potential of CML-based products is precisely in regions without or with a small number of dedicated sensors such as rain gauges (David et al., 2013). Moreover, it should be noted that by using both rain gauges and CMLs, the effect of each of the two sensor types has not been analyzed separately in this thesis.

In focusing on the generation of rainfall maps, this thesis mostly leaves out the temporal component of rainfall, which is not less relevant (Cristiano et al., 2017). All reconstructions that have been generated in this thesis represented single points in time independent of their temporal correlation. Also, RM as used in this thesis cannot easily incorporate the temporal correlation between time steps. While the disregard of time in the generation process can certainly be considered a shortcoming, meaningful temporal evolution of rainfall over several hours could nevertheless be shown in Section 6.2.5. The consistency over a series of several time steps constitutes one aspect of the temporal aspect, whereas the long term extent is another. Also long-term estimation has its limitations with the approaches presented in this thesis: A general shortcoming of CML-based rainfall estimation is the fact that sensing solid precipitation is not possible in comparable quality as is sensing liquid precipitation (Vivekanandan et al., 1999). Overeem et al. (2016b) and Graf et al. (2020) showed that the quality of estimation is significantly reduced in winter months when there is a considerable amount of solid precipitation in the respective study regions (the Netherlands and Germany).

While this limitation inhibits long-term analyses that cover all months of the year in colder climates, it has no negative effect for most periods and most regions as rainfall is clearly the predominant type of precipitation.

8.3 Outlook

While the potential for CML-based continental rainfall maps was shown from a scientific perspective, legal and administrative constraints remain the dominant factors preventing such maps in the nearest future. Without an economic benefit for the network providers, data access and exchange is likely to remain limited (Chwala and Kunstmann, 2019). Nevertheless, progress in opening up the data access exists. Recently, a data set containing hundreds of CMLs in Gothenburg, Sweden has been made publicly available by Andersson et al. (2022). While such a network from a city is far from the continental scale, it provides the first example of openly shared extensive amounts of CML data, and might be followed by others that cover larger areas. Although not publicly shared, the access and application of CML data is slowly increasing also in several other countries around the globe as shown by relatively recent studies in Brazil (Rios Gaona et al., 2018), Sri Lanka (Overeem et al., 2021), and Kenya (Kumah et al., 2022). If data accessibility continues to increase, the presented case study on transboundary maps provides a basis for research on even larger scales or in other regions.

Despite the fact that no other studies have combined independent CML data sets, there is progress to enabling broader consistent approaches of working with CML data. The EU cost action OPENSENSE[1,2] was initiated to foster interoperability and international collaboration with CML and other opportunistic rainfall data. A major step already reached is the agreement on data naming and storing conventions documented in Fencl et al. (2023) (under review).

Moreover, the scientific advances in CML-based rainfall estimation have led several meteorological services in Europe to envisage the operational use of CMLs in combination with other sensors[3]. In these cases, sharing data could be made profitable for the network providers. Once the meteorological services can significantly improve their products using the additional information, they might request and pay for long-term, stable data access.

The future applicability of CMLs will, however, not only depend on data availability but also on their quality as rainfall sensors. The number of CMLs worldwide is likely to increase (Chwala and Kunstmann, 2019) which is promising especially in face of the limited amount of dedicated rainfall sensors (Lorenz and Kunstmann, 2012; Kidd et al., 2017). However,

[1] `https://www.cost.eu/actions/CA20136/`, last access October 13, 2023
[2] `https://opensenseaction.eu/`, last access October 13, 2023
[3] `https://www.wasser.sachsen.de/Projektinformationen.html`, last access October 13, 2023

hardware characteristics and hence the quality of CML-based rainfall estimation are subject to change. For instance, CMLs that operate at E-band frequencies may become more prevalent and for these, the rain rate retrieval involves more uncertainty due to nonlinearity of the retrieval function and its increased dependence on the drop size distribution. On the other hand, E-band CMLs provide opportunities for measuring light rainfall or water vapor (Fencl et al., 2020).

Given the availability of suitable CML data, this thesis showed how it can advantageously be used in reconstructions via RM. The promising results should promote endeavors to further improve the method's applicability. For instance, current research is directed towards deriving the spatial dependence structure of rainfall from CMLs by considering Block Kriging concepts, which would be a step towards using RM with CMLs only and thus in regions where rain gauges are sparse or do not exist. Another general improvement would be the consideration of the temporal correlation of rainfall in the field generation process. Finally, with regard to the method's computational complexity, it could be further adapted to its use with large amounts of rainfall data; e.g., by adjusting internal parameters that govern the stochastic field generation process to the considered problem size, or, considering the intermittency of rainfall, by disregarding in the computations those areas that are certainly dry.

Considering the enormous importance of accurate spatial rainfall estimation, it should be aimed for continual improvement of the methods to make use of the available data as effectively as possible. The results presented in this thesis are a step in this direction. Both extending the application of CML rainfall retrieval across borders and applying a sophisticated method for high-quality reconstructions have provided valuable insights upon which future research may build.

Appendices

Appendix A

Definition of Standard Functions

The following is a list of several functions that were used but not explicitly stated in the main part:

- the arithmetic mean

$$\mu(X) = \frac{1}{C} \sum_{i=1}^{C} X_i; \tag{A.1}$$

- the covariance

$$cov(X,Y) = \frac{1}{C} \sum_{i=1}^{C} (X_i - \mu(X))(Y_i - \mu(Y)); \tag{A.2}$$

- the standard deviation

$$\sigma(X,Y) = \sqrt{\frac{1}{C} \sum_{i=1}^{C} (X_i - \mu(X))^2}; \tag{A.3}$$

- the variance

$$var(X,Y) = \sigma^2(X,Y); \tag{A.4}$$

- the two-dimensional Euclidean distance

$$dist(\boldsymbol{x}, \boldsymbol{y}) = \sqrt{(\boldsymbol{x_1} - \boldsymbol{y_1})^2 + \boldsymbol{x_2} - \boldsymbol{y_2})^2}; \tag{A.5}$$

- the continuous ranked probability score

$$crps(P(X), P(Y)) = \int_{-\infty}^{\infty} (P(X) - P(Y))^2 dx. \tag{A.6}$$

In the definitions above, X and Y are sets of values and C their size in the dimension of interest, e.g., for $\mu_{time}(X)$, C equals the number of time steps. The vectors $\boldsymbol{x}$ and $\boldsymbol{y}$ define a position on a grid. $P()$ is the empirical cumulative distribution function.

Appendix B

Transboundary Reconstruction

The CML sensor density in the case study on transboundary reconstruction (Chapter 6) is shown in Figure B.1 for the three processing lines. A second rainfall event of June 29, 2021 is shown in Figure B.2. The mean and median of the performance metrics are presented in Table B.1 and Table B.2, respectively.

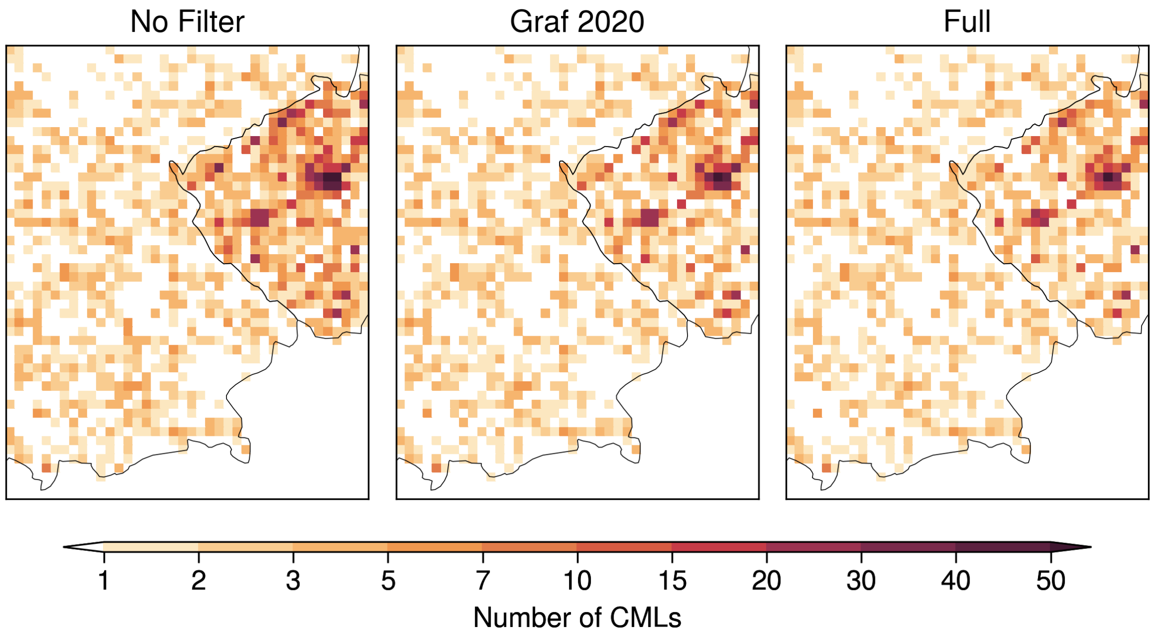

Figure B.1: CML sensor density maps for the three processing lines. The region is divided into squares of 10 km × 10 km and for each of these squares the number of CMLs is shown.

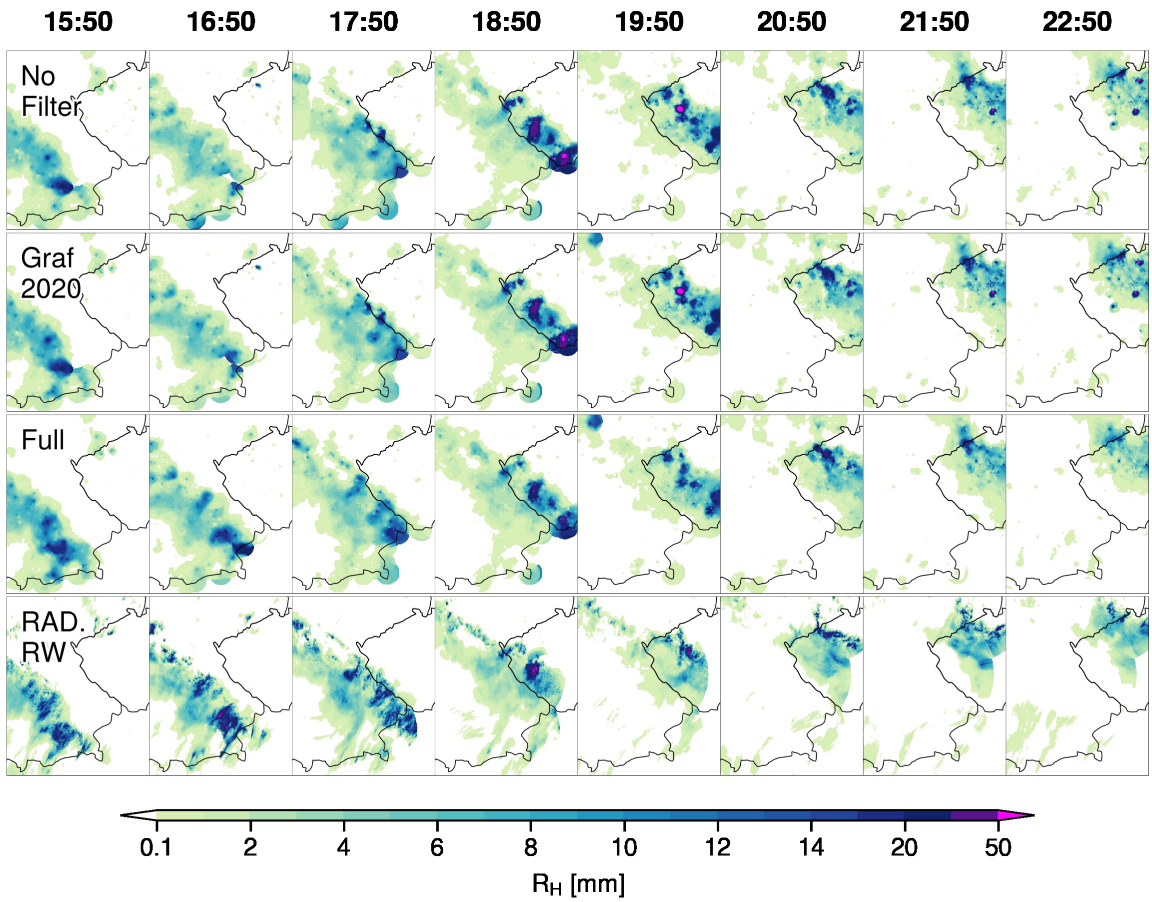

Figure B.2: Transboundary reconstruction of a second rainfall event of June 29, 2021. (cf. Figure 6.6).

Table B.1: Mean performance metrics distinguishing the three processing lines and the two countries. The mean value is calculated over all CMLs and irrespective of the detection limit.

	Country	No Filter	Graf 2020	Full
MAE [mm]	DE	0.080	0.078	0.082
MAE [mm]	CZ	0.190	0.193	0.111
MAE [mm]	Both countries	0.145	0.145	0.098
BIAS [-]	DE	- 0.038	- 0.068	- 0.067
BIAS [-]	CZ	0.799	0.829	0.104
BIAS [-]	Both countries	0.458	0.456	0.024
PCC [-]	DE	0.862	0.884	0.912
PCC [-]	CZ	0.778	0.792	0.836
PCC [-]	Both countries	0.812	0.830	0.871

Table B.2: Median performance metrics distinguishing the three processing lines and the two countries. The median value is calculated over all CMLs and irrespective of the detection limit.

	Country	No Filter	Graf 2020	Full
MAE [mm]	DE	0.069	0.071	0.075
MAE [mm]	CZ	0.099	0.103	0.098
MAE [mm]	Both countries	0.085	0.086	0.087
BIAS [-]	DE	- 0.097	- 0.109	- 0.113
BIAS [-]	CZ	- 0.001	0.031	- 0.066
BIAS [-]	Both countries	- 0.068	- 0.068	- 0.093
PCC [-]	DE	0.892	0.905	0.929
PCC [-]	CZ	0.832	0.840	0.861
PCC [-]	Both countries	0.860	0.869	0.896

Appendix C

Countrywide Reconstruction

Table C.1 summarizes performance metrics that are partly presented and discussed in Chapter 7. For the three selected case studies discussed in Chapter 7, the respective Random Mixing ensemble averages of various sizes are shown in Figures C.1–C.3. Standard performance metrics considering individual RM ensemble members are presented in Figure C.4. Figures C.5 and C.6 visualize the effect of the filtering approach for false-positive CMLs, which is described in Section 7.1. Related to the analysis of computational complexity, Figure C.7 displays the spatial extents of the considered subregions and Figure C.8 shows the working memory requirements over time for calculating the reconstruction of one time step.

Table C.1: Performance metrics for selected time steps and median over the whole period. Metrics are shown for the Random Mixing ensemble (eRM), ensemble mean fields (mRM), and Kriging (KRI). eSAL (eRM) and SAL (KRI) for the selected time steps are discussed in Section 7.2.1. SAL (mRM) for the three time steps is shown in Figures C.1 to C.3. Median over time SAL values are discussed in Section 7.2.2. Standard performance indices are shown for all selected time steps for completeness, but only the median over time is discussed in Section 7.2.3. Note that for the standard performance metrics related to eRM the median over the ensemble dimension is considered before calculating the median over time.

	Jun 11, 01:50	Jul 28, 13:50	Aug 18, 12:50	Median over time
S (eRM)	0.100	-0.257	0.158	-0.110
S (mRM(20))	0.298	0.799	0.530	0.530
S (KRI)	0.355	1.331	0.376	0.583
A (eRM)	-0.072	-0.152	0.142	-0.159
A (mRM(20))	-0.072	-0.152	0.142	-0.159
A (KRI)	-0.096	0.058	0.220	-0.035
L (eRM)	0.016	0.067	0.059	0.042
L (mRM(20))	0.026	0.070	0.070	0.057
L (KRI)	0.021	0.028	0.036	0.059
L_1 (eRM)	0.009	0.029	0.027	0.021
L_1 (mRM(20))	0.009	0.029	0.027	0.021
L_1 (KRI)	0.009	0.014	0.018	0.023
PCC (eRM)	0.905	0.432	0.826	0.651
PCC (mRM)	0.933	0.560	0.912	0.766
PCC (KRI)	0.924	0.649	0.917	0.762
RMSE (eRM)	0.494	2.333	0.207	0.274
RMSE (mRM)	0.363	1.576	0.089	0.164
RMSE (KRI)	0.419	1.277	0.085	0.159
BIAS (eRM)	-0.069	-0.151	0.150	-0.151
BIAS (mRM)	-0.069	-0.141	0.153	-0.147
BIAS (KRI)	-0.091	0.060	0.247	-0.034

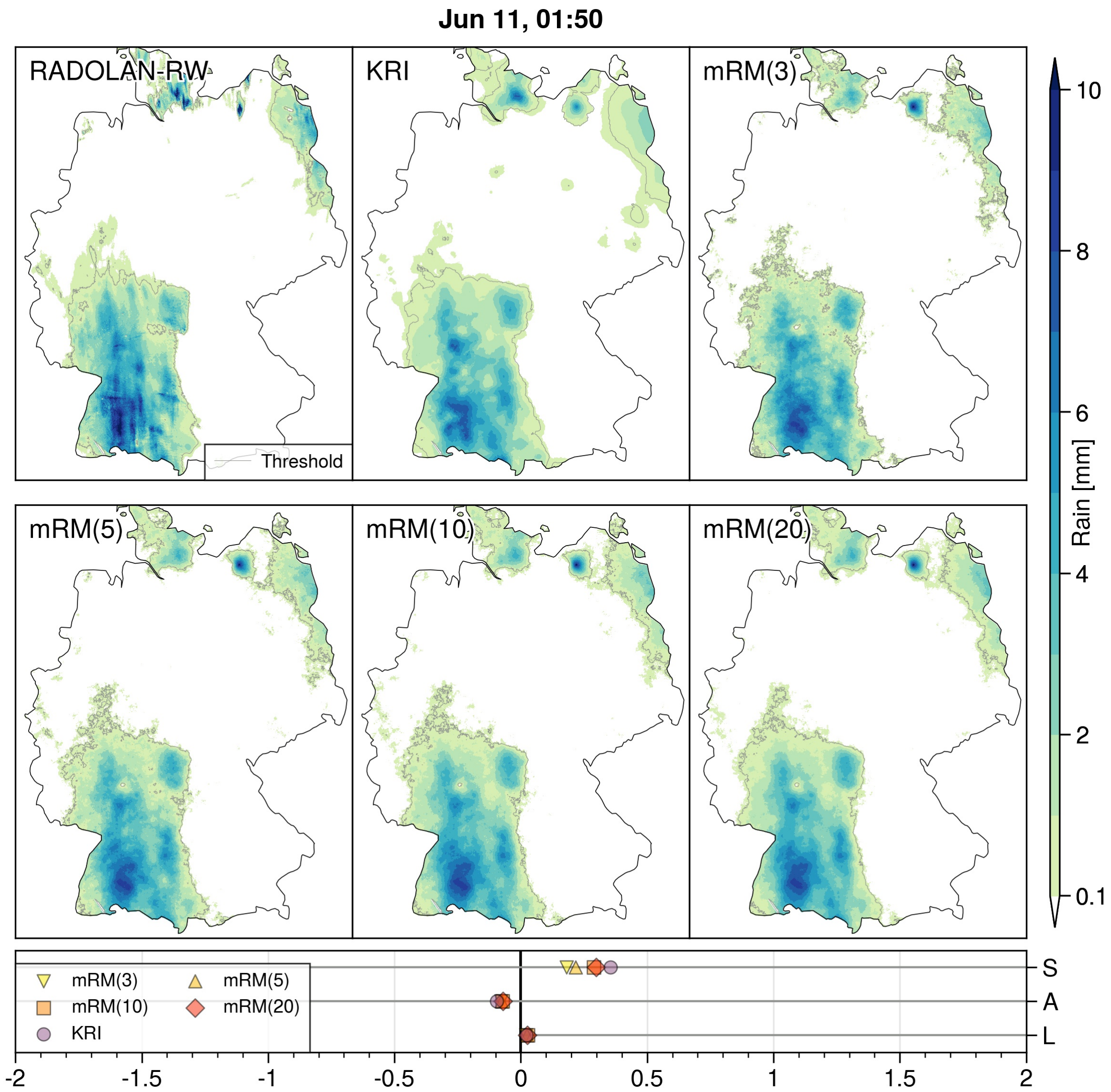

Figure C.1: Rainfall maps of the first selected time step (Jun 11, 01:50) for the reference, KRI reconstruction, and mRM reconstructions with the number of randomly chosen ensemble members considered in brackets (cf. Figure 7.4). Below the maps, the SAL error metrics are shown.

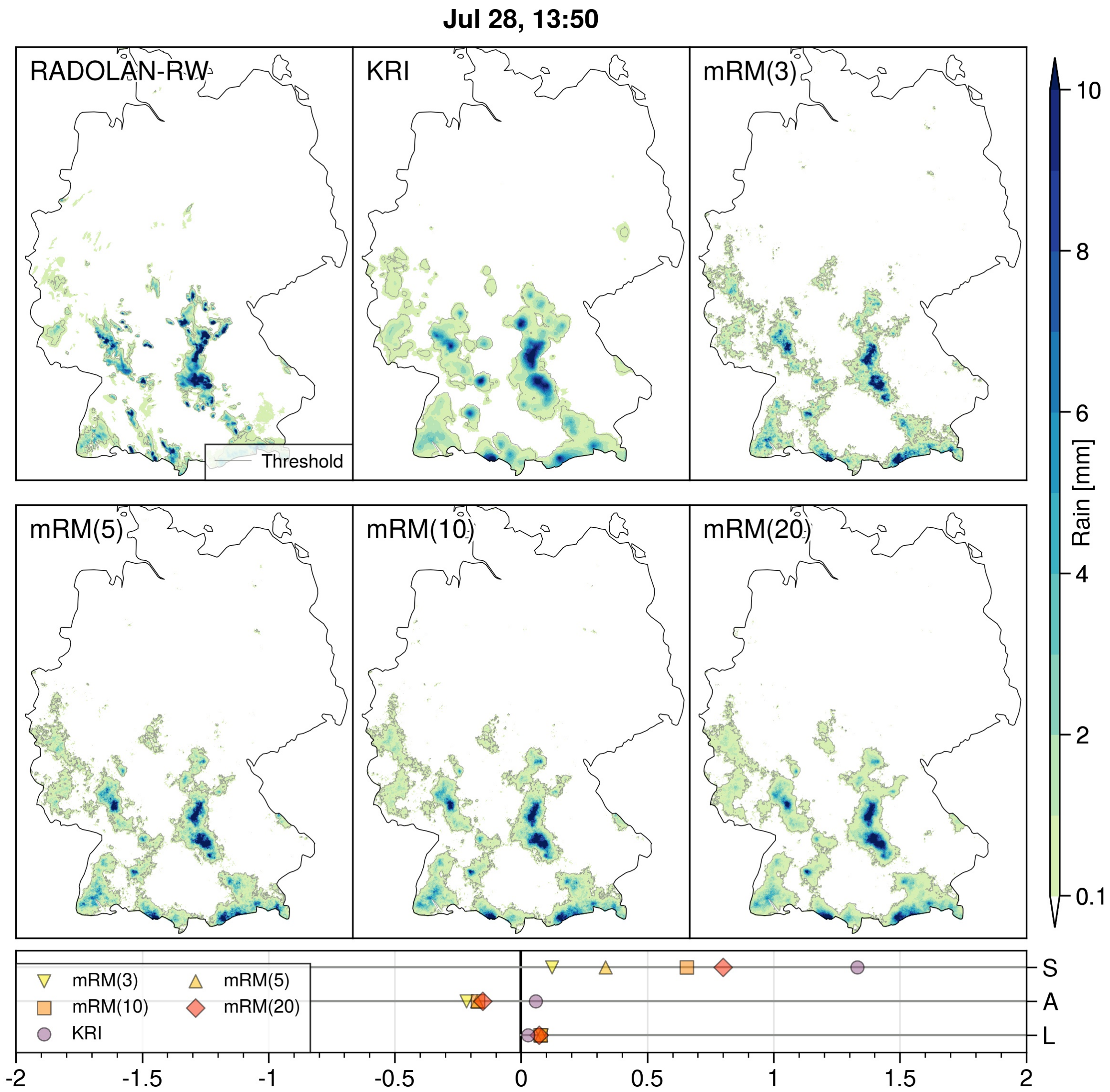

Figure C.2: Rainfall maps of the second selected time step (Jul 28, 13:50) for the reference, KRI reconstruction, and mRM reconstructions with the number of randomly chosen ensemble members considered in brackets (cf. Figure 7.5). Below the maps, the SAL error metrics are shown.

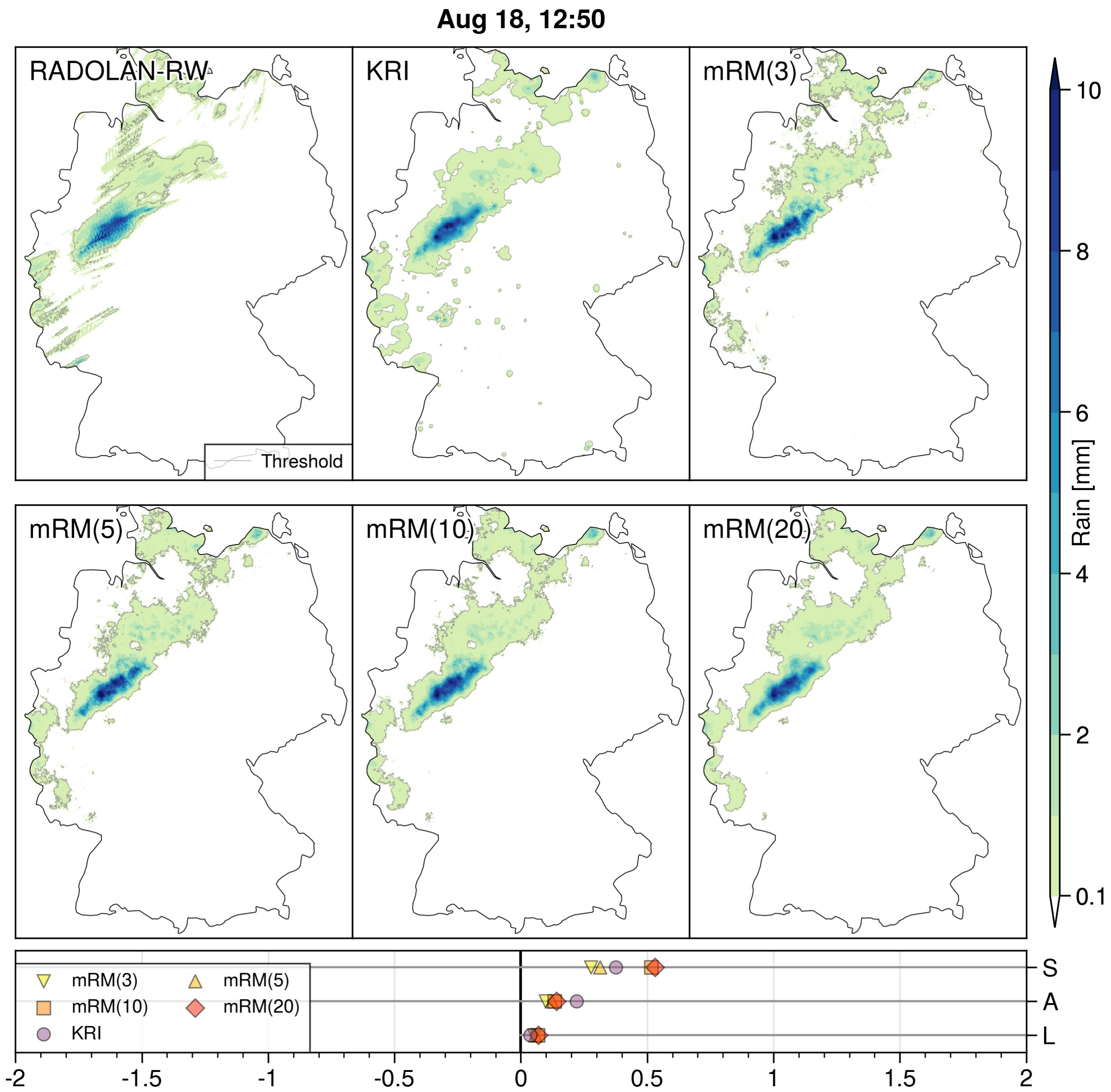

Figure C.3: Rainfall maps of the third selected time step (Aug 18, 12:50) for the reference, KRI reconstruction, and mRM reconstructions with the number of randomly chosen ensemble members considered in brackets (cf. Figure 7.6). Below the maps, the SAL error metrics are shown.

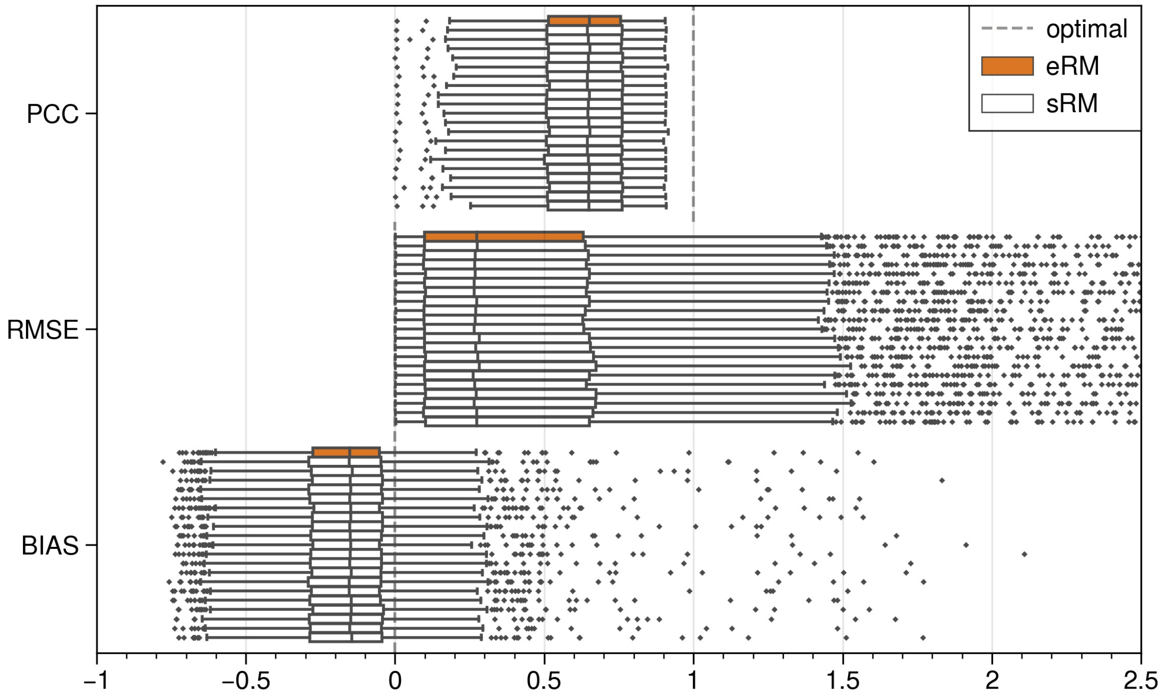

Figure C.4: Standard performance metrics of the individual ensemble members.

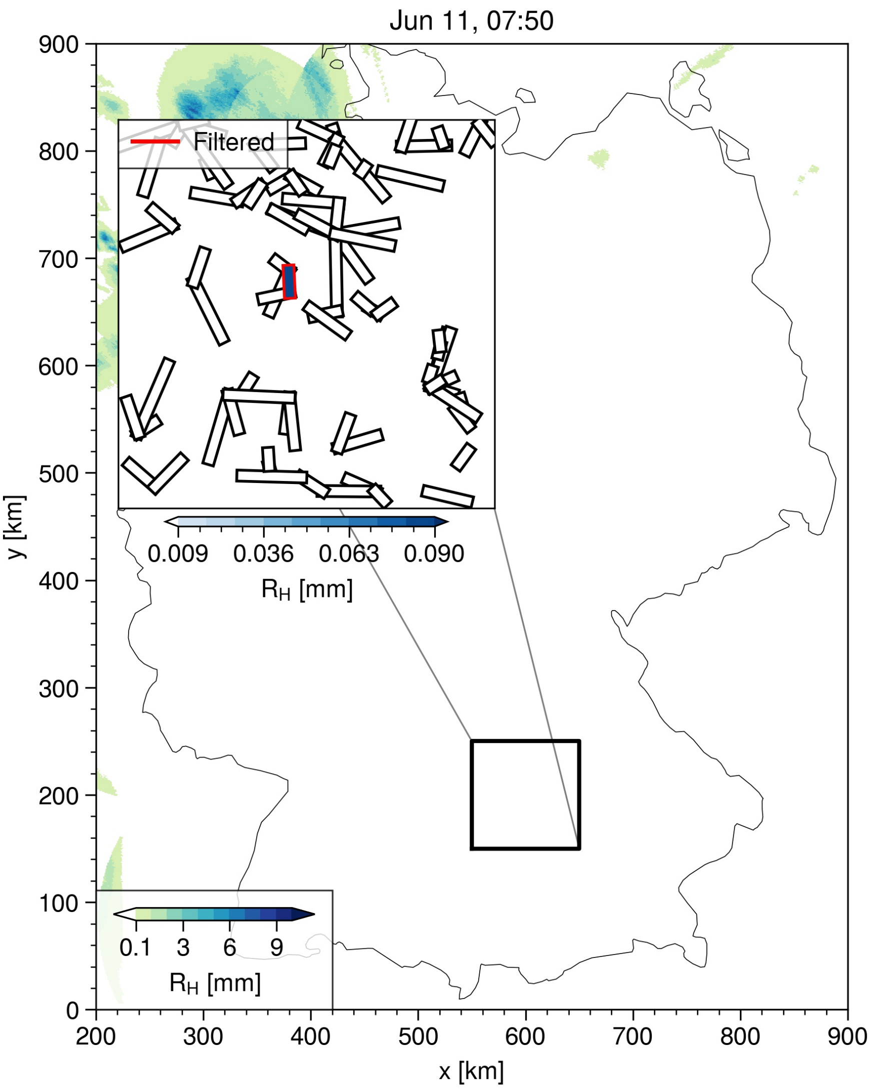

Figure C.5: First example of filtering false-positive CMLs. Note the separate color scale for the inset.

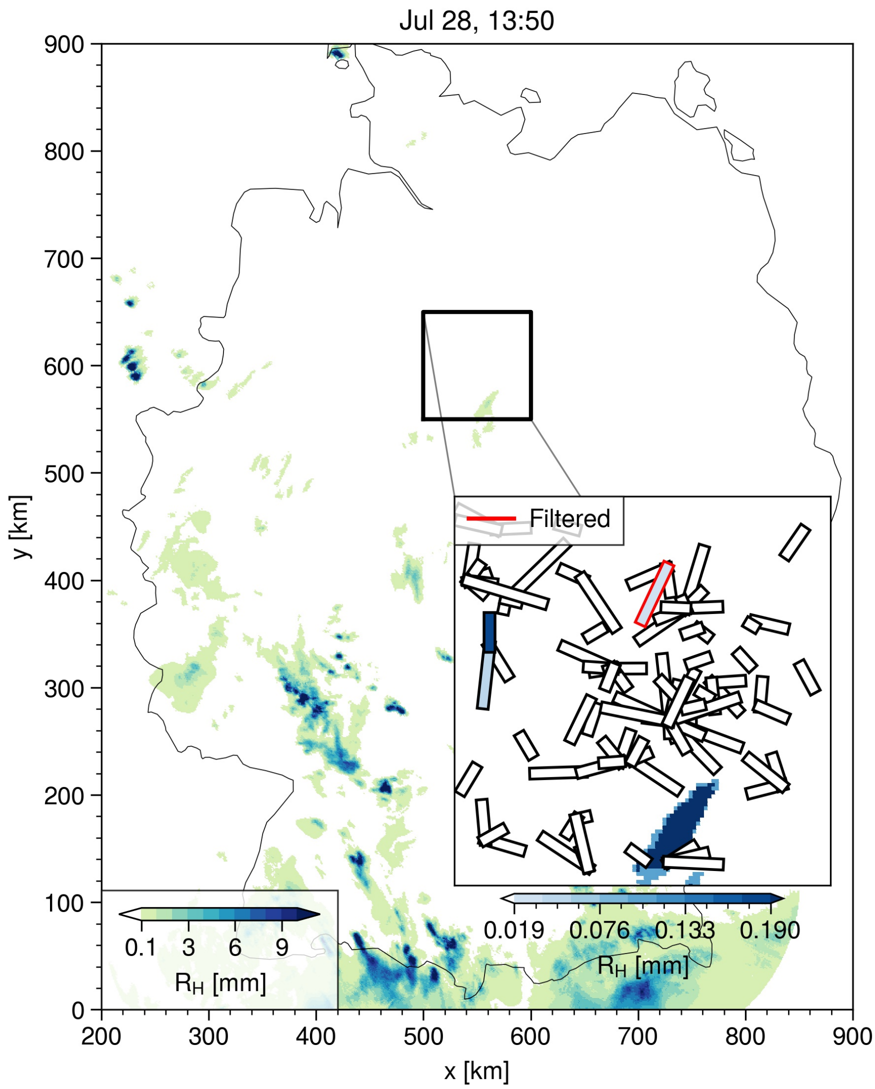

Figure C.6: Second example of filtering false-positive CMLs. Note the separate color scale for the inset.

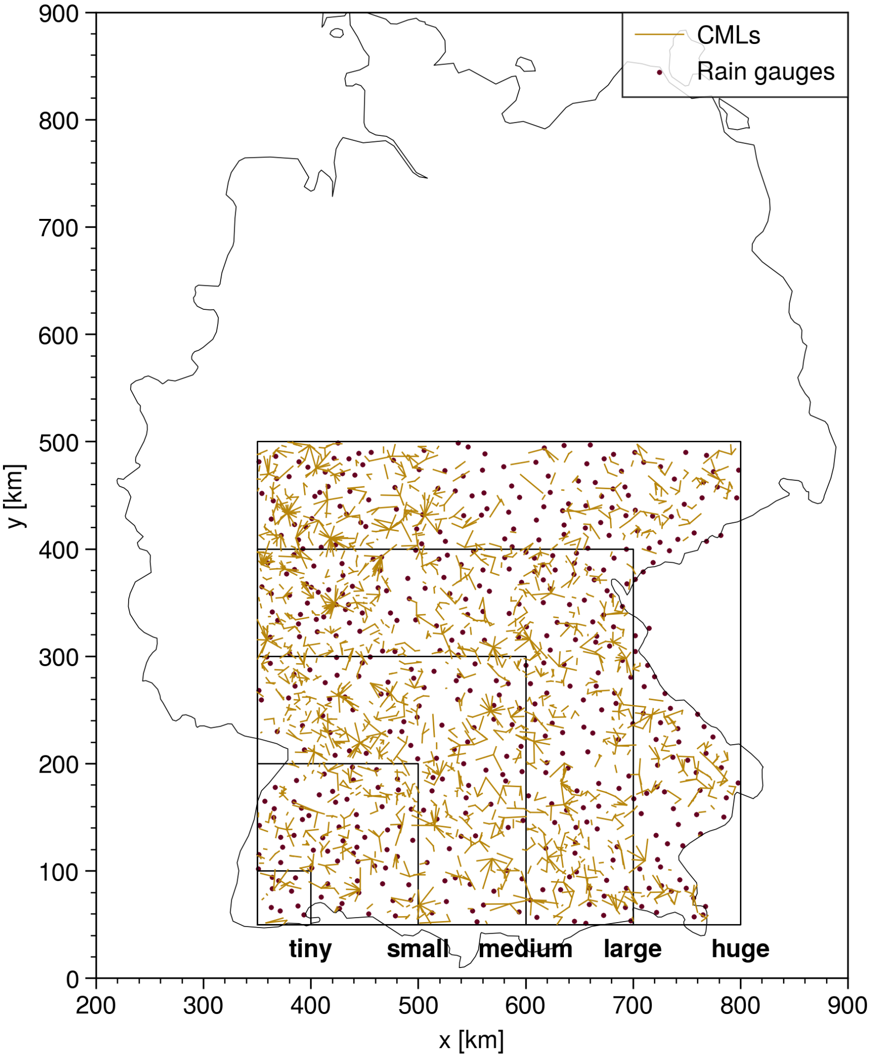

Figure C.7: Spatial extents considered in the computational complexity analysis. The five different regional extents are shown by the black boxes. The coordinates represent the distance from the lower left corner of the RADOLAN-RW projection.

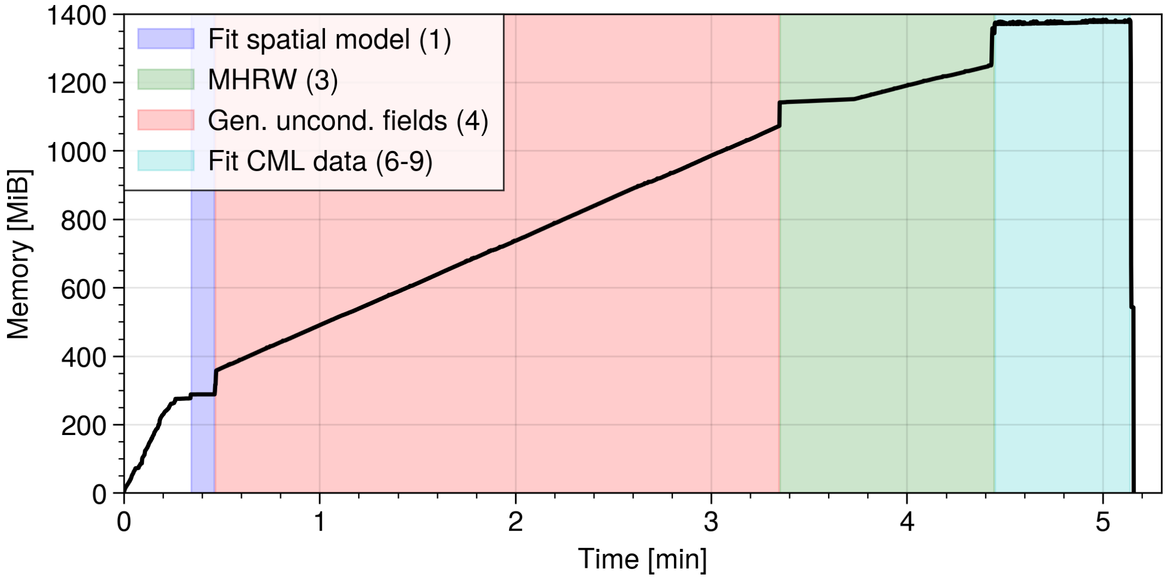

Figure C.8: Evolution of RM working memory requirements over time. The considered event is that of July 28 at 13:50 and the problem size is *medium* (see Table 7.1). The colors represent an approximate separation into the major parts of the algorithm corresponding to the colors of Figure C.7. The numbers behind the subroutines refer to the steps described in Section 4.3.3. Note that the MHRW is conducted after the generation of unconditional fields but described before it in Section 4.3.3 for better comprehensibility; the order of these to subroutines is irrelevant. Also note that the algorithm involves more than the parts presented in this figure; however, the time requirements of the omitted parts are much smaller and can therefore not be displayed.

Bibliography

Abzalov, M. *Applied Mining Geology*, volume 12 of *Modern Approaches in Solid Earth Sciences*. Springer International Publishing, Cham, 2016. doi: 10.1007/978-3-319-39264-6.

Aminou, D. MSG's SEVIRI instrument. *ESA Bulletin(0376-4265)*, 2002. `https://www-cdn.eumetsat.int/files/2020-04/pdf_msg_seviri.pdf`, last access October 13, 2023.

Andersson, J. C. M., Olsson, J., Van De Beek, R. C. Z., and Hansryd, J. OpenMRG: Open data from Microwave links, Radar, and Gauges for rainfall quantification in Gothenburg, Sweden. *Earth System Science Data*, 14(12), 2022. doi: 10.5194/essd-14-5411-2022.

Atlas, D. and Ulbrich, C. W. Path- and area-integrated rainfall measurement by microwave attenuation in the 1–3 cm band. *Journal of Applied Meteorology and Climatology*, 16(12), 1977. doi: 10.1175/1520-0450(1977)016⟨1322:PAAIRM⟩2.0.CO;2.

Bachmaier, M. and Backes, M. Variogram or Semivariogram? Variance or Semivariance? Allan Variance or Introducing a New Term? *Mathematical Geosciences*, 43(6), 2011. doi: 10.1007/s11004-011-9348-3.

Bartels, H., Weigl, E., Reich, D. T., Lang, P., Wagner, A., Kohler, O., and Gerlach, N. Routineverfahren zur Online-Aneichung der Radarniederschlagsdaten mit Hilfe von automatischen Bodenniederschlagsstationen (Ombrometer). 2004. `https://www.dwd.de/DE/leistungen/radolan/radolan_info/\abschlussbericht_pdf.pdf?__blob=publicationFile&v=2`, last access October 13, 2023.

Bauer, P., Thorpe, A., and Brunet, G. The quiet revolution of numerical weather prediction. *Nature*, 525(7567), 2015. doi: 10.1038/nature14956.

Berne, A. and Krajewski, W. Radar for hydrology: Unfulfilled promise or unrecognized potential? *Advances in Water Resources*, 51, 2013. doi: 10.1016/j.advwatres.2012.05.005.

Blettner, N. nblettner/eSALpy: v1.0.0. 2022. doi: 10.5281/zenodo.7049846.

Blettner, N. nblettner/transboundary_cml_rainfall_maps: v0.0.1. 2023. doi: 10.5281/zenodo.7973736.

Blettner, N., Chwala, C., Haese, B., Hörning, S., and Kunstmann, H. Combining Commercial Microwave Link and Rain Gauge Observations to Estimate Countrywide Precipitation: A Stochastic Reconstruction and Pattern Analysis Approach. *Water Resources Research*, 58(10), 2022. doi: 10.1029/2022WR032563.

Blettner, N., Fencl, M., Bareš, V., Kunstmann, H., and Chwala, C. Transboundary Rainfall Estimation Using Commercial Microwave Links. *Earth and Space Science*, 10(8), 2023. doi: 10.1029/2023EA002869.

Bárdossy, A. and Hörning, S. Gaussian and non-Gaussian inverse modeling of groundwater flow using copulas and random mixing. *Water Resources Research*, 52(6), 2016a. doi: 10.1002/2014WR016820.

Bárdossy, A. and Hörning, S. Random Mixing: An Approach to Inverse Modeling for Groundwater Flow and Transport Problems. *Transport in Porous Media*, 114(2), 2016b. doi: 10.1007/s11242-015-0608-4.

Bárdossy, A. and Li, J. Geostatistical interpolation using copulas. *Water Resources Research*, 44(7), 2008. doi: 10.1029/2007WR006115.

Chilès, J. and Delfiner, P. *Geostatistics: Modeling Spatial Uncertainty.* Wiley Series in Probability and Statistics. Wiley, 2009. doi: 10.1002/9781118136188.

Chwala, C. and Kunstmann, H. Commercial microwave link networks for rainfall observation: Assessment of the current status and future challenges. *WIREs Water*, 6(2), 2019. doi: 10.1002/wat2.1337.

Chwala, C., Gmeiner, A., Qiu, W., Hipp, S., Nienaber, D., Siart, U., Eibert, T., Pohl, M., Seltmann, J., Fritz, J., and Kunstmann, H. Precipitation observation using microwave backhaul links in the alpine and pre-alpine region of Southern Germany. *Hydrology and Earth System Sciences*, 16(8), 2012. doi: 10.5194/hess-16-2647-2012.

Chwala, C., Keis, F., and Kunstmann, H. Real-time data acquisition of commercial microwave link networks for hydrometeorological applications. *Atmospheric Measurement Techniques*, 9(3), 2016. doi: 10.5194/amt-9-991-2016.

Chwala, C., Polz, J., Graf, M., Sereb, D., Blettner, N., Keis, F., and Boose, Y. pycomlink/pycomlink: v0.3.2. 2021. doi: 10.5281/zenodo.4810169.

Ciach, G. J. and Krajewski, W. F. Analysis and modeling of spatial correlation structure in small-scale rainfall in Central Oklahoma. *Advances in Water Resources*, 29(10), 2006. doi: 10.1016/j.advwatres.2005.11.003.

Cristiano, E., Ten Veldhuis, M.-C., and Van De Giesen, N. Spatial and temporal variability of rainfall and their effects on hydrological response in urban areas – a review. *Hydrology and Earth System Sciences*, 21(7), 2017. doi: 10.5194/hess-21-3859-2017.

D'Amico, M., Manzoni, A., and Solazzi, G. L. Use of Operational Microwave Link Measurements for the Tomographic Reconstruction of 2-D Maps of Accumulated Rainfall. *IEEE Geoscience and Remote Sensing Letters*, 13(12), 2016. doi: 10.1109/LGRS.2016.2614326.

David, N., Alpert, P., and Messer, H. Technical Note: Novel method for water vapour monitoring using wireless communication networks measurements. *Atmospheric Chemistry and Physics*, 9(7), 2009. doi: 10.5194/acp-9-2413-2009.

David, N., Alpert, P., and Messer, H. The potential of cellular network infrastructures for sudden rainfall monitoring in dry climate regions. *Atmospheric Research*, 131, 2013. doi: 10.1016/j.atmosres.2013.01.004.

de Vos, L. W., Overeem, A., Leijnse, H., and Uijlenhoet, R. Rainfall Estimation Accuracy of a Nationwide Instantaneously Sampling Commercial Microwave Link Network: Error Dependency on Known Characteristics. *Journal of Atmospheric and Oceanic Technology*, 36(7), 2019. doi: 10.1175/JTECH-D-18-0197.1.

Djibo, M., Chwala, C., Graf, M., Polz, J., Kunstmann, H., and Zougmoré, F. High-resolution rainfall maps from commercial microwave links for a data-scarce region in west africa. *Journal of Hydrometeorology*, 24, 2023. doi: https://doi.org/10.1175/JHM-D-23-0015.1.

Doumounia, A., Gosset, M., Cazenave, F., Kacou, M., and Zougmore, F. Rainfall monitoring based on microwave links from cellular telecommunication networks: First results from a West African test bed: Wireless networks for rainfall in africa. *Geophysical Research Letters*, 41(16), 2014. doi: 10.1002/2014GL060724.

Ebert, E. E. Fuzzy verification of high-resolution gridded forecasts: a review and proposed framework. *Meteorological Applications*, 15(1), 2008. doi: 10.1002/met.25.

Eshel, A., Ostrometzky, J., Gat, S., Alpert, P., and Messer, H. Spatial Reconstruction of Rain Fields From Wireless Telecommunication Networks—Scenario-Dependent Analysis of IDW-Based Algorithms. *IEEE Geoscience and Remote Sensing Letters*, 17(5), 2020. doi: 10.1109/LGRS.2019.2935348.

Eshel, A., Messer, H., Kunstmann, H., Alpert, P., and Chwala, C. Quantitative Analysis of the Performance of Spatial Interpolation Methods for Rainfall Estimation Using Commercial Microwave Links. *Journal of Hydrometeorology*, 22(4), 2021. doi: 10.1175/JHM-D-20-0164.1.

Eshel, A., Alpert, P., and Messer, H. Estimating the Parameters of the Spatial Autocorrelation of Rainfall Fields by Measurements From Commercial Microwave Links. *IEEE Transactions on Geoscience and Remote Sensing*, 60, 2022. doi: 10.1109/TGRS.2022.3165309.

Fencl, M. and Vojtěch, B. Quantifying hardware related attenuation from the analysis of nearby microwave links. *2018 IEEE Statistical Signal Processing Workshop (SSP)*, 2018. doi: 10.1109/SSP.2018.8450825.

Fencl, M., Rieckermann, J., Sýkora, P., Stránský, D., and Bareš, V. Commercial microwave links instead of rain gauges: fiction or reality? *Water Science and Technology*, 71(1), 2015. doi: 10.2166/wst.2014.466.

Fencl, M., Dohnal, M., Valtr, P., Grabner, M., and Bareš, V. Atmospheric observations with E-band microwave links – challenges and opportunities. *Atmospheric Measurement Techniques*, 13(12), 2020. doi: 10.5194/amt-13-6559-2020.

Fencl, M., Nebuloni, R., C. M. Andersson, J., Bares, V., Blettner, N., Cazzaniga, G., Chwala, C., Colli, M., De Vos, L., El Hachem, A., Galdies, C., Giannetti, F., Graf, M., Jacoby, D., Victor Habi, H., Musil, P., Ostrometzky, J., Roversi, G., Sapienza, F., Seidel, J., Spackova, A., Van De Beek, R., Walraven, B., Wilgan, K., and Zheng, X. Data formats and standards for opportunistic rainfall sensors [version 1; peer review: 1 approved]. *Open Research Europe*, 3, 2023. doi: 10.12688/openreseurope.16068.1.

Gandin. Objective analysis of meteorological fields. By L. S. Gandin. Translated from the Russian. Jerusalem (Israel Program for Scientific Translations). *Quarterly Journal of the Royal Meteorological Society*, 92(393), 1966. doi: 10.1002/qj.49709239320.

Gilleland, E., Ahijevych, D., Brown, B. G., Casati, B., and Ebert, E. E. Intercomparison of Spatial Forecast Verification Methods. *Weather and Forecasting*, 24(5), 2009. doi: 10.1175/2009WAF2222269.1.

Goldshtein, O., Messer, H., and Zinevich, A. Rain Rate Estimation Using Measurements From Commercial Telecommunications Links. *IEEE Transactions on Signal Processing*, 57(4), 2009. doi: 10.1109/TSP.2009.2012554.

Gosset, M., Kunstmann, H., Zougmore, F., Cazenave, F., Leijnse, H., Uijlenhoet, R., Chwala, C., Keis, F., Doumounia, A., Boubacar, B., Kacou, M., Alpert, P., Messer, H., Rieckermann, J., and Hoedjes, J. Improving Rainfall Measurement in Gauge Poor Regions Thanks to Mobile Telecommunication Networks. *Bulletin of the American Meteorological Society*, 97(3), 2016. doi: 10.1175/BAMS-D-15-00164.1.

Graf, M., Chwala, C., Polz, J., and Kunstmann, H. Rainfall estimation from a German-wide commercial microwave link network: optimized processing and validation for 1 year of data. *Hydrology and Earth System Sciences*, 24(6), 2020. doi: 10.5194/hess-24-2931-2020.

Haase, G. and Johnson, D. OD12: Quality of composites. Technical report, 2018. `https://www.eumetnet.eu/wp-content/uploads/2019/01/\Quality_of_composites_OPERA.pdf`, last access October 13, 2023.

Habi, H. V. and Messer, H. Wet-Dry Classification Using LSTM and Commercial Microwave Links. In *2018 IEEE 10th Sensor Array and Multichannel Signal Processing Workshop (SAM)*, Sheffield, 2018. IEEE. doi: 10.1109/SAM.2018.8448679.

Haese, B., Hörning, S., Chwala, C., Bárdossy, A., Schalge, B., and Kunstmann, H. Stochastic reconstruction and interpolation of precipitation fields using combined information of commercial microwave links and rain gauges: Reconstruction of rainfall fields. *Water Resources Research*, 53(12), 2017. doi: 10.1002/2017WR021015.

Hapuarachchi, H. A. P., Wang, Q. J., and Pagano, T. C. A review of advances in flash flood forecasting. *Hydrological Processes*, 25(18), 2011. doi: 10.1002/hyp.8040.

Hazenberg, P., Leijnse, H., and Uijlenhoet, R. Radar rainfall estimation of stratiform winter precipitation in the Belgian Ardennes. *Water Resources Research*, 47(2), 2011. doi: 10.1029/2010WR009068.

Hogg, D. C. Millimeter-Wave Communication through the Atmosphere: The known and unknown features in propagation of short radio waves are discussed. *Science*, 159(3810), 1968. doi: 10.1126/science.159.3810.39.

Hou, A. Y., Kakar, R. K., Neeck, S., Azarbarzin, A. A., Kummerow, C. D., Kojima, M., Oki, R., Nakamura, K., and Iguchi, T. The Global Precipitation Measurement Mission. *Bulletin of the American Meteorological Society*, 95(5), 2014. doi: 10.1175/BAMS-D-13-00164.1.

Hu, L. Y. Gradual Deformation and Iterative Calibration of Gaussian-Related Stochastic Models. *Mathematical Geology*, 2000. doi: 10.1023/A:1007506918588.

Huffman, G. J., Bolvin, D. T., Braithwaite, D., Hsu, K., Joyce, R., Kidd, C., Nelkin, E. J., Sorooshian, S., Tan, J., and Xie, P. NASA global precipitation measurement (GPM) integrated multi-satellite retrievals for GPM (IMERG). 2020. `https://gpm.nasa.gov/sites/default/files/2020-05/IMERG_ATBD_V06.3.pdf`, last access October 13, 2023.

Huuskonen, A., Saltikoff, E., and Holleman, I. The Operational Weather Radar Network in Europe. *Bulletin of the American Meteorological Society*, 95(6), 2014. doi: 10.1175/BAMS-D-12-00216.1.

Hörning, S. and Blettner, N. nblettner/RMWSPy: v1.1.1. 2022. doi: 10.5281/zenodo.7049826.

Hörning, S. and Haese, B. RMWSPy (v 1.1): A Python code for spatial simulation and inversion for environmental applications. *Environmental Modelling & Software*, 138, 2021. doi: 10.1016/j.envsoft.2021.104970.

Hörning, S., Sreekanth, J., and Bárdossy, A. Computational efficient inverse groundwater modeling using Random Mixing and Whittaker–Shannon interpolation. *Advances in Water Resources*, 123, 2019. doi: 10.1016/j.advwatres.2018.11.012.

IPCC. Summary for policymakers [H.-O. Pörtner, D.C. Roberts, M. Tignor, E.S. Poloczanska, K. Mintenbeck, A. Alegría, M. Craig, S. Langsdorf, S. Löschke, V. Möller, A. Okem, B. Rama (eds.)]. In: Climate Change 2022: Impacts, Adaptation and Vulnerability. Contribution of Working Group II to the Sixth Assessment Report of the Intergovernmental Panel on Climate Change. *Cambridge University Press, Cambridge, UK and New York, NY, USA, pp. 3-33*, 2022. doi: 10.1017/9781009325844.

ITU-R. Specific attenuation model for rain for use in prediction methods (recommendation p.838-3). 2005. `https://www.itu.int/dms_pubrec/itu-r/rec/p/R-REC-P.838-3-200503-I!!PDF-E.pdf`, last access October 13, 2023.

Journel, A. G. and Huijbregts, C. J. *Mining geostatistics.* London; New York: Academic Press, 1978.

Kabanikhin, S. I. *Inverse and ill-posed problems: theory and applications.* Number 55 in Inverse and ill-posed problems series. De Gruyter, Berlin; Boston, 2012. doi: 10.1515/9783110224016.

Kharadly, M. and Ross, R. Effect of wet antenna attenuation on propagation data statistics. *IEEE Transactions on Antennas and Propagation*, 49(8), 2001. doi: 10.1109/8.943313.

Kidd, C., Becker, A., Huffman, G. J., Muller, C. L., Joe, P., Skofronick-Jackson, G., and Kirschbaum, D. B. So, How Much of the Earth's Surface Is Covered by Rain Gauges? *Bulletin of the American Meteorological Society*, 98(1), 2017. doi: 10.1175/BAMS-D-14-00283.1.

Krajewski, W. F., Ciach, G. J., and Habib, E. An analysis of small-scale rainfall variability in different climatic regimes. *Hydrological Sciences Journal*, 48(2), 2003. doi: 10.1623/hysj.48.2.151.44694.

Kumah, K., Maathuis, B., Hoedjes, J., and Su, Z. Near real-time estimation of high spatiotemporal resolution rainfall from cloud top properties of the MSG satellite and commercial microwave link rainfall intensities. *Atmospheric Research*, 279, 2022. doi: 10.1016/j.atmosres.2022.106357.

Lanza, L. G. and Vuerich, E. The WMO Field Intercomparison of Rain Intensity Gauges. *Atmospheric Research*, 94(4), 2009. doi: 10.1016/j.atmosres.2009.06.012.

Laux, P., Dieng, D., Portele, T. C., Wei, J., Shang, S., Zhang, Z., Arnault, J., Lorenz, C., and Kunstmann, H. A High-Resolution Regional Climate Model Physics Ensemble for Northern Sub-Saharan Africa. *Frontiers in Earth Science*, 9, 2021. doi: 10.3389/feart.2021.700249.

Leijnse, H., Uijlenhoet, R., and Stricker, J. N. M. Rainfall measurement using radio links from cellular communication networks. *Water Resources Research*, 43(3), 2007. doi: 10.1029/2006WR005631.

Leijnse, H., Uijlenhoet, R., and Stricker, J. Microwave link rainfall estimation: Effects of link length and frequency, temporal sampling, power resolution, and wet antenna attenuation. *Advances in Water Resources*, 31(11), 2008. doi: 10.1016/j.advwatres.2008.03.004.

Liu, J., Yang, H., Gosling, S. N., Kummu, M., Flörke, M., Pfister, S., Hanasaki, N., Wada, Y., Zhang, X., Zheng, C., Alcamo, J., and Oki, T. Water scarcity assessments in the past, present, and future: Review on water scarcity assessment. *Earth's Future*, 5(6), 2017. doi: 10.1002/2016EF000518.

Lorenz, C. and Kunstmann, H. The Hydrological Cycle in Three State-of-the-Art Reanalyses: Intercomparison and Performance Analysis. *Journal of Hydrometeorology*, 13(5), 2012. doi: 10.1175/JHM-D-11-088.1.

Matheron, G. Les variables régionalisées et leur estimation, une application de la théorie de fonctions aleéatoires aux sciences de la nature. 1965.

McKee, J. L. and Binns, A. D. A review of gauge–radar merging methods for quantitative precipitation estimation in hydrology. *Canadian Water Resources Journal / Revue canadienne des ressources hydriques*, 41(1-2), 2016. doi: 10.1080/07011784.2015.1064786.

Mekonnen, M. M. and Hoekstra, A. Y. Four billion people facing severe water scarcity. *Science Advances*, 2(2), 2016. doi: 10.1126/sciadv.1500323.

Messer, H. Environmental Monitoring by Wireless Communication Networks. *Science*, 312 (5774), 2006. doi: 10.1126/science.1120034.

Mishra, A. K. and Singh, V. P. A review of drought concepts. *Journal of Hydrology*, 391 (1-2), 2010. doi: 10.1016/j.jhydrol.2010.07.012.

Moroder, C., Siart, U., Chwala, C., and Kunstmann, H. Microwave Instrument for Simultaneous Wet Antenna Attenuation and Precipitation Measurement. *IEEE Transactions on Instrumentation and Measurement*, 69(8), 2020. doi: 10.1109/TIM.2019.2961498.

Nebuloni, R., Cazzaniga, G., D'Amico, M., Deidda, C., and De Michele, C. Comparison of CML Rainfall Data against Rain Gauges and Disdrometers in a Mountainous Environment. *Sensors*, 22(9), 2022. doi: 10.3390/s22093218.

Nelsen, R. B. *An Introduction to Copulas.* Springer New York, NY, 2 edition, 2006. doi: 10.1007/0-387-28678-0.

Ochoa-Rodriguez, S., Wang, L., Willems, P., and Onof, C. A Review of Radar-Rain Gauge Data Merging Methods and Their Potential for Urban Hydrological Applications. *Water Resources Research*, 55(8), 2019. doi: 10.1029/2018WR023332.

Olsen, R., Rogers, D., and Hodge, D. The aR^brelation in the calculation of rain attenuation. *IEEE Transactions on Antennas and Propagation*, 26(2), 1978. doi: 10.1109/TAP.1978.1141845.

Overeem, A., Leijnse, H., and Uijlenhoet, R. Measuring urban rainfall using microwave links from commercial cellular communication networks: Measuring urban rainfall using microwave links. *Water Resources Research*, 47(12), 2011. doi: 10.1029/2010WR010350.

Overeem, A., Leijnse, H., and Uijlenhoet, R. Country-wide rainfall maps from cellular communication networks. *Proceedings of the National Academy of Sciences*, 110(8), 2013. doi: 10.1073/pnas.1217961110.

Overeem, A., Leijnse, H., and Uijlenhoet, R. Retrieval algorithm for rainfall mapping from microwave links in a cellular communication network. *Atmospheric Measurement Techniques*, 9(5), 2016a. doi: 10.5194/amt-9-2425-2016.

Overeem, A., Leijnse, H., and Uijlenhoet, R. Two and a half years of country-wide rainfall maps using radio links from commercial cellular telecommunication networks. *Water Resources Research*, 52(10), 2016b. doi: 10.1002/2016WR019412.

Overeem, A., Leijnse, H., van Leth, T. C., Bogerd, L., Priebe, J., Tricarico, D., Droste, A., and Uijlenhoet, R. Tropical rainfall monitoring with commercial microwave links in Sri Lanka. *Environmental Research Letters*, 16(7), 2021. doi: 10.1088/1748-9326/ac0fa6.

Pastorek, J., Fencl, M., Rieckermann, J., and Bares, V. Precipitation Estimates From Commercial Microwave Links: Practical Approaches to Wet-Antenna Correction. *IEEE Transactions on Geoscience and Remote Sensing*, 2021. doi: 10.1109/TGRS.2021.3110004.

Pollock, M. D., O'Donnell, G., Quinn, P., Dutton, M., Black, A., Wilkinson, M. E., Colli, M., Stagnaro, M., Lanza, L. G., Lewis, E., Kilsby, C. G., and O'Connell, P. E. Quantifying and Mitigating Wind-Induced Undercatch in Rainfall Measurements. *Water Resources Research*, 54(6), 2018. doi: 10.1029/2017WR022421.

Polz, J., Chwala, C., Graf, M., and Kunstmann, H. Rain event detection in commercial microwave link attenuation data using convolutional neural networks. *Atmospheric Measurement Techniques*, 13(7), 2020. doi: 10.5194/amt-13-3835-2020.

Polz, J., Graf, M., and Chwala, C. Missing rainfall extremes in commercial microwave link data due to total loss of signal. *Earth and Space Science*, 2023. doi: 10.1029/2022EA002456.

Por, V. N. and Sevruk, B. Estimation of Wind-Induced Error of Rainfall Gauge Measurements Using a Numerical Simulation. *Journal of Atmospheric and Oceanic Technology*, 16, 1999. doi: 10.1175/1520-0426(1999)016⟨0450:EOWIEO⟩2.0.CO;2.

Portele, T. C., Laux, P., Lorenz, C., Janner, A., Horna, N., Fersch, B., Iza, M., and Kunstmann, H. Ensemble-Tailored Pattern Analysis of High-Resolution Dynamically Downscaled Precipitation Fields: Example for Climate Sensitive Regions of South America. *Frontiers in Earth Science*, 9, 2021. doi: 10.3389/feart.2021.669427.

Radanovics, S., Vidal, J.-P., and Sauquet, E. Spatial Verification of Ensemble Precipitation: An Ensemble Version of SAL. *Weather and Forecasting*, 33(4), 2018. doi: 10.1175/WAF-D-17-0162.1.

Rios Gaona, M. F., Overeem, A., Raupach, T. H., Leijnse, H., and Uijlenhoet, R. Rainfall retrieval with commercial microwave links in São Paulo, Brazil. *Atmospheric Measurement Techniques*, 11(7), 2018. doi: 10.5194/amt-11-4465-2018.

Rousi, E., Fink, A. H., Andersen, L. S., Becker, F. N., Beobide-Arsuaga, G., Breil, M., Cozzi, G., Heinke, J., Jach, L., Niermann, D., Petrovic, D., Richling, A., Riebold, J., Steidl, S., Suarez-Gutierrez, L., Tradowsky, J. S., Coumou, D., Düsterhus, A., Ellsäßer, F., Fragkoulidis, G., Gliksman, D., Handorf, D., Haustein, K., Kornhuber, K., Kunstmann, H., Pinto, J. G., Warrach-Sagi, K., and Xoplaki, E. The extremely hot and dry 2018 summer in central and northern Europe from a multi-faceted weather and climate perspective. *Natural Hazards and Earth System Sciences*, 23(5), 2023. doi: 10.5194/nhess-23-1699-2023.

Roversi, G., Alberoni, P. P., Fornasiero, A., and Porcù, F. Commercial microwave links as a tool for operational rainfall monitoring in Northern Italy. *Atmospheric Measurement Techniques*, 13(11), 2020. doi: 10.5194/amt-13-5779-2020.

Scheidegger, A. and Rieckermann, J. Bayesian assimilation of rainfall sensors with fundamentally different integration characteristics. In WRaH Proceedings. Washington, DC: International Weather Radar and Hydrology symposium. Technical report, 2014.

Schleiss, M. and Berne, A. Identification of Dry and Rainy Periods Using Telecommunication Microwave Links. *IEEE Geoscience and Remote Sensing Letters*, 7(3), 2010. doi: 10.1109/LGRS.2010.2043052.

Schleiss, M., Jaffrain, J., and Berne, A. Statistical analysis of rainfall intermittency at small spatial and temporal scales: Rainfall intermittency. *Geophysical Research Letters*, 38(18), 2011. doi: 10.1029/2011GL049000.

Schleiss, M., Rieckermann, J., and Berne, A. Quantification and Modeling of Wet-Antenna Attenuation for Commercial Microwave Links. *IEEE Geoscience and Remote Sensing Letters*, 10(5), 2013. doi: 10.1109/LGRS.2012.2236074.

Skofronick-Jackson, G., Petersen, W. A., Berg, W., Kidd, C., Stocker, E. F., Kirschbaum, D. B., Kakar, R., Braun, S. A., Huffman, G. J., Iguchi, T., Kirstetter, P. E., Kummerow, C., Meneghini, R., Oki, R., Olson, W. S., Takayabu, Y. N., Furukawa, K., and Wilheit, T. The Global Precipitation Measurement (GPM) Mission for Science and Society. *Bulletin of the American Meteorological Society*, 98(8), 2017. doi: 10.1175/BAMS-D-15-00306.1.

Smiatek, G., Keis, F., Chwala, C., Fersch, B., and Kunstmann, H. Potential of commercial microwave link network derived rainfall for river runoff simulations. *Environmental Research Letters*, 12(3), 2017. doi: 10.1088/1748-9326/aa5f46.

Strangeways, I. A history of rain gauges. *Weather*, 65(5), 2010. doi: 10.1002/wea.548.

Tarantola, A. *Inverse Problem Theory and Methods for Model Parameter Estimation.* Society for Industrial and Applied Mathematics, 2005. doi: 10.1137/1.9780898717921.

Tiede, J., Chwala, C., and Siart, U. New Insights Into the Dynamics of Wet Antenna Attenuation Based on In Situ Estimations Provided by the Dedicated Field Experiment ATTRRA2. *IEEE Geoscience and Remote Sensing Letters*, 20, 2023. doi: 10.1109/LGRS.2023.3320755.

Tradowsky, J. S., Philip, S. Y., Kreienkamp, F., Kew, S. F., Lorenz, P., Arrighi, J., Bettmann, T., Caluwaerts, S., Chan, S. C., De Cruz, L., De Vries, H., Demuth, N., Ferrone, A., Fischer, E. M., Fowler, H. J., Goergen, K., Heinrich, D., Henrichs, Y., Kaspar, F., Lenderink, G., Nilson, E., Otto, F. E. L., Ragone, F., Seneviratne, S. I., Singh, R. K., Skålevåg, A., Termonia, P., Thalheimer, L., Van Aalst, M., Van Den Bergh, J., Van De Vyver, H., Vannitsem, S., Van Oldenborgh, G. J., Van Schaeybroeck, B., Vautard, R., Vonk, D., and Wanders, N. Attribution of the heavy rainfall events leading to severe flooding in Western Europe during July 2021. *Climatic Change*, 176(7), 2023. doi: 10.1007/s10584-023-03502-7.

Uijlenhoet, R., Overeem, A., and Leijnse, H. Opportunistic remote sensing of rainfall using microwave links from cellular communication networks. *WIREs Water*, 5(4), 2018. doi: 10.1002/wat2.1289.

Ulbrich, C. W. and Lee, L. G. Rainfall Measurement Error by WSR-88D Radars due to Variations in Z–R Law Parameters and the Radar Constant. *Journal of Atmospheric and*

Oceanic Technology, 16(8), 1999. doi: 10.1175/1520-0426(1999)016⟨1017:RMEBWR⟩2.0.CO;2.

UNHCR. As the Horn of Africa drought enters a sixth failed rainy season, UNHCR calls for urgent assistance, 2023. https://www.unhcr.org/news/horn-africa-drought-enters-sixth-failed-rainy-season-unhcr-calls-urgent-assistance, last access October 13, 2023. Technical report, 2023.

Upton, G., Holt, A., Cummings, R., Rahimi, A., and Goddard, J. Microwave links: The future for urban rainfall measurement? *Atmospheric Research*, 77(1-4), 2005. doi: 10.1016/j.atmosres.2004.10.009.

Valtr, P., Fencl, M., and Bareš, V. Excess attenuation caused by antenna wetting of terrestrial microwave links at 32 ghz. *IEEE Antennas and Wireless Propagation Letters*, 18(8), 2019. doi: 10.1109/LAWP.2019.2925455.

Van Leth, T. C., Overeem, A., Leijnse, H., and Uijlenhoet, R. A measurement campaign to assess sources of error in microwave link rainfall estimation. *Atmospheric Measurement Techniques*, 11(8), 2018. doi: 10.5194/amt-11-4645-2018.

Vivekanandan, J., Martner, B., Politovich, M., and Guifu Zhang. Retrieval of atmospheric liquid and ice characteristics using dual-wavelength radar observations. *IEEE Transactions on Geoscience and Remote Sensing*, 37(5), 1999. doi: 10.1109/36.789629.

Vörösmarty, C. J., McIntyre, P. B., Gessner, M. O., Dudgeon, D., Prusevich, A., Green, P., Glidden, S., Bunn, S. E., Sullivan, C. A., Liermann, C. R., and Davies, P. M. Global threats to human water security and river biodiversity. *Nature*, 467(7315), 2010. doi: 10.1038/nature09440.

Wang, Z., Schleiss, M., Jaffrain, J., Berne, A., and Rieckermann, J. Using Markov switching models to infer dry and rainy periods from telecommunication microwave link signals. *Atmospheric Measurement Techniques*, 5(7), 2012. doi: 10.5194/amt-5-1847-2012.

Werner, P. C. and Gerstengarbe, F.-W. Katalog der Großwetterlagen Europas (1881-2009), 2010. `https://publications.pik-potsdam.de/pubman/item/item_16367_1/component/file_16368/4609.pdf`, last access October 13, 2023.

Wernli, H., Paulat, M., Hagen, M., and Frei, C. SAL—A Novel Quality Measure for the Verification of Quantitative Precipitation Forecasts. *Monthly Weather Review*, 136(11), 2008. doi: 10.1175/2008MWR2415.1.

World Economic Forum. The global risks report. Technical report, 2023. `https://www3.weforum.org/docs/WEF_Global_Risks_Report_2023.pdf`, last access October 13, 2023.

Zhou, H., Gómez-Hernández, J. J., and Li, L. Inverse methods in hydrogeology: Evolution and recent trends. *Advances in Water Resources*, 63, 2014. doi: 10.1016/j.advwatres.2013.10.014.

Zinevich, A., Alpert, P., and Messer, H. Estimation of rainfall fields using commercial microwave communication networks of variable density. *Advances in Water Resources*, 31 (11), 2008. doi: 10.1016/j.advwatres.2008.03.003.